# Ultrathin Metasurface Devices for Phase and Polarization Control

Chunmei Zhang

Submitted for the degree of Doctor of Philosophy

Institute of Photonics and Quantum Sciences

School of Engineering & Physical Sciences

Heriot-Watt University

March 2019

# Abstract

Metamaterials are artificial materials, which consist of periodic or non-periodic structures of manmade “atoms” with a typical size of subwavelength scale. Benefiting from the freedom to tailor the properties of electromagnetic waves that are unavailable in nature, metamaterials have brought new concepts and new discoveries to the world (e.g., negative refraction, super imaging and cloaking). However, the application of 3D metamaerials in the optical range is limited by current nanofabrication techniques. As 2D counterparts of metamaterials, metasurfaces, which are comprised of a single layer or a stack of several layers of 2D structures, can facilitate manufacturing process and manipulate light propagation in desirable manner. Metsurfaces are ultrathin and ultraflat, which has enabled ultrathin optical devices that can outperform the capabilities of traditional bulky optical elements. The unprecedented capabilities of metasurfaces in the manipulation of amplitude, phase and polarization have led to the development of novel, compact optical devices with specially designed functionalities.

In this thesis, we simultaneously control the phase and polarization state of light with one single metasurface, enabling novel multifunctional devices that are not possible with conventional optical devices. To meet the growing requirement of device miniaturization and system integration, it is of great importance and interest to develop ultrathin optical devices that integrate multiple functionalities into one device while preserving their independent functionalities. To increase the functionality density, we develop metasurface devices that can dynamically control the superposition of laser beams with various orbital angular momentum (OAM). This unique approach can arbitrarily realize different functionalities in multiple channels based on a single plasmonic metasurface. As a proof of concept, we experimentally demonstrate an ultrathin optical device that can simultaneously realize polarization-controllable hologram and superposition of OAM beams in multiple channels, which is realized by controlling the polarization state of the incident light.

Although human eyes or cameras are sensitive to spatially varying intensity or colour profiles, they are blind to polarization profiles with uniform intensity profiles. We propose and experimentally demonstrate an approach to hide a high-resolution grayscale image in a laser beam. The space-variant polarization profile originates from the superposition of two circularly polarized beams with opposite handedness that come from from a single metasurface device. Upon the illumination of a linearly polarized light beam, we experimentally demonstrate a metasurface device that can generate a light beam with

inhomogeneous polarization profile for hiding a quick response (QR) code. The unique measurement technique used here holds great promise for anti-counterfeiting and encryption. This approach is extended to hide a color image through the local control of both polarization and color selectivity based on a high-efficiency transmissive dielectric metasurface, which consists of silicon nanoblocks that can precisely control brightness and contrast. This approach provides an extraordinary capability in additive color mixing and tailoring the polarization of light at the nanoscale.

The unprecedented capabilities of optical metasurfaces in the local manipulation of the phase and polarization of light at the subwavelength scale, open a new window for the implementation of a plethora of novel optical components. The unique advantages of simplicity and robustness of our design, ease of fabrication, compactness and unusual functionalities of ultrathin metadevices render optical metasurfaces very attractive for new applications in free-space imaging, information processing, encryption, anti-counterfeiting, optical communications, and fundamental physics. The plan for the future work in this amazing field is also discussed in the last chapter.

## Dedication

*To my beloved family*

# Acknowledgement

First of all, my gratitude goes to my supervisor Dr. Wei Wang, for his instructive advices, suggestions, encouragements and support. My second supervisor Dr. Jining Sun gave me some advices as well. This thesis would be impossible without the support of Dr. Xianzhong Chen, whose enthusiasm for metasurfaces and metamaterials triggers my love for this beautiful and dynamic research field.

I am deeply indebted to all the other members in the Experimental Nanophotonics Group at Heriot-Watt University, for their direct and indirect help. Mr. Yuttana Intaravanne, Dr. Fuyong Yue, Dr. Dandan Wen, Prof. Xiaofei Zang, Prof. Huigang Liu, Prof. Zhengren Zhang, Prof. Ming Chen all helped me along this learning journey. Those discussions, time spent together in the group meetings and laboratory will be deeply imprinted in my brain.

I also would like to take this chance to thank all the following collaborators for their great contributions: Mr. Neil Ross for the support with fabrication in the clean room, Prof. Yan Zhang & Ms. Huan Zhao from Capital Normal University for the great support during my visit in 2018, Prof. Guoxing Zheng at Wuhan University, Prof. Fengliang Dong and his team at National Centre for Nanoscale Science and Technology of China. I received countless help from Mubbashar, Ambrose, Gordon, Ali, Arshad, Alwin, Guochao, Farooq, Tariq and other members of Room 2.26 in James Nasmyth building in the last three and half years. Those happy time in the office shall be remembered by me. Special thanks to Mrs Loraine Cameron, Louise Exton and all other staff in EPS PGR office, whose professional services set a standard for others, and shall be remembered by me.

In the last, I would like to extend my gratitude to the Institute of Photonics and Quantum Sciences (IPaQS) at Heriot-Watt University, for providing me such a chance to pursue my PhD degree. This chance is precious and opens a new door for me after my career break.

Special thanks go to my beloved family for their love and great confidence in me. Their tremendous support is the key that I can finish this study.

# Table of contents

Abstract ..... ii

Dedication ..... iv

Acknowledgement ..... v

Table of contents ..... vi

Research Output ..... ix

Chapter 1 Introduction ..... 1

1.1 Metasurfaces ..... 1

1.2 Various types of metasurfaces ..... 1

1.3 Applications of metasurfaces ..... 3

1.3.1 Metalenses ..... 4

1.3.2 Metasurface holograms ..... 6

1.3.3 Generation of OAM beams ..... 9

1.3.4 Helicity-dependant beam steering ..... 13

1.3.5 Wavefront shaping of SPP ..... 15

1.3.6 Nonlinear metasurfaces ..... 16

1.4 Thesis structure ..... 17

1.5 References ..... 17

Chapter 2 Theory and Methods ..... 25

2.1 Geometric phase ..... 25

2.2 Highly efficient geometric metasurfaces ..... 26

2.2.1 Reflective plasmonic metasurfaces ..... 26

2.2.2 Dielectric metasurfaces ..... 29

2.3 Controlling the polarization state of the incident light..... 32

2.4 Device fabrication ..... 33

2.5 Summary ..... 34

2.6 References ..... 35

Chapter 3 Multichannel metasurface devices for phase control ..... 37

3.1 Generation of Orbital Angular Momentum beams. ..... 37

3.2 Superposition of OAM states ..... 38

3.3 Computer Generated Hologram ..... 42

3.4 Multichannel metasurface for simultaneous control of holograms and twisted light beams..... 43

3.4.1 Design ..... 43

3.4.2 Results ..... 48

3.4.3 Discussion ..... 52

3.5 Multichannel Metasurfaces for controllable OAM superpositions ..... 54

3.6 Summary ..... 60

3.7 References ..... 61

Chapter 4 Metasurface devices for polarization manipulation ..... 65

4.1 Introduction ..... 65

4.2 Malus law ..... 65

4.3 Hiding a grayscale image in the laser beam through a reflective metasurface .... 66

4.3.1 Design and method ..... 66

4.3.2 Sample fabrication ..... 69

4.3.3 Results ..... 70

4.4 Hiding a QR code for anti-counterfeiting purpose ..... 77

4.5 Encoding a colour image into the laser beam through a dielectric metasurface ..... 82

4.6 Summary ..... 89

4.7 References ..... 89

Chapter 5 Simultaneous control of phase and polarization ..... 91

5.1 Introduction ..... 91

5.2 Results ..... 92

5.3 Discussion ..... 98

5.4 Conclusion ..... 99

5.5 References ..... 100

Chapter 6 Summary and outlook ..... 102

6.1 Summary ..... 102

6.2 Outlook ..... 103

6.3 References ..... 106

# Research Output

Journal papers:

1. C. Zhang, et al, Multichannel metasurface for simultaneous control of holograms and twisted light beams, ACS Photonics, 4, 1906, 2017.
2. C. Zhang, et al, Optical Metasurface generated vector beam for anti-counterfeiting, Phys. Rev. Applied, 10(3), 034028, 2018.
3. C. Zhang, et al, Development of polarization speckle based on random polarization phasor sum, Journal of the Optical Society of America A, 36(2) 277, 2019.
4. C. Zhang, et al, Image-switchable metasurface hologram with hidden images, submitted to Nano Letters (under review).
5. F. Yue, C. Zhang, et al, High-resolution grayscale image hidden in a laser beam, Light: Science & Applications, 7, 2018, 17129.
6. H. Zhao, C. Zhang, et al, Linear and circular polarization multiplexing metasurface for optical image encryption, Laser & Photonics Review, submitted (Equal contribution).
7. F. Yue, D. Wen, C. Zhang, et al, Multichannel polarization-controllable superpositions of orbital angular momentum states, Advanced Materials, 29(15), 1603838, 2017.
8. D. Wen, F. Yue, C. Zhang, et al, Plasmonic metasurface for optical rotation, Applied Physics Letters 111, 023102, 2017.
9. Z. Zhang, D. Wen, C. Zhang, et al, Multifunctional light sword metasurface lens, ACS Photonics, 18, 2024, 2017.
10. X. Zang, F. Dong, F. Yue, C. Zhang, et al, Polarization encoded color image embedded in a dielectric metasurface. Advanced Materials, 30(21), 1707499, 2018.

Talks:

11. Simultaneous control of holograms and OAM states by using one metasurface, SSOP4, France, September 2017.
12. Metasurface devices for polarization and phase control, Chongqing University of Post and Communications, May 2018.
13. Phase and polarization manipulation by using one metasurface device, Capital Normal University, June 2018.

Honors and rewards:

14. Winner of Santander Mobility Grant 2016.
15. Winner of SUPA Early Career and Postdoc Exchange Program 2018, for the visit to Beijing Key Laboratory of Metamaterials and Devices, at Capital Normal University, China, from 11/05/18 to 15/06/18.

# Chapter 1 Introduction

Metamaterials are manmade materials, which allow engineers to design materials with electromagnetic properties unavailable in nature [1-5]. Natural materials are made of atoms, while the metamaterials are made of the artificial building blocks that can be tailored at will. The unusual properties of metamaterials have attracted considerable interest from all over the world, leading to many breakthrough works, including invisibility cloaking[1], superimaging [2, 3] and negative refraction [4]. Although metamaterials have brought new concepts and new ideas, the application of metamaterials in the optical range (especially visible light) has been hindered by the fabrication challenge of three-dimensional (3D) nanostructures. Metasurfaces are two-dimensional (2D) counterparts of metamaterials, which consist of single or several layers of artificial structures. In this chapter, we are going to review the current progress of metasurfaces and their applications in the ultrathin optical devices.

## 1.1 Metasurfaces

Metasurfaces, the planar metamaterials, can reduce the complexity of the fabrication process comparing with that of the 3D metamaterials. The fabrication of metasurfaces is compatible with semiconductor processing, making the application of metamaterials in the optical range more practical. The typical structures used in the optical metasurfaces are 2D nanostructures with various shapes of metallic or dielectric antennas, whose dimensions are smaller than the operating wavelengths, leading to the high resolution and the elimination of higher diffraction orders (in comparison with traditional diffractive optical components). Additionally, the thickness of metasurfaces is much smaller than the incident wavelength, which would be beneficial to device miniaturization and system integration.

The extraordinary capability of optical metasurfaces in the local manipulation of the light's amplitude, phase and polarization has led to various applications in imaging, security, optical communication, quantum sciences and fundamental scientific research. The most well-known examples include Snell's law of reflection and refraction, photonics Spin Hall Effect, metalenses, holograms, and so on.

## 1.2 Various types of metasurfaces

One of the milestone works of phase-gradient metasurface was demonstrated by Capasso's group[5]. When shined by the linearly polarized light, V-shaped antennas with various arm lengths and opening angles can introduce a phase gradient to the cross-

polarized light, which verifies the generalized laws of reflection and refraction. A two-dimensional array of V-shaped antennas (Fig.1-1a) is used to produce a linear phase gradient distribution (Fig 1-1b). Anomalous reflection and refraction phenomena were observed by patterning periodic distributed nanoantennas, where each unit cell consists of eight different V-shaped antennas which can cover the [0, 2π] phase range. The generalized laws of reflection and refraction from Fermat's principle were proposed and the experimental demonstration of an optical vortex (Fig.1-1d) was realized.

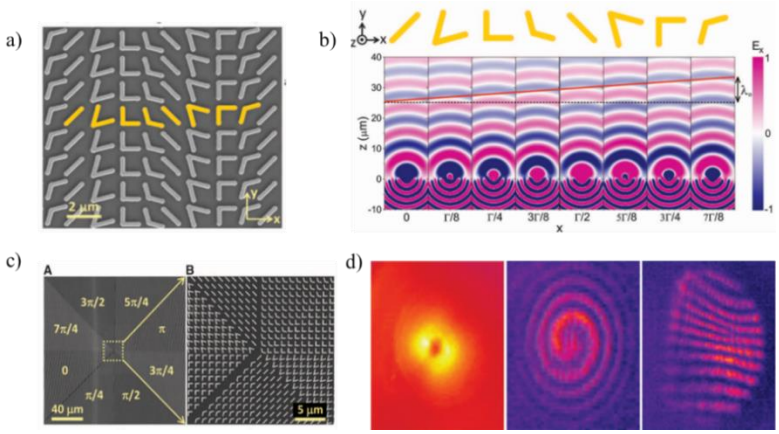


**Figure 1-1 The phase-gradient metasurface using V-shaped antennas[5]. a)** Scanning electron microscope (SEM) image of an antenna array fabricated on a silicon wafer. The unit cell of the plasmonic interface (yellow) consists of eight gold V shaped antennas. **b)** Schematic of the unit cell of the plasmonic and the FDTD simulations of the scattered electric field for each individual antennas. **c)** SEM image of a plasmonic interface. To generate a helical wavefront, the antennas are arranged which varies azimuthally from 0 to 2π. **d)** Experimental results of the designed optical vortex.

Metasurfaces based on the Pancharatnam-Berry (PB, see Chapter 2.1) phase are associated with the change of polarization state of light. Huang et al. investigated dispersionless phase discontinuity by using the dipole nanorods (Fig1-2))[6]. In this approach, each dipole nanorod can be treated as an anisotropic scatterer which converts part of the incident circularly polarized (CP) light to its opposite helicity with an extra phase brought in whose absolute value equals to two times of the orientation angle of the dipole. Therefore, by arranging the orientation of array of dipoles, a phase function can be introduced to the scattered light. The abrupt phase change is generated when a right circularly polarized (RCP) light beam is converted to its opposite helicity. An optical vortex beam with topological charge of one was demonstrated experimentally. Although this kind of optical metasurface device can work in the broadband (Fig1-2b), the efficiency is very low even at the resonance wavelength. To tackle the challenge of low efficiency while maintaining the property of broadband, the reflective metasurfaces were

proposed. This type of metasurface consists of three layers: the nanorods on the top, the metallic film at the bottom and the dielectric sandwiched in the middle. Each nanorod along with the top and bottom layer functions as a reflective-type half-wave plate, which can dramatically increase the efficiency and broadband.

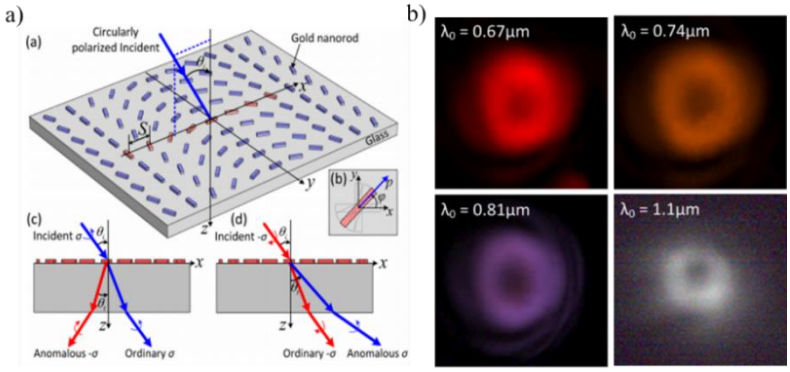


**Figure 1-2 Metasurface consists of nanorods with spatially variant orientations**[6]**. a)** Schematic illustrations of a refractive type dipole array, including the schematic illustration of a representative dipole array (eight dipoles in the top image), excitation of dipole moment when one dipole is illuminated with the azimuth angle φ along the x-axis, schematic illustration of normal and anomalous refraction by dipole arrays when left and right circularly polarized light impinges on the sample, respectively. **b)** Experimental results of optical vortexes with different wavelengths of incident light illuminated on the sample.

Apart from V-shaped structures and rod structures, other structures have also been developed in the last several years (see Fig1-3). Among these structures, metasurfaces consisting of dielectric nanopillars are very attractive since they are highly efficient and compatible with most optical systems (transmission type). Each nanopillar functions as a half waveplate, which can realize the polarization rotation of the linearly polarized light and can generate PB phase for the incident light with circular polaritons. In this thesis, we will mainly focus on two types of metasurfaces, i.e., reflective-type metasurface consisting of sandwich structures and dielectric metasurfaces consisting of spatially variant orientations. More details of PB phase generation based on the two types of metasurfaces will be discussed in Chapter 2.

## 1.3 Applications of metasurfaces

Metasurfaces have attracted considerable attention due to their ultrathin nature, ease of fabrication and subwavelength resolution. Benefiting from the unprecedented capability in the light manipulation, a plethora of metasurface devices with unusual functionalities have been developed. In this part, we will focus on the applications in metalenses,

holograms, generation and manipulation of orbital angular momentum(OAM) beams, wavefront shaping of surface plasmon polariton (SPP), and nonlinear optics.

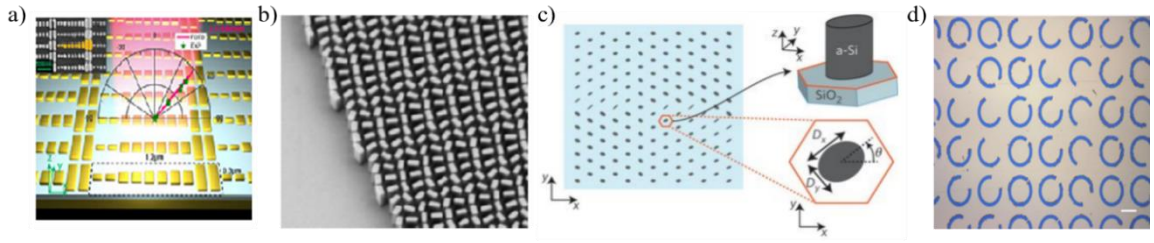


**Figure1-3 Metasurfaces with different shapes of basic unit.** a) Efficiency reaches 80% broadband anomalous reflection by gradient metasurfaces working in 750-900nm wavelength range[7]. b)The TiO2 nanofin structure based metalens which has high efficiency and high numerical aperture (NA) at the same time[8]. c) Top view of the elliptical silicon posts structure which has the same height, but different diameters ($D_x$ and $D_y$) and orientations ($\theta$). Insets: schematic three-dimensional view of an amorphous silicon post and its magnified top view[9]. d) Micrograph of the fabricated C-shape antenna structure[10].

### 1.3.1 Metalenses

Traditional lenses are designed based on the light propagation, which is typically realized by controlling the surface topography. In contrast, metasurface lenses (metalenses) are designed based on the abrupt phase change at the interface within a deep-subwavelength range, therefore they can decrease the thickness and volume of the lenses, along with a series of new functionalities which are not even possible for the traditional lenses, such as multiple functionalities.

Metalenses have the potential to replace the bulky, curved lenses that are currently used in the optical system. Fig.1-4 shows various metalenses. Fig.1-4a shows the phase profile of a near-infrared ($\lambda$ = 1550 nm) metalens consisting of eight V-antennas in each unit [11]. The SEM image (left) of one part of this matalens and measured diffraction-limited irradiance in the focal region (right) are shown at the bottom area. Fig.1-4b is the schematic illustration of a polarization-dependent metalens[12]. When a right circularly polarized light impinges on the lens, it is a convex lens, which will be changed to a concave lens when the handedness of the incident light is changed from right-handed to left-handed circular polarization. Fig.1-4c is an example of a cylindrical lens which can focus the incident light into a focal line. Fig.1-4d shows the breakthrough work in metalenses based on TiO2 nanofin structures, which have high efficiency and high numerical aperture (NA) [8]. In the visible range, the efficiency of the single layer plasmonic metalens is relatively low because of Ohmic losses and the difficulty of eliminating the zeroth order. By using the high aspect ratio dielectric nanopillars, such as TiO2 nanofins fabricated on a glass substrate, the efficiency can be greatly improved.

Each nanofin can be treated as a birefringent antenna, where the birefringence is induced by the asymmetric cross section of nanofins. In this work, by carefully designing the geometry of these nanofins, the conversion efficiency can reach 66%, 73%, and 86%, at 660 nm, 405 nm and 532nm, respectively. Light of different colors travels at different speeds in different materials and structures. A traditional lens can therefore not focus light of different colors to a single spot due to dispersion. More recently, a flat metasurface lens is developed which can focus different colors of any polarization to the same focal point [13] , as shown in Fig.1-4e. Fig.1-4f shows a metalens that has multiple longitudinal focal points with different polarization states [14].

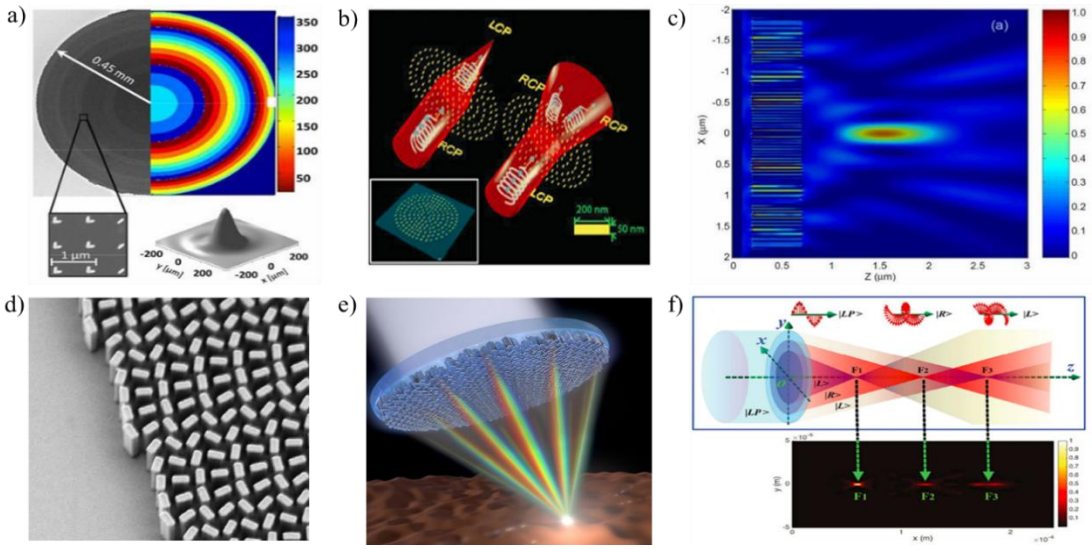


**Figure1-4 Examples of different metalens. a)** Phase profile of a near-infrared (λ = 1550 nm) metalens utilizing eight V-antennas. Shown in the bottom are the measured diffraction-limited irradiance in the focal region (right) and an SEM image of a portion of the metalens (left) [11]. b) Schematic of the reversible 3D focusing lens. Top: the expected realized phase profile of one the metalenses for right circularly polarized incident light [12]. c) Simulated normalized Poynting vector distribution at λ = 650 nm for a metalens consisting of an array of 65 silver slits with a fixed depth of 500 nm and widths ranging from 10 nm to 70 nm. The lens functions as a cylindrical lens, focusing the incident light into a line [12]. d) The SEM image of the dielectric metasurface based on TiO2 nanofins [8]. e) A single metasurface lens which can focus the entire visible spectrum of light to the same spot, and in high resolution [13]. f) Multi-foci lens that converges the scattered LCP light to points F1 and F3, and it also focuses the scattered RCP light to F2 [14].

Multifunctional metalenses can combine two or more functions onto a single device. As an example, Fig.1-5a shows the design procedure of how a positive cylindrical lens and a negative spherical lens is merged together[14], and the corresponding experimental results is given in Fig.1-5b. When the incident light is RCP, this device works as a cylindrical lens, and when the incident is LCP, is it a spherical lens. It is possible to

include two arbitrary phase functions in the multifunctional metasurface, as shown in Fig.1-5c where the device works as a lens(RCP incidence) or a hologram of a cat(LCP incidence)[14]. If two arrays of silicon nanofins are interlaced row by row so that they focus the LCP and RCP light to the corresponding off-axis points, chiral imaging can be realized, where two images with opposite helicity of an object are formed simultaneously.

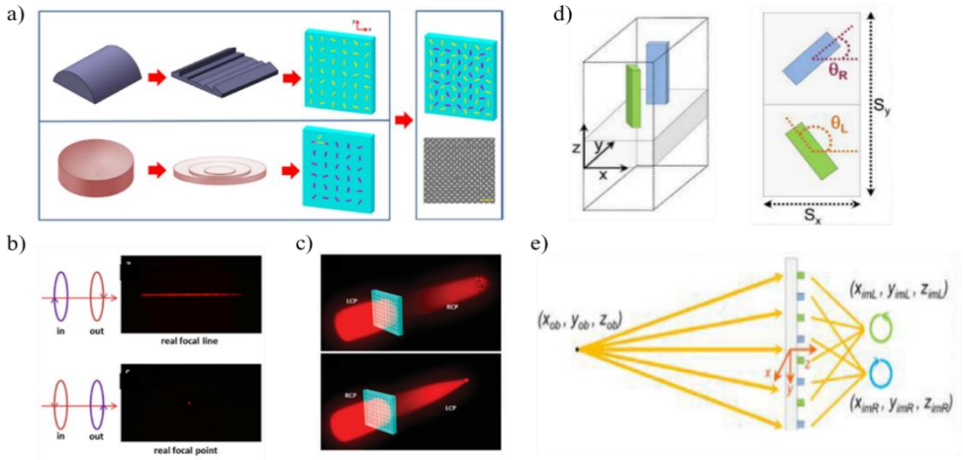


**Figure 1-5 Multifunctional metalenses** (a) Schematic of the multifunctional lenses. The phase functions of the positive cylindrical lens and the negative spherical lens are encoded on the yellow and purple nanorods, respectively[14]. (b) The experimental results for the multifunctional lens[14]. (c) The metasurface combines a lens and a hologram of a 'cat'.[15]. (d) The basic building block of the multispectral chiral lens. The blue and green nanofins contribute to the functionalities required for the RCP and LCP imaging, respectively[16]. e) Schematic demonstration of the chiral lens, where the RCP and LCP light from the target point is focused to two different points[16].

Furthermore, metalenses fabricated on the stretchable polydimethylsiloxane substrates can continuously tune the focal length[17]. By using the phase-changing material $Ge_3Sb_2Te_6$, each lens can interact with the substrate selectively depending on its amorphous or crystalline state when two cylindrical metasurface lenses are integrated together[18]. The flexibly of the phase control offered by geometric metasurface paves the way for metalenses with arbitrary focusing property, such as multiple off-axis focusing[19, 20] and multifocal metalens with conic shapes[21], or even the combination of lens and other optical element.

### 1.3.2 Metasurface holograms

The traditional two-beam hologram is the recorded interference pattern of the scattered light. It produces an amplitude hologram through which the scattered wavefront is directly recorded through the intensity of the interference pattern. If the intensity variations in the interference pattern is interpreted into the phase variation, a phase

hologram can be obtained which increases the brightness of the hologram image[22, 23].

Computer generated holograms (CGH) are digital format holograms. The phase profile of phase-only CGH is normally controlled by etching different depths into a dielectric substrate or grayscale lithography[24]. Because of their ease of fabrication, two-level binary CGHs have widely been used in many areas such as optical scanning, particle trapping, virtual reality etc. Recently metasurfaces have been used to realize CGHs[25-29] in an easier and efficient way, and more often with incredible performances, such as high efficiency[30], wide angle[28], and so on. In the content that follows, some examples of metasurface holograms have been picked up from the publications and presented in Fig.1.6.

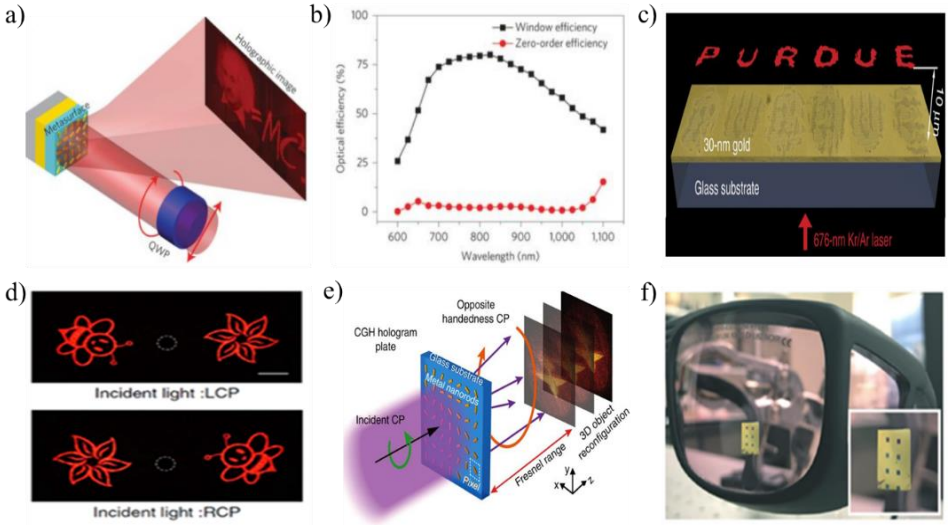


**Figure 1-6 Metasurface holograms. a)** Schematic illustration of a reflective-type metasurface hologram. It was reported that the efficiency can reach 80% at 825 nm, as shown in the measured conversion efficiency in **b)**[30]. **c)** Ultra-thin (30 nm) metasurface hologram which operates in the visible range[29]. **d)** The experimental results (bee and flower) of helicity-dependent metasurface holograms [31]. **e)** High-resolution on-axis three dimensional holography by using metasurfaces consisting of subwavelength metallic nanorods, where the phase can be continuously controlled by the rod orientation in each subwavelength unit cell [27]. f**)** Conformable metasurfaces on a safety glass[32].

Fig.1-6a is the schematic illustration of the reflective type metasurface hologram[30]. The famous mass-energy equivalence and the image of Albert Einstein were chosen as the target images of the hologram. In the design of this CGH, the conversion efficiency, signal-to-noise ratio and the uniformity were well considered as figure of merit. Instead of 8 phase levels, 16 phase levels were used to obtain the high performance from the CGH. The experimental results show that the diffraction efficiencies of this geometric metasurface hologram reaches 80% at the wavelength of 825nm, and a broad

bandwidth ranging from 630 nm to 1050nm, as shown in Fig.1-6b. This work combines the advantages of the phase profile control offered by a geometric metasurface and the reflective design to achieve the high polarization conversion efficiency. In the work shown in Fig.1-6c, an ultra-thin metasurface hologram which operate in the visible range is realized. The thickness of the gold layer on top of the glass base is only 30nm which is approximately 1/23 of the operational wavelength[29]. This hologram can provide not only the phase, but also amplitude of the incident light potentially can be efficiently manipulated. Fig.1-6d is the experimental results of a helicity multiplexed metasurface hologram with both high efficiency and good image fidelity over a broad range of frequencies[31]. In this piece of work, the authors combine two sets of hologram pattern operating with opposite helicities of the circularly polarized incident light. Gerchberg−Saxton algorithm[33] is used to retrieve the phase profile for this phase-only hologram. When the polarization states of the incident light changes from RCP to LCP, or the other way around, two symmetrically distributed off-axis images (flower and bee) flip. In Fig.1-6e, an on-axis three-dimensional hologram with a wide field of view is realized by using a metasurface made of subwavelength metallic nanorods with spatially-variant orientations. The 3D jet can be regarded as a collection of 2D images subsequently arranged in the longitudinal direction.

Apart from the hologram shown above, metasurfaces have also been used to demonstrate color holograms, especially in the visible wavelength range [8, 38, 39] where three primary colors (red, green and blue) need to be integrated into one singe metasurface. An ultrathin plasmonic metasurface hologram has been demonstrated, as shown in Fig.1-7a[34]. The designed metasurface consists of subwavelength nanoslits for the reconstructing of two and three dimensional full color holographic image. It is worth mentioning that this hologram offers both amplitude and phase modulations at the subwavelength scale and produces three primary colors and their secondary colors. Fig.1-7b is the schematic illustration of an angular multiplexed multicolor hologram[35]. During the design process, the target image is first decomposed into its R, G, B components, then in order to form a new target image, the positions of these three primary colors are properly arranged. Next, the phase distribution of the hologram is calculated by using the well-known Gerchberg-Saxton algorithm, and each pixel is then encoded into the orientation angle of the corresponding nanoslit. The image with correct colors can be obtained when the off-axis illumination of the red, green and blue laser is adopted. The angular multiplexing can also be applied by assigning different phase shifts to the R,

G, B parts of the hologram, the corresponding tilted incident light beams can reconstruct the R, G, B image in the designed observation zone[34]. Apart from the angular multiplexing method, a more straightforward way to realize color holograms is to find out three types of nanoantennas which filter out the R, G, B components separately, as shown in Fig.1-7c[36] and Fig.1-7d[37].

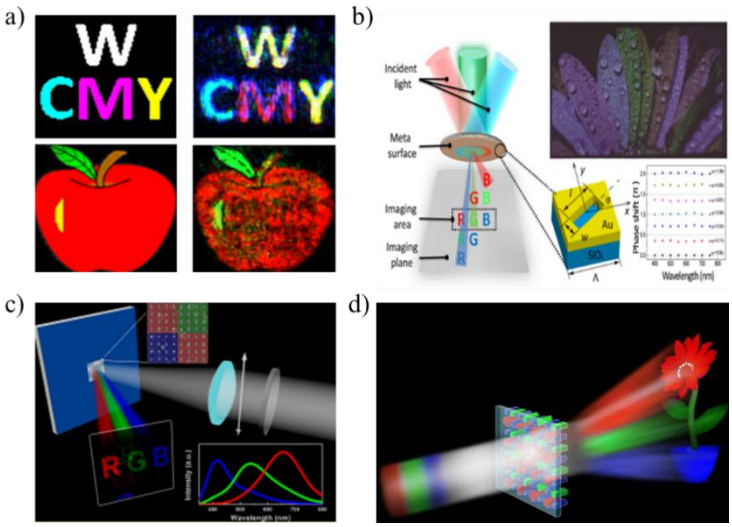


**Figure 1-7 Metasurface based color hologram. a)** Reconstruction of 2D holographic images which contains primary and secondary colors. Left: original 2D object, and Right: experimentally reconstructed holographic images[34]. **b)** Left: Schematic illustration of the multicolor hologram under the illumination of laser beams with different incident angles. The zoom-in area shows a gold nanoslit antenna. Top right: Experimental results. Bottom right: Simulated geometric phase of the light scattered by an antenna with orientation angle $\varphi$[35]. **c)** Polarization-dependent Phase-modulated multicolor metasurface hologram which can produce images in three primary colors. Inset: intensity profile over the visible range for three primary color [36]. **d)** Three types of silicon antennas are adopted in the design of metasurface to independently manipulate the R, G, B components.[37].

Matesurfaces have provided a novel approach to realize holograms with special features such as subwavelength pixel size and continuous phase levels which make them suitable for 3D holography and color holography, leading to the new functionalities and significant increase of the information capacity[40].

### 1.3.3 Generation of OAM beams

Apart from spin angular momentum(SAM), a light field can carry OAM that is associated with the phase of the optical field[41]. Different from the value of SAM which can be ± ħ per photon, OAM can process ± $m$ħ per photon[42], here $m$ can be any integer and it is called topological charge, which is the number of the twist in one wavelength. The higher the topological charge is, the faster the wavefront of the light beam is spinning. The

intensity, phase and wavefront of the beam with topological charge of 1, 2 and 3 are demonstrated in Fig.1-8.

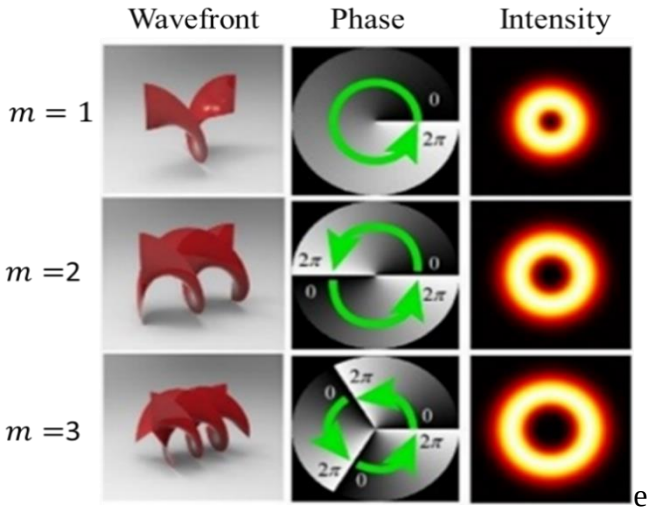

e

**Figure 1-8 The wavefront, phase and intensity profile of light beam with topological charges of 1, 2 and 3, respectively[43].**

Although there have been many methods and technical approaches [44-46] to generate the OAM beams, the systems are often either bulky, or have low resolution, which has prevented their applications in the system integration. Thanks to the advances in the nanofabrication process which has enable the metasurfaces to manipulate the light wavefront at subwavelength resolution. In recent years, metasurfaces have been used to generate the OAM[5, 6, 47-52], spin-to-orbital conversion[53, 54] and manipulation[55], or do other OAM manipulations, such as the generation of vortex beam[5, 6, 47] and OAM superposition[56, 57].

By controlling the geometric parameters of the unit cell of the metasurface, OAM can be generated and controlled at will [6, 47, 53, 58, 60, 61]. For example, a plasmonic metasurface using L-shaped nanoantennas can transfer the SAM to the OAM[47], as shown in Fig.1-9c. The well-known milestone work in this area by the research group in Harvard University, an OAM beam with topological charge of one is demonstrated in 2011 by carefully designing the parameters of V-shape antennas so that a helical phase can be introduced to the light beam[5]. A three-dimensional volumetric optical vortices generator is realized by using the dielectric nanopattern (Fig.1-9f). To generate the vortex arrays needed, the concepts of spiral Dammann zone plates and Dammann vortex gratings are used here[59].

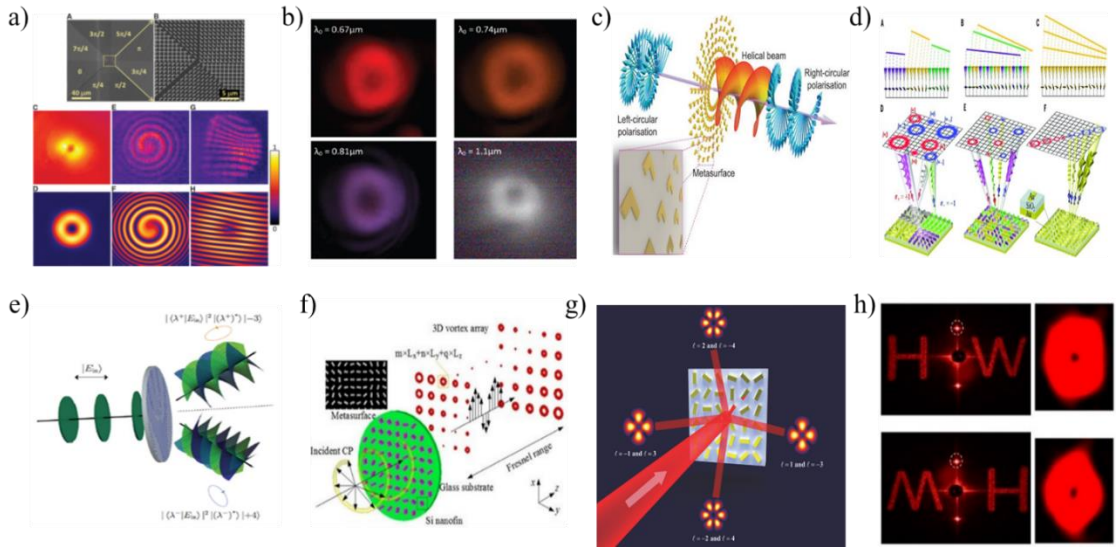


**Figure 1-9. Metasurfaces for the generation and manipulation of OAM beams. a)** SEM image of a plasmonic interface consists of V-shaped antennas that creates an optical vortex with topological charge of one[5]. **b)** Measured intensity distribution of the vortex beam patterns for wavelengths from 670 to 1100 nm[6]. **c)** Schematic of spin-to-orbit coupling through a metasurface consisting of L-shaped nanoantennas [47]. **d)** The schematic illustration of the shared-aperture concepts [48]. **e)** Generation of two vortex beams with topological charges -3 and -4 from two orthogonal SAM states with elliptical polarizations [58]. **f)** Dielectric metasurface for the generation and reconstruction of a 3D vortex array through [59]. **g)** Schematic of off-axis multi-OAM generation and superposition [56]. **h)** The measured results of holograms and OAM beams generated from a single metasurface device. Both the two hologram images and the sign of two OAM beams ($m = 1$ and $m = -1$) are closely related to the helicity of the incident beam[57].

A method which converts the elliptically polarized incident light to two independent OAM beams. By introducing an additional constant phase gradient, these two independent OAM states can also be spatially separated by an angle of ±10°, as reported in Ref[58]. Benefiting from their capabilities of arbitrary control of phase profile of light beam, metasurfaces have practical applications in the integrated system.

Metsurfaces can not only be used to generate the desirable OAM states, but also provides an elegant way to control the superposition of two OAM beams, or more in a multichannel manner. We experimentally demonstrated a metasurface platform to realize polarization-controllable multichannel superpositions of vortex beams with various topological charges[56]. Under the RCP incident light, four OAM states with topological charges ranging from 1 to 4 are generated at the same time. By controlling the polarization state of the incident light, superpositions of different OAM states are realized in four different channels. In the case of linearly or elliptically polarization incidence, the superpositions such as m=3(RCP) and m=-1(LCP), m=1(RCP) and m=-3(LCP) will be realized in one direction, and similarly other two superpositions can be realized at the orthogonal

direction, as illustrated in Fig.1-9g. Based on this, we further developed a metasurface device with tunable functionalities including polarization-controllable hologram generation and superposition of orbital angular momentums[57]. Fig.1-9h presents the experimental results of holograms and vortex beams.

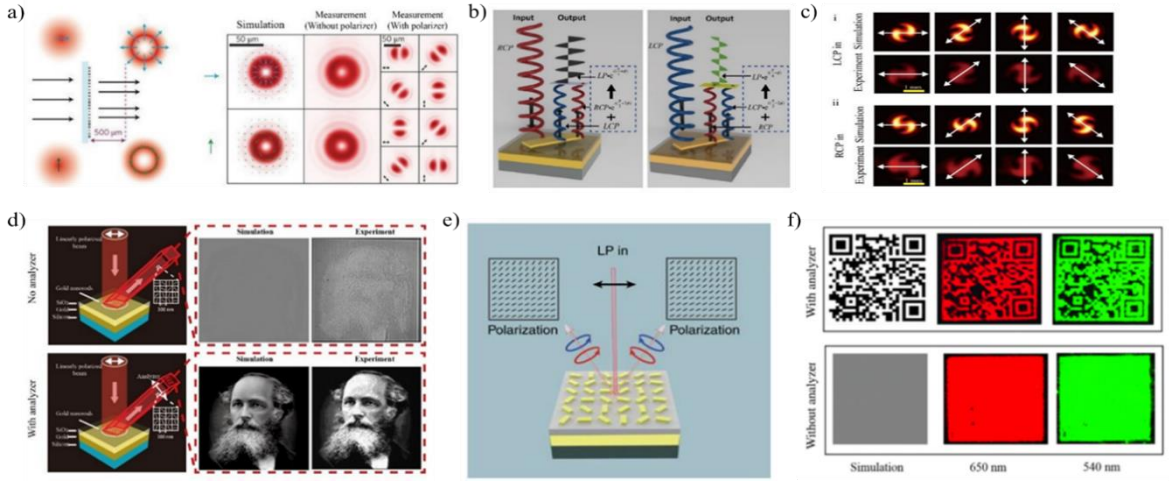


**Figure 1-10** (a) Radially and azimuthally polarized cylindrical vector beams. These light beam were obtained by the same metasurface that can provide two incident light beams with orthogonal polarization states [9]. (b) Schematic of polarization and phase evolution of emerging light on a single unit of the metasurface [64]. (c) Simulation and experimental results after the vector vortex beam passing through an analyser [64]. (d) Schematic illustration of hiding a high-resolution grayscale image into the polarization profile of the light [65]. The image can be resolved by an analyzing polarizer. Under the illumination of a light beam with linear polarization, the two beams with opposite handedness of circularly polarized light will interfere with each other, which can generate the required polarization profile for the hidden image, as shown in e). f) Simulation and measured results of QR code hidden to the light, for color light of red and green [66].

Apart from the phase and amplitude modification, metasurfaces are also used to control the polarization profile of the light, which further shows their capabilities in the control of the light, and possible applications, e.g., vector beams[9, 62-65] and vector OAM beams generation[66], and image hiding[67, 68]. In 2015, Arbabi et al. demonstrated a metasurface device to generate a cylindrical vector beam. In this work, by locally manipulating the polarization profile of the light, both azimuthal and radial vector beams were generated from two orthogonal linearly polarized beams[9] (Fig.1-10a). Chen group demonstrated a reflective-type plasmonic metasurface which can produce a vector vortex beam[66]. In this work, the vector vortex beams were generated from the superposition of two circularly polarized components that are the converted parts when the incident light is reflected from the metasurface(Fig.1-10b). The ‘s’ pattern verifies that such a beam carries OAMs (Fig.1-10c).

A metasurface approach is demonstrated later which is based on the polarization manipulation. In this work [67], we have successfully demonstrated an approach to hide a high-resolution grayscale image of 1300x1300 pixels into a laser beam with the spatial-variant polarization states(Fig.1-10d). The hidden image can be revealed (or not), depending on the angles between the transmission axes of the two polarizers which are located before and after the metasurface sample, respectively. This approach has provided a route to control the polarization profile of the light, offering a unique approach to image encryption, and can be used in the information security, anticounterfeiting and other similar fields.

### 1.3.4 Helicity-dependant beam steering

As stated above, light can carry both spin and orbital momentum, which are determined by the polarization and spatial degrees of freedom of the light. The spin-orbit interaction of light refers to the optical phenomenon in which the spin (circular polarization) affects and controls light's spatial degrees of freedom, e.g., its intensity distribution and propagation path[69].

Upon the illumination of the CP light, a metasurface will introduce a phase gradient $d\varphi/dx$ to converted part of the beam, while the non-converted part remain unchanged. The phase gradient will change to $-d\varphi/dx$ if the handedness of the light beam is changed[6]. Therefore, for the linearly or elliptically polarized incident light, the converted RCP and LCP components will be shifted to their mirrored positions. Fig1-11a shows a method to determine the polarization state of the incident light based on the intensities of the refracted light spots[70]. The LCP and/or RCP are steered in two directions by the designed metasurface which consist of nanorods with spatial-variant orientations.

By using dielectric metasurfaces [73], the CP light splitting also has a higher conversion efficiency(Fig.1-11b). Outside of the visible wavelength range, even higher conversion efficiency can be achieved by using the metasurfaces, such as nearly 100% in the microwave range[74], and 70% in near infrared(NIR) [75]. Fig.1-11c is another example to shift circularly polarized beams to both sides by using the nanorod arrays with the same orientations along x direction and different orientations along y direction. Cheng et al. proposed few-layer metasurfaces which can dramatically expand the functionalities of plasmonic metasurfaces[76].These metasurfaces can produce waveguide modes[77, 78], Fabry-Pérot resonances[79] and near field interaction[80] between layers. A reflective metasurface was proposed to develop highly-efficient metadevices[81]. When the incident beam shines onto the devices from forward and backwards, the metasurface will

play different roll in spin conversion and reflection, which were used to achieve asymmetric transmission(Fig.1-11d) [72]. This design approach has been extended to acoustic metasurfaces[82]. Moreover, with accurate control of the incident angles and phase of the CP light, the intensity of the refracted light can be dynamically tuned (Fig.1-12a-b).

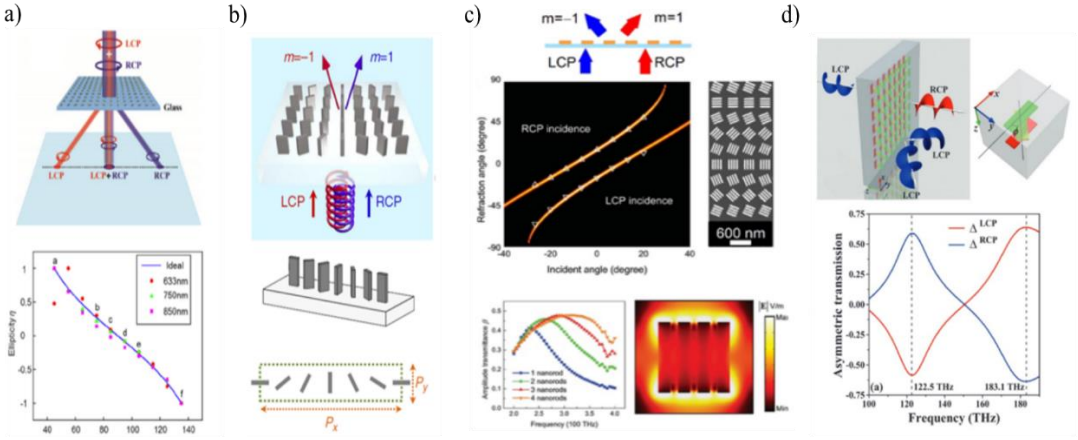


**Figure 1-11.** (a) Beam steering for polarization measurement. Top: schematic. Bottom: Measured ellipticity of the incident light [70]. (b) Metasurface consisting of amorphous silicon nanofins [76]. Top: schematic. Middle: There are six nanofins in a supercell. Bottom: The length and width of the supercell. (c) Top: Schematic. Middle: The deflection angles of LCP and RCP light beams at various angles. Bottom: The efficiency and operation bandwidth of the plasmonic metasurfaces will increases when the number of nanorods in a unit cell goes up [71]. (d) Top: Schematic. Bottom: Simulation results of the transmission efficiency for the incident light with LCP and RCP [72].

It is worth mentioning here that graphene can produce plasmonic resonances [86], leading to the spin dependent beam steering. Graphene nanocrosses were proposed to achieve beam steering in the infrared range [84](Fig.1-12c-d). One of the advantages of the graphene-based metasurface is that the intensity of the refracted light changes dynamically with the Fermi level of graphene. The metasurfaces based on graphene working at the deep sub-wavelength scale can realize high-order optical modulation (e.g., high-order diffraction), as shown in (Fig.1-12e) and vector beams[85] as the plasmonic resonances generation is still possible even when the size of graphene nanostructure is as small as $\lambda/80$.

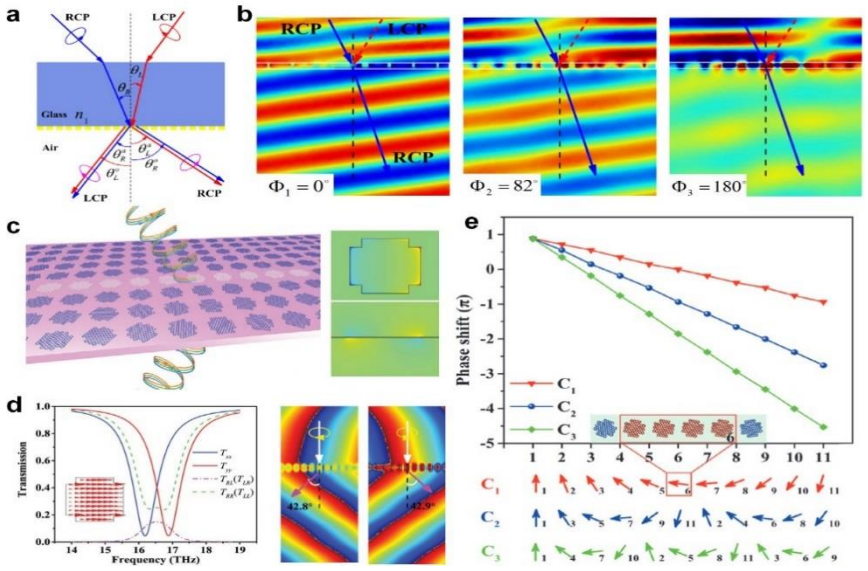


**Figure 1-12** (a) Dynamic control of the strength of the anomalously refracted light [83]. (b) Distribution of the electric field for incident light with RCP for various relative phases[83]. (c) Graphene for metasurface [84]. (d) Transmission spectra of graphene nanostructures for linearly and circularly polarized incident light [84]. (e) Phase shift of various graphene groups. The nanoantennas are similar to those in (c-d) with smaller size[85].

### 1.3.5 Wavefront shaping of SPP

Surface plasmon polaritons (SPPs) refers to the excitation of collective motion of conduction band electrons on the metal/dielectric interfaces [32]. SPPs have been widely explored in the scientific fields of physics, biology and so on, leading to different applications such as photonic biochemical sensors[87], nonlinear optics[88, 89], sub-diffractional imaging[90] and many more. In many applications it is essential to control the process of coupling the free space photons to SPPs. The main techniques such as prism coupling, and periodic corrugations have been used for the realization of momentum matching between the free space photons and SPPs. However, these techniques either provide symmetric SPP waves in two directions, meaning there are two SPPs propagating along opposite directions, or are not suitable for coupling light to compact integrated plasmonic devices.

Except the wavefront manipultation in free space shown above, a metasurfaces can also shape the SPP wavefront by linking SPPs with light. By using the spin-dependent phase gradient generated by a metasurface, the unidirectional excitation of SPPs were realized[91].

As shown in Fig.1-13a, when a circularly polarized light beam shines on a metasurface, the propagation direction of the excited SPPs can be controlled helicity of the light [91]. It is interesting that SPPs which propagate along two directions can occur when incident

light has elliptical or linear polarizations, which makes the unidirectional excitation of SPPs possible and offer another degree of freedom for SPP excitation [92].

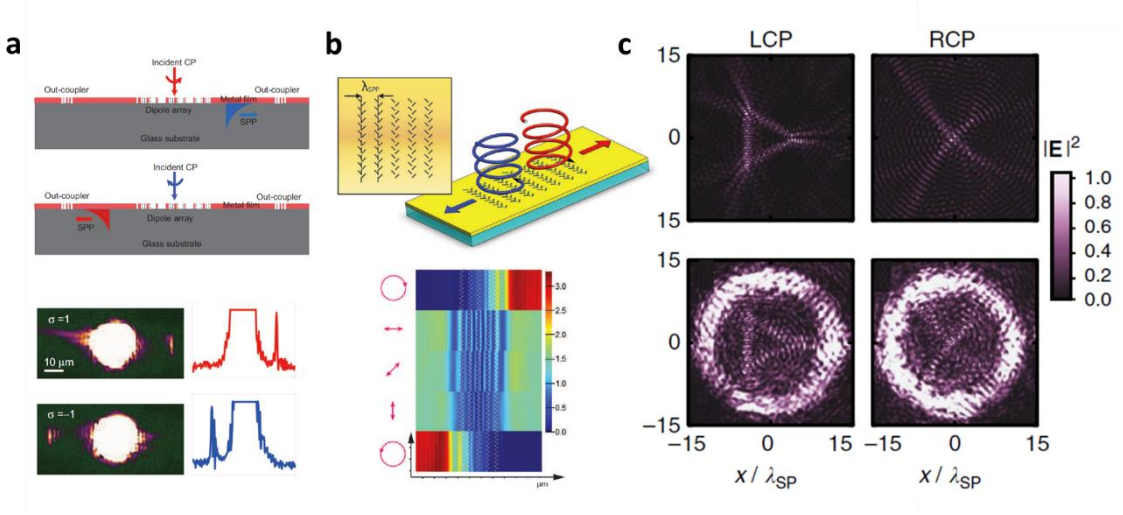


**Figure 1-13** (a) Schematic of the unidirectional SPPs excitation (top) and measured results (bottom) [91]. (b) The nanoslit pairs (top) are used to couple the incident light to opposite directions. Bottom: The dependence of the near-field distribution on polarization states[92]. (c) Simulated results (top) and experimental results (bottom) for RCP and LCP light [93].

The unidirectional excitation of SPPs were also realized with nanoapertures in the metallic film [92]. For incident light with circular polarization states, the phase of the SPP wave can be shifted using nanoslits with spatially-variant orientations [93]. The nanoslits function as the helicity-dependent unidirectional coupler (Fig.1-13b) [92]. The nanorods sitting on a graphene layer can also unidirectionally excite plasmons[94]. Similar to CGHs, the SPP wave profile can work as a target image and the metasurface work as a hologram coupler. Based on the phase matching, two SPP beams can meet with each other and reconstruct spin-dependent profiles for SPPs (Fig.1-13c) [93, 95].

### 1.3.6 Nonlinear metasurfaces

The capability of metasurface in the manipulation of light propagation has been extended to nonlinear optics, providing new opportunities for the realization of nonlinear optical devices. The efficient nonlinear generation can be based on the metasuface paradigm. Specific optical properties on demand can be obtained with metasurfaces by carefully engineering the nanoantennas (e.g., shape and spatial arrangement).

In comparison with 3D structures, the nonlinear metasurfaces (2D) are easier to fabricate and have exhibited excellent nonlinear optical responses in a more compact footprint. In the recent years various types of nonlinear metasurface devices with unusual functionalities have been developed. Examples include harmonic generation based on the continuous control of the nonlinearity phase[96], nonlinear metasurface hologram based

on the spin and wavelength multiplexing[97]and nonlinear metasurface devices for OAM manipulation[98]. Nonlinear metasurfaces have provided new opportunities for nonlinear optics, enabling the efficient, robust and miniaturized nonlinear optical devices available for fundamental research.

## 1.4 Thesis structure

There are totally six chapters in this thesis. Chapter one is the introduction part where the brief concept of metasurface is given, followed by the review of the recent research and development in this dynamic field. The theory involved in this thesis is presented in Chapter two. Given the fact that the main work of this thesis is experiment based, the brief introduction of the nanofabrication and the details of sample fabrication are presented as well. Chapter three to five shows in detail the research work done by the candidate and her co-workers. Chapter three focuses on the phase manipulation, followed by polarization control in Chapter four. In Chapter five, one single metasurface is demonstrated for the purpose of controlling of both phase and polarization state of light. In each of these three chapters, the design method, sample fabrication, simulation and experimental results are given in detail. In the last chapter of the thesis, the author summarizes all the work.

## 1.5 References


1. Pendry, J.B., D. Schurig, and D.R. Smith, *Controlling electromagnetic fields.* science, 2006. **312**(5781): p. 1780-1782.

2. Liu, Z., et al., *Far-field optical hyperlens magnifying sub-diffraction-limited objects.* science, 2007. **315**(5819): p. 1686-1686.

3. Fang, N., et al., *Sub–diffraction-limited optical imaging with a silver superlens.* Science, 2005. **308**(5721): p. 534-537.

4. Shelby, R.A., D.R. Smith, and S. Schultz, *Experimental verification of a negative index of refraction.* science, 2001. **292**(5514): p. 77-79.

5. Yu, N., et al., *Light Propagation with Phase Discontinuities: Generalized Laws of Reflection and Refraction.* Science (Washington), 2011. **334**(6054): p. 333-337.

6. Huang, L., et al., *Dispersionless phase discontinuities for controlling light propagation.* Nano letters, 2012. **12**(11): p. 5750-5755.

7. Sun, S., et al., *High-efficiency broadband anomalous reflection by gradient meta-surfaces.* Nano letters, 2012. **12**(12): p. 6223-6229.

8. Khorasaninejad, M., et al., *Metalenses at visible wavelengths: Diffraction-limited focusing and subwavelength resolution imaging.* Science, 2016. **352**(6290): p. 1190-1194.

9. Arbabi, A., et al., *Dielectric metasurfaces for complete control of phase and polarization with subwavelength spatial resolution and high transmission.* Nature nanotechnology, 2015. **10**(11): p. 937-943.

10. Zhao, H., et al., *Demonstration of orbital angular momentum multiplexing and demultiplexing based on a metasurface in the terahertz band.* ACS Photonics, 2017. **5**(5): p. 1726-1732.

11. Aieta, F., et al., *Aberration-free ultrathin flat lenses and axicons at telecom wavelengths based on plasmonic metasurfaces.* Nano letters, 2012. **12**(9): p. 4932-4936.

12. Chen, X., et al., *Dual-polarity plasmonic metalens for visible light.* Nature communications, 2012. **3**: p. 1198.

13. Shrestha, S., et al., *Broadband Achromatic Dielectric Metalenses Concise running title: Achromatic Metalenses.* Light: Science & Applications, 2018. 7: 85.

14. Wen, D., et al., *Multifunctional metasurface lens for imaging and Fourier transform.* Scientific reports, 2016. **6**: p. 27628.

15. Wen, D., et al., *Metasurface device with helicity-dependent functionality.* Advanced Optical Materials, 2016. **4**(2): p. 321-327.

16. Khorasaninejad, M., et al., *Multispectral chiral imaging with a metalens.* Nano letters, 2016. **16**(7): p. 4595-4600.

17. Ee, H.-S. and R. Agarwal, *Tunable metasurface and flat optical zoom lens on a stretchable substrate.* Nano letters, 2016. **16**(4): p. 2818-2823.

18. Yin, X., et al., *Beam switching and bifocal zoom lensing using active plasmonic metasurfaces.* Light: Science & Applications, 2017. **6**(7): p. e17016.

19. Li, R., et al., *Arbitrary focusing lens by holographic metasurface.* Photonics Research, 2015. **3**(5): p. 252-255.

20. Chen, X., et al., *Ultrathin metasurface laser beam shaper.* Advanced Optical Materials, 2014. **2**(10): p. 978-982.

21. Bao, Y., et al., *Enhanced optical performance of multifocal metalens with conic shapes.* Light: Science & Applications, 2017. **6**(10): p. e17071.

22. Rogers, G.L., *XIV.—Experiments in Diffraction Microscopy.* Proceedings of the Royal Society of Edinburgh Section A: Mathematics, 1952. **63**(3): p. 193-221.

23. Cathey, W., *Three-dimensional wavefront reconstruction using a phase hologram.* JOSA, 1965. **55**(4): p. 457-457.

24. Freese, W., et al., *Design of binary subwavelength multiphase level computer generated holograms.* Optics letters, 2010. **35**(5): p. 676-678.

25. Larouche, S., et al., *Infrared metamaterial phase holograms.* Nature materials, 2012. **11**(5): p. 450.

26. Chen, W.T., et al., *High-efficiency broadband meta-hologram with polarization-controlled dual images.* Nano letters, 2013. **14**(1): p. 225-230.

27. Huang, L., et al., *Three-dimensional optical holography using a plasmonic metasurface.* Nature communications, 2013. **4**: p. 2808.

28. Yifat, Y., et al., *Highly efficient and broadband wide-angle holography using patch-dipole nanoantenna reflectarrays.* Nano letters, 2014. **14**(5): p. 2485-2490.

29. Ni, X., A.V. Kildishev, and V.M. Shalaev, *Metasurface holograms for visible light.* Nature communications, 2013. **4**: p. 2807.

30. Zheng, G., et al., *Metasurface holograms reaching 80% efficiency.* Nature nanotechnology, 2015. **10**(4): p. 308.

31. Wen, D., et al., *Helicity multiplexed broadband metasurface holograms.* Nature communications, 2015. **6**: p. 8241.

32. Burch, J., et al., *Conformable holographic metasurfaces.* Scientific Reports, 2017. **7**(1): p. 4520.

33. Gerchberg, R.W., *A practical algorithm for the determination of phase from image and diffraction plane pictures.* Optik, 1972. **35**: p. 237-246.

34. Wan, W., J. Gao, and X. Yang, *Full-color plasmonic metasurface holograms.* ACS nano, 2016. **10**(12): p. 10671-10680.

35. Li, X., et al., *Multicolor 3D meta-holography by broadband plasmonic modulation.* Science advances, 2016. **2**(11): p. e1601102.

36. Huang, Y.-W., et al., *Aluminum plasmonic multicolor meta-hologram.* Nano letters, 2015. **15**(5): p. 3122-3127.

37. Wang, B., et al., *Visible-frequency dielectric metasurfaces for multiwavelength achromatic and highly dispersive holograms.* Nano letters, 2016. **16**(8): p. 5235-5240.

38. Choudhury, S., et al., *Pancharatnam–Berry phase manipulating metasurface for visible color hologram based on low loss silver thin film.* Advanced Optical Materials, 2017. **5**(10): p. 1700196.

39. Devlin, R.C., et al., *Broadband high-efficiency dielectric metasurfaces for the visible spectrum.* Proceedings of the National Academy of Sciences, 2016. **113**(38): p. 10473-10478.

40. Huang, L., et al., *Broadband hybrid holographic multiplexing with geometric metasurfaces.* Advanced Materials, 2015. **27**(41): p. 6444-6449.

41. Barnett, S.M., L. Allen, and M.J. Padgett, *Optical angular momentum*. 2016: CRC Press.

42. Mair, A., et al., *Entanglement of the orbital angular momentum states of photons.* Nature, 2001. **412**(6844): p. 313.

43. Yue, F., *Geometric optical metasurface for polarization control*. 2017, Heriot-Watt University.

44. Rumala, Y.S., et al., *Tunable supercontinuum light vector vortex beam generator using a q-plate.* Optics letters, 2013. **38**(23): p. 5083-5086.

45. Cardano, F., et al., *Polarization pattern of vector vortex beams generated by q-plates with different topological charges.* Applied Optics, 2012. **51**(10): p. C1-C6.

46. Beresna, M., et al., *Radially polarized optical vortex converter created by femtosecond laser nanostructuring of glass.* Applied Physics Letters, 2011. **98**(20): p. 201101.

47. Karimi, E., et al., *Generating optical orbital angular momentum at visible wavelengths using a plasmonic metasurface.* Light: Science & Applications, 2014. **3**(5): p. e167.

48. Maguid, E., et al., *Photonic spin-controlled multifunctional shared-aperture antenna array.* Science, 2016: p. aaf3417.

49. Mühlenbernd, H., et al., *Amplitude-and phase-controlled surface plasmon polariton excitation with metasurfaces.* ACS Photonics, 2016. **3**(1): p. 124-129.

50. Jin, J., et al., *Generation and detection of orbital angular momentum via metasurface.* Scientific reports, 2016. **6**: p. 24286.

51. Chen, C.-F., et al., *Creating optical near-field orbital angular momentum in a gold metasurface.* Nano letters, 2015. **15**(4): p. 2746-2750.

52. Pu, M., et al., *Catenary optics for achromatic generation of perfect optical angular momentum.* Science Advances, 2015. **1**(9): p. e1500396.

53. Devlin, R.C., et al., *Spin-to-orbital angular momentum conversion in dielectric metasurfaces.* Optics express, 2017. **25**(1): p. 377-393.

54. Bouchard, F., et al., *Optical spin-to-orbital angular momentum conversion in ultra-thin metasurfaces with arbitrary topological charges.* Applied Physics Letters, 2014. **105**(10): p. 101905.

55. Li, G., et al., *Spin-enabled plasmonic metasurfaces for manipulating orbital angular momentum of light.* Nano letters, 2013. **13**(9): p. 4148-4151.

56. Yue, F., et al., *Multichannel Polarization-Controllable Superpositions of Orbital Angular Momentum States.* Advanced Materials, 2017. **29**(15): p. 1603838.

57. Zhang, C., et al., *Multichannel metasurface for simultaneous control of holograms and twisted light beams.* ACS Photonics, 2017. **4**(8): p. 1906-1912.

58. Devlin, R.C., et al., *Arbitrary spin-to–orbital angular momentum conversion of light.* Science, 2017. **358**(6365): p. 896-901.

59. Huang, L., et al., *Volumetric generation of optical vortices with metasurfaces.* Acs Photonics, 2017. **4**(2): p. 338-346.

60. Kang, M., et al., *Twisted vector field from an inhomogeneous and anisotropic metamaterial.* JOSA B, 2012. **29**(4): p. 572-576.

61. Yang, Y., et al., *Dielectric meta-reflectarray for broadband linear polarization conversion and optical vortex generation.* Nano letters, 2014. **14**(3): p. 1394-1399.

62. Chen, H., et al., *Generation of vector beams based on dielectric metasurfaces.* Journal of Modern Optics, 2015. **62**(8): p. 638-643.

63. Chen, H., et al., *Generation of double-ring-shaped cylindrical vector beams by modulating Pancharatnam–Berry phase.* Optik-International Journal for Light and Electron Optics, 2017. **134**: p. 227-232.

64. Zhou, J., et al., *Spin-dependent manipulating of vector beams by tailoring polarization.* Scientific reports, 2016. **6**: p. 34276.

65. Yi, X., et al., *Generation of cylindrical vector vortex beams by two cascaded metasurfaces.* Optics express, 2014. **22**(14): p. 17207-17215.

66. Yue, F., et al., *Vector vortex beam generation with a single plasmonic metasurface.* ACS photonics, 2016. **3**(9): p. 1558-1563.

67. Yue, F., et al., *High-resolution grayscale image hidden in a laser beam.* Light: Science & Applications, 2018. **7**(1): p. 17129.

68. Zhang, C., et al., *Optical Metasurface Generated Vector Beam for Anticounterfeiting.* Physical Review Applied, 2018. **10**(3): p. 034028.

69. Bliokh, K.Y., et al., *Spin–orbit interactions of light.* Nature Photonics, 2015. **9**(12): p. 796.

70. Wen, D., et al., *Metasurface for characterization of the polarization state of light.* Optics express, 2015. **23**(8): p. 10272-10281.

71. Liu, Z., et al., *High-performance broadband circularly polarized beam deflector by mirror effect of multinanorod metasurfaces.* Advanced Functional Materials, 2015. **25**(34): p. 5428-5434.

72. Liu, J., et al., *High-Efficiency Mutual Dual-Band Asymmetric Transmission of Circularly Polarized Waves with Few-Layer Anisotropic Metasurfaces.* Advanced Optical Materials, 2016. **4**(12): p. 2028-2034.

73. Khorasaninejad, M. and K.B. Crozier, *Silicon nanofin grating as a miniature chirality-distinguishing beam-splitter.* Nature communications, 2014. **5**: p. 5386.

74. Luo, W., et al., *Transmissive ultrathin Pancharatnam-Berry metasurfaces with nearly 100% efficiency.* Physical Review Applied, 2017. **7**(4): p. 044033.

75. Li, Z., et al., *Manipulation of the Photonic Spin Hall Effect with High Efficiency in Gold-Nanorod-Based Metasurfaces.* Advanced Optical Materials, 2017. **5**(20): p. 1700413.

76. Cheng, H., et al., *Emergent functionality and controllability in few-layer metasurfaces.* Advanced Materials, 2015. **27**(36): p. 5410-5421.

77. Li, J., et al., *Bidirectional perfect absorber using free substrate plasmonic metasurfaces.* Advanced Optical Materials, 2017. **5**(12): p. 1700152.

78. Li, J., et al., *Simultaneous control of light polarization and phase distributions using plasmonic metasurfaces.* Advanced Functional Materials, 2015. **25**(5): p. 704-710.

79. Grady, N.K., et al., *Terahertz metamaterials for linear polarization conversion and anomalous refraction.* Science, 2013, 340(6138): p. 1304-1307.

80. Yu, P., et al., *Controllable optical activity with non-chiral plasmonic metasurfaces.* Light: Science & Applications, 2016. **5**(7): p. e16096.

81. Li, Z., et al., *Simultaneous generation of high-efficiency broadband asymmetric anomalous refraction and reflection waves with few-layer anisotropic metasurface.* Scientific reports, 2016. **6**: p. 35485.

82. Xie, B., et al., *Coding acoustic metasurfaces.* Advanced Materials, 2017. **29**(6): p. 1603507.

83. Liu, Z., et al., *Fully interferometric controllable anomalous refraction efficiency using cross modulation with plasmonic metasurfaces.* Optics Letters, 2014. **39**(23): p. 6763-6766.

84. Cheng, H., et al., *Dynamically tunable broadband infrared anomalous refraction based on graphene metasurfaces.* Advanced Optical Materials, 2015. **3**(12): p. 1744-1749.

85. Wang, C., et al., *Dynamically Tunable Deep Subwavelength High-Order Anomalous Reflection Using Graphene Metasurfaces.* Advanced Optical Materials, 2018. **6**(3): p. 1701047.

86. Ju, L., et al., *Graphene plasmonics for tunable terahertz metamaterials.* Nature nanotechnology, 2011. **6**(10): p. 630.

87. Anker, J.N., et al., *Biosensing with plasmonic nanosensors*, in *Nanoscience And Technology: A Collection of Reviews from Nature Journals*. 2010, World Scientific. p. 308-319.

88. Kauranen, M. and A.V. Zayats, *Nonlinear plasmonics.* Nature Photonics, 2012. **6**(11): p. 737.

89. Noskov, R., A. Krasnok, and Y.S. Kivshar, *Nonlinear metal–dielectric nanoantennas for light switching and routing.* New Journal of Physics, 2012. **14**(9): p. 093005.

90. Kawata, S., Y. Inouye, and P. Verma, *Plasmonics for near-field nano-imaging and superlensing.* Nature Photonics, 2009. **3**(7): p. 388.

91. Huang, L., et al., *Helicity dependent directional surface plasmon polariton excitation using a metasurface with interfacial phase discontinuity.* Light: Science & Applications, 2013. **2**(3): p. e70.

92. Lin, J., et al., *Polarization-controlled tunable directional coupling of surface plasmon polaritons.* Science, 2013. **340**(6130): p. 331-334.

93. Xiao, S., et al., *Flexible coherent control of plasmonic spin-Hall effect.* Nature Communications, 2015. **6**: p. 8360.

94. Zhu, B., et al., *Graphene circular polarization analyser based on unidirectional excitation of plasmons.* Optics Express, 2015. **23**(25): p. 32420-32428.

95. Xu, Q., et al., *Polarization-controlled surface plasmon holography.* Laser & Photonics Reviews, 2017. **11**(1): p. 1600212.

96. Li, G., et al., *Continuous control of the nonlinearity phase for harmonic generations.* Nature Materials, 2015. **14**(6): p. 607.

97. Ye, W., et al., *Spin and wavelength multiplexed nonlinear metasurface holography.* Nature Communications, 2016. **7**: p. 11930.

98. Li, Z., et al., *Tripling the capacity of optical vortices by nonlinear metasurface.* Laser & Photonics Reviews, 2018. **12**(11): p. 1800164.

# Chapter 2 Theory and Methods

In the first chapter, we reviewed the current progress of metasurfaces and their applications in various fields. In this chapter, we will discuss the theory and methods that are closely related to the metadevices in the thesis. We will concentrate on the generalized geometric phase, highly efficient geometric metasurfaces, dynamic control of the polarization state of the incident light, and the fabrication procedures of metasurface devices that we have developed.

## 2.1 Geometric phase

A geometric phase can be achieved when a polarized light beam undergoes a closed loop on the Poincaré sphere. The geometric phase equals to half of the solid angle in the closed loop on the Poincaré sphere. This was initially proposed by Pancharatnam[1, 2] and further developed by Berry[3, 4]. Therefore, the geometric phase associated with polarization manipulation was called Pancharatnam-Berry (PB) phase, which can be realized with optical metasurfaces such as metasurfaces consisting of nanorods[5] or nanopillars[6] with spatially variant orientations. To describe the space-variant birefringence property of the metasurface, the Jones matrix can be used as follows.

$$T = R(\theta)^{-1}\begin{bmatrix} t_x & 0 \\ 0 & t_y e^{i\delta} \end{bmatrix} R(\theta) \qquad (2\text{-}1)$$

Where $R(\theta)$ is the rotation matrix, $\theta(x,y)$ is the orientation angle of the optical axis, $t_x$ and $t_y$ are the transmission amplitudes of TE and TM components, and δ is the phase retardation. For an incident light with an arbitrary polarization state $|E_{in}\rangle$, the output light beam $|E_{out}\rangle$ can be decomposed into three parts, based on two orthogonal circular polarization states.

$$|E_{out}>=\sqrt{\tau_E}|E_{in}>+\sqrt{\tau_R}e^{i2\theta}|R>+\sqrt{\tau_L}e^{-i2\theta}|L> \qquad (2\text{-}2)$$

$\tau_E$, $\tau_R$ and $\tau_L$ are the coefficients of each component, which are governed by the following equations.

$$\tau_E = |0.5(t_x + t_y e^{i\delta})|^2 \qquad (2\text{-}3)$$

$$\tau_R = |0.5(t_x - t_y e^{i\delta}) < L|E_{in}>|^2 \qquad (2\text{-}4)$$

$$\tau_L = |0.5\left(t_x - t_y e^{i\delta}\right) < R|E_{in} > |^2 \qquad (2\text{-}5)$$

Where $|R>$ and $|L>$ represent the RCP and LCP, respectively. From Eq. (2-2), we can clearly see that the first part keeps the same polarization state as that of the incident light, while the second or third part undergoes a spin orbit momentum conversion associated with a phase change of $\pm 2\theta$, depending on the helicity of the incident light. This spin orbit momentum conversion can be understood from the point of conservation of angular momentum. If we neglect the absorption and material loss, upon the illumination of a pure circularly polarized light beam, the conversion efficiency can reach 100% when the retardation is δ=π, meaning that the device functions as a perfect half waveplate. Helicity still changes, by conservation of momentum, beam should rotate about propagation axis.

It is well known that a single-layer plasmonic geometric metasurface has a very low efficiency[7]. To tackle this issue, reflective plasmonic metasurfaces consisting of three layers (nanorods on the top, metal film at the bottom and dielectric layer sandwiched between them) or dielectric metasurfaces consisting of nanopillars with spatially variant orientations can be adopted to realize the desirable phase modulation with high efficiency. To facilitate device fabrication, the above two types of geometric metasurfaces are the main focus of this thesis.

## 2.2 Highly efficient geometric metasurfaces

### 2.2.1 Reflective plasmonic metasurfaces

When metallic nanostructures are illuminated by light beam, the oscillation of free electrons at the structure surface can be exited due to the resonant electronic-electromagnetic oscillation. The output light can be modulated by the response of the localized plasmonic resonance. Although the resonance frequencies of gold and silver are within the visible range, these materials are highly dispersive, limiting their broadband performance. Fortunately, reflective plasmonic metasurfaces have provided an effective approach to tackle this bandwidth issue while maintaining high efficiency.

A typical reflective metasurface consists of three layers where a dielectric layer is sandwiched in between the top metallic nanostructure layer and bottom metal layer. In this structure the material dispersion of top and bottom metal (very often they are gold and silver) can be compensated by the thickness-dependent dispersion of the dielectric layer (e.g., silicon dioxide)[8]. Furthermore, the Fabry-Pérot effect of the multilayer configuration can dramatically enhance the conversion efficiency of the metasurface[9]. Suppose an incident light beam with an electric field $E_{in}$, the total output light beam will

be the superposition of all the reflected light beams from the nanostructure layer and the transmitted light after propagation in the dielectric layer(see Fig.2-1). The output light can be described as

$$\mathbf{E}_{out} = \mathbf{E}_1 + \mathbf{E}_2 + \mathbf{E}_3 + \mathbf{E}_4 + .... \qquad (2\text{-}6)$$

In order to derive the complex reflection and transmission coefficients at the interface between air and the nanostructure layer $r$ and $t$, and the interface between the nanostructure and the dielectric layer $r'$and $t'$. To simplify the theoretical model, the slice of ultrathin nanostructures can be considered as a homogeneous layer[10].

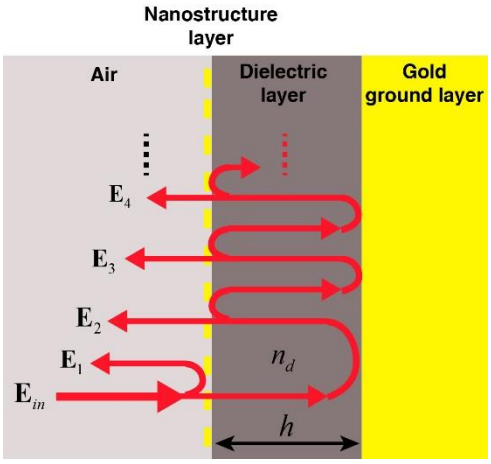


**Figure 2-1 Schematic of the multiple reflections from a reflective metasurface[11].**

The susceptibility of homogeneous layer is closely related to the polarizability of an individual structure

$$\chi_g = \frac{\alpha_g}{a^2 d} \qquad (2\text{-}7)$$

Where $d$ the thickness of nanostructure layer is, $\alpha_g$ is the polarizability of the antenna, which is assumed as $\alpha_g \propto \frac{1}{\omega - \omega_0 + i\gamma}$ due to the localized surface plasmon resonance of the antennas. If $d$ is sufficiently small, the complex coefficients for the reflection and transmission can be approximately derived as follows [10]

$$r = \frac{\frac{1-n_d}{2} + \frac{i}{2}\frac{k_0\alpha_g}{a^2}}{\frac{1+n_d}{2} - \frac{i}{2}\frac{k_0\alpha_g}{a^2}} \qquad (2\text{-}8)$$

$$t = \frac{1}{\frac{1+n_d}{2} - \frac{i}{2}\frac{k_0\alpha_g}{a^2}} \tag{2-9}$$

$$r' = \frac{\frac{n_d - 1}{2} + \frac{i}{2}\frac{k_0\alpha_g}{a^2}}{\frac{1+n_d}{2} - \frac{i}{2}\frac{k_0\alpha_g}{a^2}} \tag{2-10}$$

$$t' = \frac{n_d}{\frac{1+n_d}{2} - \frac{i}{2}\frac{k_0\alpha_g}{a^2}} \tag{2-11}$$

Let us suppose that all the light is reflected at the interface between the dielectric layer and metal layer at the bottom, but it will obtain a phase change of $\varphi$. Now, the total output light can be calculated by using the following equation.

$$\begin{aligned} \mathbf{E}_{out} &= \mathbf{E}_{in} r + \mathbf{E}_{in} tt' e^{i(2n_d k_0 h + \varphi)} + \mathbf{E}_{in} tt' r' e^{2i(2n_d k_0 h + \varphi)} + .... \\ &= \mathbf{E}_{in}\left(r + \frac{tt' e^{i2n_g k_0 h + \varphi}}{1 - r' e^{i2n_g k_0 h + \varphi}}\right) \end{aligned} \tag{2-12}$$

Due to the dispersion property of the middle dielectric layer, the dispersion of the coefficients can be cancelled by carefully designing the thickness $h$ of the dielectric layer. In addition, the Fabry-Pérot effect also plays an important role in the triple-layer configuration, which can greatly increase the conversion efficiency.

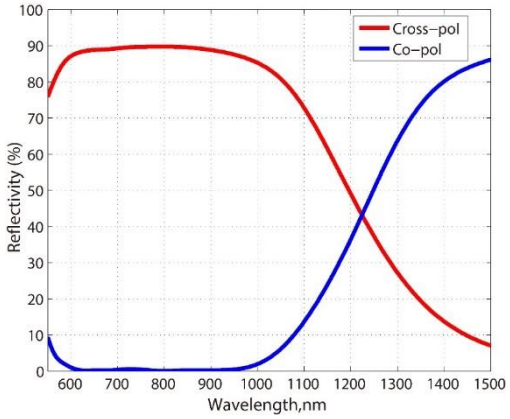


**Figure 2-2. Simulated conversion efficiency of a reflective metasurface[11].** Cross-pol and co-pol represent the converted and non-converted part of the output light, respectively.

In this thesis, CST Microwave Studio was used to calculate the conversion efficiency. Silicon dioxide was used as the dielectric layer and the Drude model was used for the gold. The Epsilon infinity, the plasma frequency and the collision efficiency are 1, $1.37 \times 10^{16}$ rad/s and $12.15 \times 10^{13}$ 1/s, respectively. In the calculation, each gold nanorod is 220 nm long, 80 nm wide, and 30 nm high. The thickness of the spacer layer ($SiO_2$) and the ground layer (gold) are 85 nm and 150 nm, respectively. The refractive index of $SiO_2$ is 1.45. The simulation result is shown in Fig.2-2.

### 2.2.2 Dielectric metasurfaces

Another type of highly efficient metasurfaces that we used in this thesis is the dielectric metasurface which consists of amorphous silicon nanopillars with spatially variant orientations. Fig.2-3a is the schematic illustration of dielectric metasurface for the linear polarization rotation. The Jones matrix of a silicon nanopillar with in-plane orientation angle of θ can be expressed as[12]:

$$\begin{aligned} T(\theta) &= R(-\theta)T_0(\theta)R(\theta) \\ &= \begin{bmatrix} cos\theta & -sin\theta \\ sin\theta & cos\theta \end{bmatrix} \begin{bmatrix} i\sqrt{\xi(\lambda)} & 0 \\ 0 & -i\sqrt{\xi(\lambda)} \end{bmatrix} \begin{bmatrix} cos\theta & sin\theta \\ -sin\theta & cos\theta \end{bmatrix} \\ &= i\sqrt{\xi(\lambda)} \begin{bmatrix} cos2\theta & sin2\theta \\ sin2\theta & -cos2\theta \end{bmatrix} \end{aligned} \tag{2-13}$$

where $T_0$ represents the Jones matrix of the silicon nanopillar without rotation, and R(θ) is the rotator operator. ξ(λ) is the conversion efficiency. For a linearly polarized light beam along the horizontal direction, it can be decomposed into a LCP light beam and a RCP light beam with equal intensities and zero initial phase. When a linearly polarized light beam along the horizontal direction shines on the nanopillar (see Fig.2-3a), the LCP light beam is partially converted into RCP light beam with an additional phase delay 2θ while the RCP light beam is partially converted into its opposite helicity with an additional phase delay -2θ. The corresponding transmitted electric field for each converted part can be expressed as follows:

$$E_{LCP/RCP} = i\sqrt{\frac{\xi(\lambda)}{2}} e^{\pm i2\theta} \begin{bmatrix} 1 \\ \mp i \end{bmatrix} \tag{2-14}$$

Since the converted parts have the same intensities and the opposite helicity, they are combined into a linearly polarized light beam which can be written as follows:

$$E_{con} = i\sqrt{\frac{\xi(\lambda)}{2}}e^{-i2\theta}\begin{bmatrix}1\\ i\end{bmatrix} + i\sqrt{\frac{\xi(\lambda)}{2}}e^{i2\theta}\begin{bmatrix}1\\ -i\end{bmatrix} = i\sqrt{\frac{\xi(\lambda)}{2}}\begin{bmatrix}\cos(2\theta)\\ \sin(2\theta)\end{bmatrix}, \quad (2\text{-}15)$$

This leads to the polarization rotation of 2θ for the converted linearly polarized light beam. If there are various nanopillars with different in-plane orientations on the metasurface (see Fig. 2-3(b)), a homogeneously incident light beam with linear polarization will be converted into an inhomogeneous polarization profile of the light beam, providing the desired polarization-rotating states for image encoding, as shown in Fig. 2-3(c).

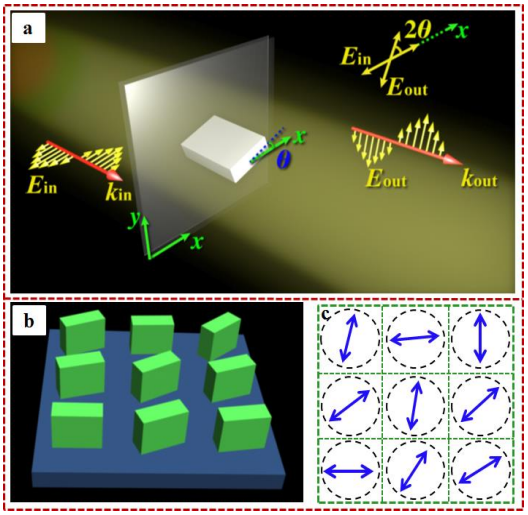


**Figure2-3 Polarization rotation generated by the dielectric metasurface[6].** (a)The polarization of a linearly polarized light beam is rotated by 2θ counterclockwise after passing through a nanopillar with in-plane orientation angle of θ. (b) nine nanopillars with different in-plane orientations on the metasurface can generate nine corresponding polarization states (c).

The performance (e.g., polarization purity and diffraction efficiency) of fabricated device is affected by the sample imperfection (e.g., nanopillar shape in Fig. 2-4) due to the fabrication imperfection. The conversion efficiency (polarization purity) is defined as the ratio between the optical power with desired polarization rotation and the transmitted power, while the diffraction efficiency is the ratio between the optical power with desired polarization rotation and the incident power [13], as shown in the equations below.

$$Conversion\ Efficiency = \frac{the\ power\ of\ converted\ part}{the\ transmitted\ power} \quad (2\text{-}16)$$

$$Diffraction\ Efficiency = \frac{the\ power\ of\ converted\ part}{the\ incident\ power} \quad (2\text{-}17)$$

The height of each nanopillar is 310 nm, which satisfies the phase retardation of a half waveplate ($\frac{2\pi}{\lambda} \cdot h \cdot \Delta n = \pi$ ). Fig. 2-5 and Fig.2-6 show the effect of the shape of silicon nanopillar on the conversionn efficiency and diffraction efficiency for red and blue colour

filtering, respectively. In the simulation in Fig.2-5 and Fig.2-6, the length of the nanopillar is changed from 140 (90) nm to 170 (120) nm, while the width is changed from 95 (65) nm to 115(85) nm for filtering red (green) light. P=360 nm, Ly'=0.9Ly, r1=0.5Ly, and r2=0.5Ly'. The numerical calculation of the conversion efficiency and diffraction efficiency is carried out by using the commercial microwave software CST Microwave Studio.

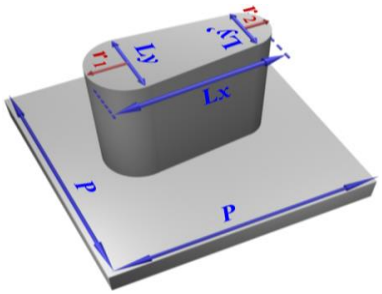


**Figure 2-4. Schematic of the nanopillar geometry[6].**

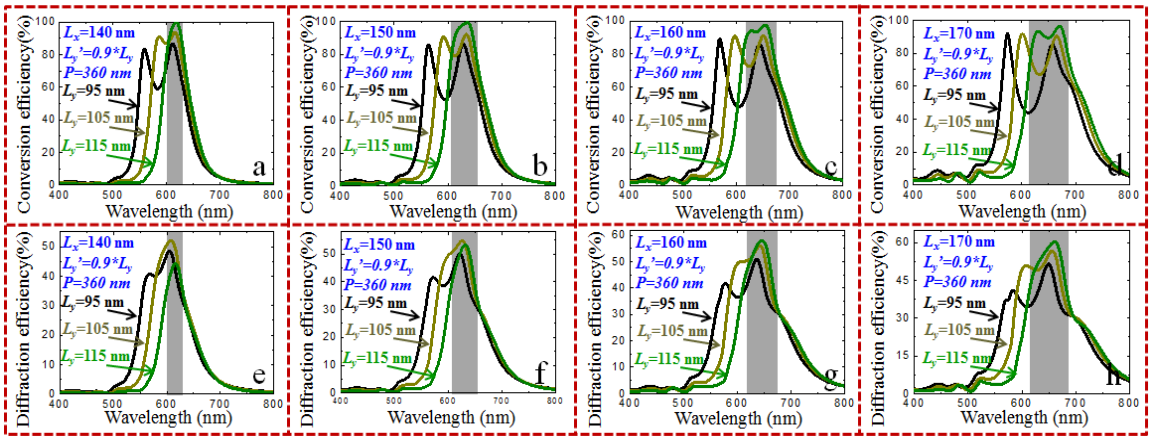


**Figure 2-5. The conversion efficiency and diffraction efficiency of nanopillars with various structure parameters for filtering red light[6].**

Fig.2-5 shows the polarization purity (conversion efficiency) and diffraction efficiency of nanopillars with different structure parameters. In Figs. 2-5(a)-(d), the response wavelength is gradually tuned from 600 to 680 nm when Lx (Ly) is changed from 140 (95) nm to 170 (115) nm, which means that the large nanopillar in the sample can perfectly filter red light in a wide wavelength range. The conversion efficiency (peak value) in this case is more than 80% in the range of the parameter variation. The response width becomes wider. The corresponding diffraction efficiency is given in Figs. 2-5(e)-(h) which indicated the same variation tendency with a diffraction efficiency over 40%. For the green light filtering, the length and width of the nanopillars are also changed with a variation range of 30 nm and 20 nm, respectively, as shown in Figs. 2-6(a)-(h).

The response wavelength is in the range of 490～575 nm for Lx (Ly) when it is changed from 90 (65) nm to 120 (85) nm. Our simulation results show that the metasurface exhibit color filtering functionality, but the peak conversion efficiency and diffraction efficiency are lower than the case of perfect structure parameters.

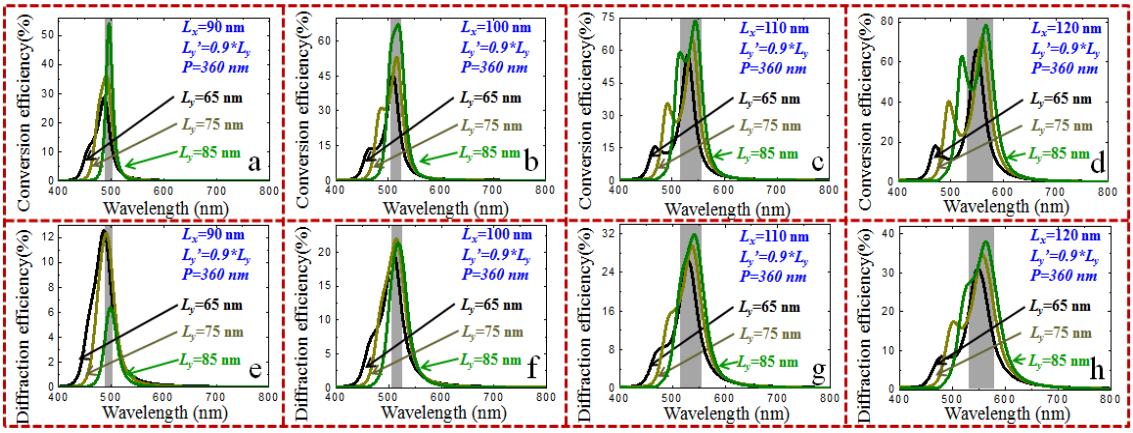


**Figure 2-6. The conversion efficiency and diffraction efficiency of nanopillars with various structure parameters for filtering green light[6].**

### 2.3 Controlling the polarization state of the incident light

In this thesis, various polarization states are generated by controlling the angle between the transmission axis of a linear polarizer and the fast axis of a quarter waveplate (QWP). Suppose the angle between the fast axis of QWP with respect to the x-axis is α. The Jones matrix of the QWP and Jones vector of the linearly polarized light in the x direction are $e^{-i\pi/4}\begin{pmatrix} cos^2\alpha + isin^2\alpha & (1-i)sin\alpha cos\alpha \\ (1-i)sin\alpha cos\alpha & sin^2\alpha + icos^2\alpha \end{pmatrix}$ and $\begin{pmatrix}1\\0\end{pmatrix}$, respectively. The Jones vector of the light beam after passing through the polarizer and the QWP can be written as follows.

$$\begin{aligned} & e^{-\frac{i\pi}{4}}\begin{pmatrix} cos^2\alpha + isin^2\alpha & (1-i)sin\alpha cos\alpha \\ (1-i)sin\alpha cos\alpha & sin^2\alpha + icos^2\alpha \end{pmatrix}\begin{pmatrix}1\\0\end{pmatrix} \\ &= e^{-\frac{i\pi}{4}}\begin{pmatrix} cos^2\alpha + isin^2\alpha \\ (1-i)sin\alpha cos\alpha \end{pmatrix} \\ &= \frac{a}{\sqrt{2}}\begin{pmatrix}1\\i\end{pmatrix} + \frac{b}{\sqrt{2}}\begin{pmatrix}1\\-i\end{pmatrix} \end{aligned} \tag{2-16}$$

Where $a = (1 - sin2\alpha - icos2\alpha)/2$ and $b = (1 + sin2\alpha - icos2\alpha)/2$ are the components of LCP and RCP light, respectively.

## 2.4 Device fabrication

In this thesis, a typical reflective metasurface is composed of three layers: a gold ground layer, a silicon dioxide (SiO2) spacer layer, and a top layer of gold nanorods. All the nanorods have the same geometry and spatial-variant orientations.

To demonstrate the fabrication process, the detail of how a typical sample is fabricated is given below. First, silicon substrates are cleaned with acetone in ultrasonic bath for 10 min, then followed by isopropyl alcohol (IPA) for 10 min. After that the substrates are rinsed in deionized water and dried with compressed air. Next step, the gold layer (150 nm) is deposited onto the silicon substrate by using the electron beam evaporator, followed by the deposition of silicon dioxide (SiO2) layer of 85nm. During the deposition process, the film thickness is controlled by using a calibrated film thickness monitor. Then the positive poly methyl methacrylate (PMMA) 950 A2 resist is spin coated on the SiO2 layer at 1000 rpm for 60s, then followed by 1500 rpm for 15s, producing a PMMA film with a thickness of 100 nm. After the PMMA is coated, the sample is then baked on a hotplate at 180oC for 5 mins. The designed nanopatterns are defined in the PMMA film using the standard electron-beam lithography (EBL, Raith PIONEER, 30KV). The sample is developed in MIBK: IPA (1:3) for 45 s followed by stopper (IPA) for 45 s. A thin gold layer (30 nm) is deposited on the developed sample using electron beam evaporator. For the adhesion purpose, a thin titanium layer (3 nm) is deposited on the SiO2 layer prior to the gold layer. Final step of the fabrication process is the lift-off process in acetone. Now the sample is ready for the characterization. Fig. 2-7 presents the SEM image of a typical reflective metasurface device that we have fabricated.

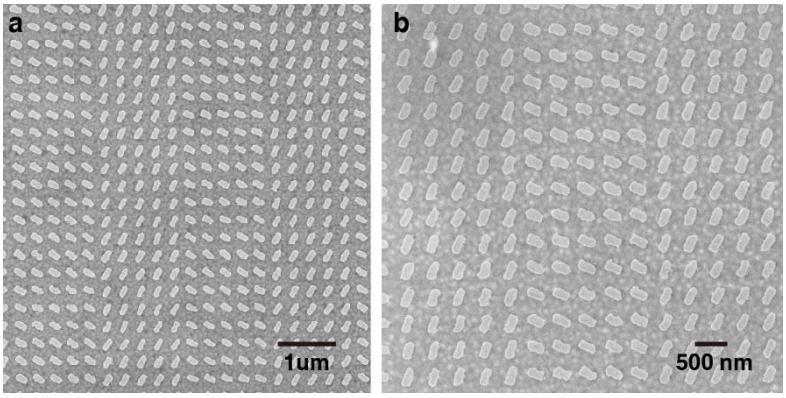


**Figure 2-7. The scanning electron microscope (SEM) images of a typical reflective metasurface.**

The dielectric metasurfaces we used in the thesis consist of amorphous silicon nanopillars with spatially variant orientations. Quartz substrates are used to fabricate the designed silicon nanopillars. First, an amorphous silicon film with a thickness of 310 nm is

deposited on the quartz substrate by using an Inductively Coupled Plasma Enhanced Chemical Vapor Deposition System (ICPECVD, Sentech SI 500D). Then, an electron beam evaporator is used to deposit an aluminum film with a thickness of 50 nm, which is used as a charge-dissipation layer and hard mask for etching. The positive electron beam resist (ZEP-520A) with a thickness of 200 nm is spin coated on the sample. After that, nanostructures are defined on the resist film based on the standard electron-beam lithography (EBL, Vistec EBPG 5000+). The nanopatterns are transferred into the aluminum layer and silicon layer by subsequent etching using an Inductively Coupled Plasma etcher (ICP, Sentech PTSA SI 500). Finally, the silicon nanopillars are obtained on the quartz substrate by removing the aluminum layer with aluminum etchant. Fig.2-8(a) shows the real and imaginary parts of the refraction index of the amorphous silicon film with a thickness of 310 nm. The samples consist of the amorphous silicon nanopillars on the quartz substrates. The scanning electron microscope (SEM) images of samples are given in Figs. 2-8(b) and 2-8 (c) (with a tilt angle), respectively[6].

### 2.5 Summary

In this chapter, we discussed the mechanism of geometric phase, highly efficient measurfaces, the effect of fabrication error on the performance of the dielectric metasurface, the dynamic control of polarization state of the input light and fabrication procedures of a typical metasurface devices. Theoretical analysis is essential during the design process and plays an important role when we try to improve the performance of the designed devices. From next chapter, we will focus on the development of the novel metasurface devices for the purpose of phase and polarization control.

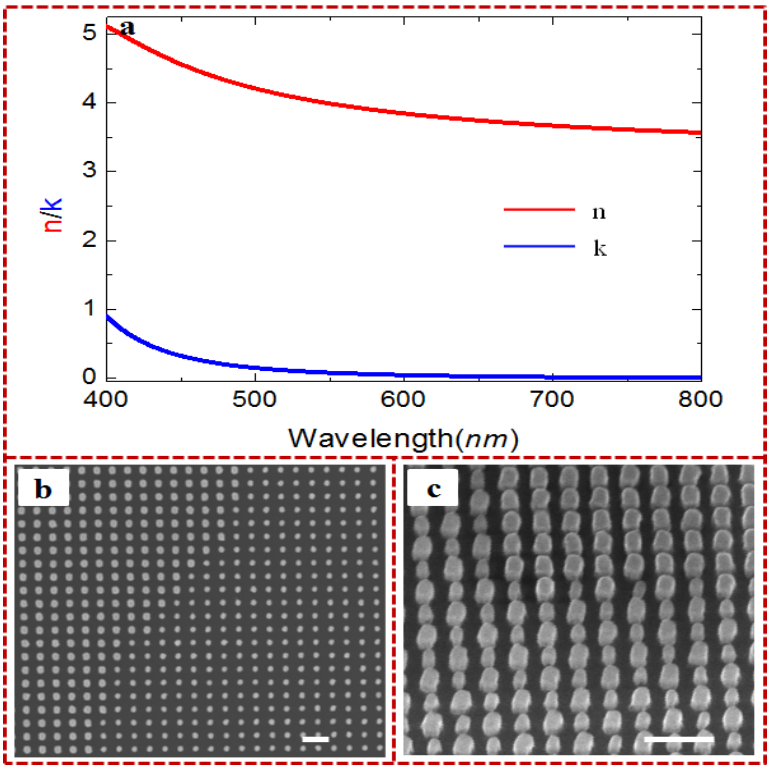


**Figure 2-8. The refractive index of the amorphous silicon film with a thickness of 310 nm and the SEM images of the fabricated samples[6].** (a) Red and blue curves represent the real and imaginary parts of the refractive index, respectively. (b) SEM image of the flower sample. (c) SEM image of the fruit sample with a tilt angle. The scale bar in (b) and (c) is 500 nm.

## 2.6 References


1. Pancharatnam, S. *Generalized theory of interference and its applications*. in *Proceedings of the Indian Academy of Sciences-Section A*. 1956. Springer.

2. Kruk, S. and Y. Kivshar, *Functional meta-optics and nanophotonics governed by Mie resonances.* ACS Photonics, 2017. **4**(11): p. 2638-2649.

3. Berry, M.V., *Quantal phase factors accompanying adiabatic changes.* Proc. R. Soc. Lond. A, 1984. **392**(1802): p. 45-57.

4. Berry, M.V., *The adiabatic phase and Pancharatnam's phase for polarized light.* Journal of Modern Optics, 1987. **34**(11): p. 1401-1407.

5. Huang, L., et al., *Dispersionless phase discontinuities for controlling light propagation.* Nano letters, 2012. **12**(11): p. 5750-5755.

6. Zang, X., et al., *Polarization Encoded Color Image Embedded in a Dielectric Metasurface.* Advanced Materials, 2018. **30**(21): p. 1707499.

7. Arbabi, A. and A. Faraon, *Fundamental limits of ultrathin metasurfaces.* Scientific reports, 2017. **7**: p. 43722.

8. Jiang, S.-C., et al., *Controlling the Polarization State of Light with a Dispersion-Free Metastructure.* Physical Review X, 2014. **4**(2).

9. Grady, N.K., et al., *Terahertz metamaterials for linear polarization conversion and anomalous refraction.* Science, 2013. **340**(6138): p. 1304-1307.

10. Zheng, G.X., et al., *Metasurface holograms reaching 80% efficiency.* Nature Nanotechnology, 2015. **10**(4): p. 308-312.

11. Yue, F., et al., *High-resolution grayscale image hidden in a laser beam.* Light: Science & Applications, 2018. **7**(1): p. 17129.

12. Goldstein, D., *Polarized light*, second edition, revised and expanded. OPTICAL ENGINEERING-NEW YORK-MARCEL DEKKER INCORPORATED, 2003. **83**.

13. Wang, B., et al., *Visible-frequency dielectric metasurfaces for multiwavelength achromatic and highly dispersive holograms.* Nano letters, 2016. **16**(8): p. 5235-5240.

# Chapter 3 Multichannel metasurface devices for phase control

The background of metasurface devices and the relevant physics were covered in the last two chapters. From chapter 3 to chapter 5, we will focus on the metasurface devices with unusual functionalities. When it comes to system integration and device miniaturization, a single optical device which can possess more tunable functionalities is desirable. In this chapter, we will concentrate on two types of multichannel metasurface devices: simultaneous control of holograms and twisted light beams[1], and multichannel polarization-controllable superposition of OAM beams[2].

## 3.1 Generation of Orbital Angular Momentum beams.

As an electromagnetic radiation, a light beam can carry orbital angular momentum (OAM) and spin angular momentum (SAM). Comparing to the common $TEM_{00}$ wave, the wavefront of the light beam with OAM states has a helical phasefront, and an optical vortex in the middle (See Fig.1-8). This helical mode is normally characterized by an integer number named topological charge of m, which can be positive or negative. If $m = 0$, it is a plane wave. If $m \neq 0$, the sign of $m$ determines the handedness of the helical wave front. $m > 0$ means that the wavefront is right-handed twisted, and $m < 0$ means left handedness. The wavefront is then composed of $|m|$ intertwined helices, and each photon carries an orbital angular momentum of $m\hbar$ [3]. One of the common ways to generate such a light beam with OAM state is to use a spiral phase plate, as shown in Fig.3-1. The spiral phase plate introduces the phase shift needed to the $TEM_{00}$ mode of light. The phase shift can be written as $\Delta\varphi = 2\pi(n-1)d/\lambda$, where $\Delta\varphi$ is the phase shift, $n$ is the refractive index of the material used, and $d$ is the thickness of the plate[4].

OAM beams can be generated by using the cylindrical lenses, spiral phase plate, holograms, q-plates and space light modulators [5-7]. However, some of these devices are polarization independent, and others may suffer from the poor spatial resolution, or chemical degradation and sensitive to the environmental temperature, etc. The current method to realize the superposition of various OAM states in quantum experiments is by using the interferometers consisting of an OAM generator, mirrors, beam splitters and other optical components [8-11]. Unfortunately, the involvement of this amount of optical components significantly increases the complexity of the systems, and the errors and misalignment introduced hereby will affect greatly the performance of the experimental setup.

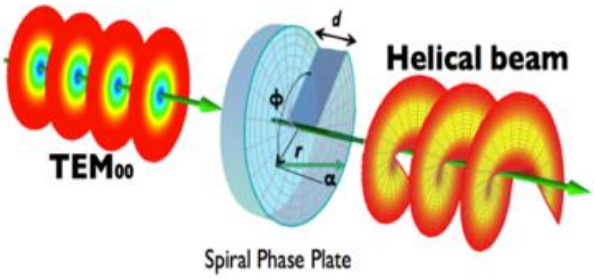


**Figure 3-1 Schematic of the spiral phase plate for OAM generation**[4].

### 3.2 Superposition of OAM states

In recent years the OAM of light has shown very attractive and potential applications in the areas like quantum memories[8], optical tweezers[12], high-capacity optical communication[13, 14] and metrology[15, 16]. The superposition of OAM states is important in the field of classical physics and quantum sciences [9, 10, 17]. Therefore, for practical applications of OAM states, it is very desirable to find a simple and efficient approach to generate OAM beams and to manipulate OAM superpositions at will. For example, a vector beam whose polarization state in the plane transverse to the beam propagation direction is radially distributed, can be realized by the superposition of equal-weight OAM states of $m = 1$ and $m = -1$. This radially polarized vector beam has been widely used[18, 19]. Multiple OAM states can be used to generate arbitrary superpositions of atomic rotational states in a Bose-Einstein condensate[20, 21]. In quantum sciences, OAM entangled light beams are one of the candidates for the fundamental research and characterization of quantum entanglements[22], especially the spin-orbit hybrid entanglement[23-25].

Before we move to the practical part of our approach of realizing the multiple channel superposition of OAM states, the theory modes adopted need to be analysed. As stated in the Chapter 2 of this thesis, the right circularly polarized incident light will be converted to two parts after passing through the nanorods of our design, and they are the non-converted part with the same right circularly polarization, and the converted part with the opposite handedness. These two parts are used in the superposition of the OAM states.

The OAM states of light can be described mathematically as Laguerre-Gaussian (LG) modes which are solutions of the paraxial Helmholtz equation in cylindrical coordinates. The LG mode is characterized by two indices $p$ and $\ell$, which refer to the radial nodes in its amplitude and azimuthal phase dependence, respectively. In this work, we limit to the case of singly-ringed modes with $p = 0$. The field distribution of LG modes with

topological charge of $\ell$ can be expressed as[3, 26]

$$LG^{\ell}(r,\phi,z)=\left(\frac{2}{\pi\,|\,\ell\,|\,!}\right)^{1/2}\frac{1}{w(z)}\left(\frac{r\sqrt{2}}{w(z)}\right)^{|\ell|}e^{-r^2/(w(z))^2}e^{-i\ell\phi}e^{i(kz-kr^2/(2R(z)))}e^{i\varphi(\ell)} \tag{3-1}$$

where $r,\phi,z$ are the cylindrical coordinates, $w(z)=w_0\sqrt{2+z^2/z_R^2}$ is the beam radius at a propagation distance $z$, the constant $w_0$ is the beam waist, $k$ is the wave number, $R(z)=(z_R^2+z^2)/z$ denotes the radius of curvature of the wavefront, $\varphi(\ell)=(|\ell|+1)\tan^{-1}(z/z_R)$ is the $\ell$-dependent Gouy phase[27] at point of z, and $z_R=kw_0^2/2$ is the Raleigh range. The LG mode has a 'doughnut' intensity profile due to the phase singularity in the beam centre. The distance from the centre to points where the intensity is maximum is given by

$$\Omega=\sqrt{\frac{\ell}{2}}w(z) \tag{3-2}$$

The superposition of LG modes with orthogonal circular polarizations produces Poincaré beams which have a spatial mode that correlates transverse spatial coordinates with states of polarization[17, 27]. As we know, any pure state of polarization can be represented with circular polarization bases as

$$|\Psi\rangle=\frac{1}{\sqrt{2}}(\cos\theta e^{i\vartheta}|R\rangle+\sin\theta e^{-i\vartheta}|L\rangle) \tag{3-3}$$

Where $\cos(\theta)$ and $\sin(\theta)$ are the amplitudes of two orthogonal circular components $|R\rangle$ and $|L\rangle$, respectively, $\vartheta$ refers to the phase difference between these two components. Under the illumination of Gaussian beam ($LG^{\ell=0}$) with polarization state described by Eq.3-3 upon the metasurface, the resultant beam is the superposition of two LG modes with orthogonal circular polarizations. Consider the superposition of two LG modes with topological charges $\ell_1$ and $\ell_2$, the resultant beam can be expressed as

$$V = \frac{1}{\sqrt{2}}(\cos\theta \cdot LG^{\ell_1} \cdot e^{i\vartheta} \left| R, \quad \ell_1 \right\rangle + \sin\theta \cdot LG^{\ell_2} \cdot e^{-i\vartheta} \left| L, \quad \ell_2 \right\rangle) \tag{3-4}$$

To clearly analyse the resultant beam, in the context that follows the results are divided into two cases: when $\ell_1 = -\ell_2$ and $\ell_1 \neq -\ell_2$.

1. case $\ell_1 = -\ell_2$

We can rewrite Eq. 3-4 with Jones vector as

$$V = \frac{G^{\ell}}{\sqrt{2}}(\cos\theta e^{i(\ell\phi+\vartheta)} \left| R \right\rangle + \sin\theta e^{-i(\ell\phi+\vartheta)} \left| L \right\rangle) \tag{3-5}$$

Where $\ell = \ell_1 = -\ell_2$ , $G^{\ell} = \left(\frac{2}{\pi \mid \ell \mid !}\right)^{1/2} \frac{1}{w(z)} \left(\frac{r\sqrt{2}}{w(z)}\right)^{|\ell|} e^{-r^2/(w(z))^2} e^{i(kz - kr^2/(2R))} e^{i\varphi(\ell)}$ . When $\theta = \frac{\pi}{4}$, the two circular components have equal intensities. The polarization state at every point of the beam's transverse plane is linear polarization with orientation angle of $\ell\phi + \vartheta$. For $\ell = 1$, the vector beam is the well-studied radial vector beam for $\vartheta = 0$, and the azimuthal vector beam for $\vartheta = \pi/2$. When θ is within the limit of (0, π/4) or (π/4, π/2), the polarization state at every point is elliptical polarization. The ellipticity is determined by θ, and the azimuthal angle is $\ell\phi + \vartheta$. When $\theta = 0$ or $\theta = \pi/2$, the resultant beam is right- or left-handed circularly polarized optical vortex, respectively. The Poincaré beam generated by the superposition of LG modes with orthogonal circular polarizations can be diagnosed by passing it through a linear polarizer with orientation angle $\chi$ (with the horizontal). The transmitted intensity is proportional to $\cos^2(\ell\phi + \vartheta - \chi)$ , and it has $2\ell$ minima at angles[27]

$$\phi_m = \frac{(2a-1)\pi}{2\ell} - \frac{\vartheta}{\ell} + \frac{\chi}{\ell} \tag{3-6}$$

Where $a = 1, 2, \ldots 2\ell$.

2. case $\ell_1 \neq -\ell_2$

The Eq. 3-4 can be rewritten as

$$V = \frac{1}{\sqrt{2}} e^{i(\ell_1+\ell_2)\phi/2} (e^{i\delta} \cos\theta \cos\beta \left|R\right\rangle + e^{-i\delta} \sin\theta \sin\beta \left|L\right\rangle) \tag{3-7}$$

where

$$\beta = \tan^{-1}(\frac{G^{\ell_2}}{G^{\ell_1}}) \tag{3-8}$$

$$\delta = \frac{(\ell_1 - \ell_2)\phi}{2} + \vartheta \tag{3-9}$$

The polarization state at every point is determined by the three parameters $\theta, \beta, \delta$. If $|\ell_1| < |\ell_2|$, the polarization state evolves from right circularly polarized to left circularly polarized when moving the position from centre to the edge of the beam. Interestingly, when $\ell_1 = 0$ and $\ell_2 = 1$, the resultant beam refers to as full Poincaré beam, which has all states of polarization represented on the Poincaré sphere[28], as shown in Fig.3-2.

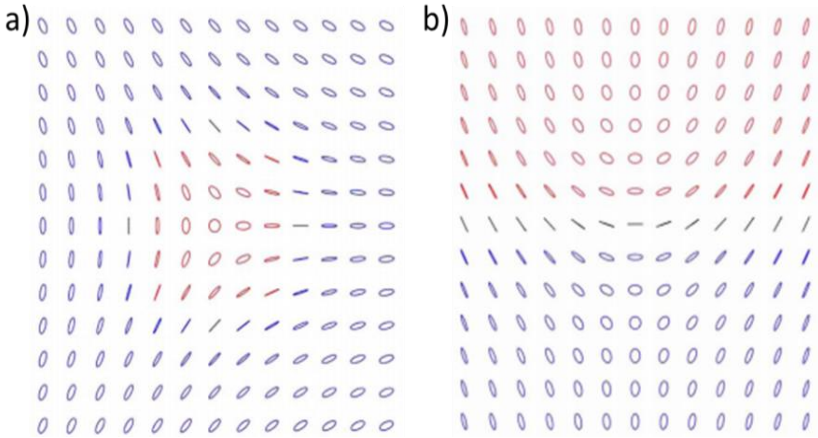


**Figure 3-2 Polarization-state maps of the Poincaré mode obtained by combining the spatial modes with ℓ1 − ℓ2= -1 and (b) ℓ1 − ℓ2=1**. In both cases the spatial modes have p1=p2=0, with the polarization of the component modes linear. Blue, red and black colors represent left-handed, right-handed and linear polarization states, respectively [28].

By passing the resultant beam through a linear polarizer, the output beam becomes composite-vortex beam which contains a vortex of topological charge $\ell_1$ in the centre of

the beam surrounded by $|\ell_1 - \ell_2|$ singly charged peripheral vortices with the same sign of $\ell_2$ located at the same radial distance[28]

$$d = \frac{w(z)}{\sqrt{2}} \left( \frac{\ell_2!}{\ell_1!} (\tan\theta)^2 \right)^{\frac{1}{2(|\ell_2| - |\ell_1|)}} \tag{3-10}$$

Above derivation shows the superposition of LG modes with orthogonal circular polarization states can produce Poincaré beams, which have a spatial mode that correlates transverse spatial coordinates with states of polarization[18]. In Chap.3.4 we will demonstrate the superposition of $\ell = 1$ and $\ell = -1$, while more examples of OAM superpositons will be given in Chap.3.5.

### 3.3 Computer Generated Hologram

Traditionally, a hologram is a three-dimensional image formed by the interference of light beams from a laser or other coherent light source. When properly illuminated by a light beam, this photograph of interference pattern will produce a three-dimensional image, and this process is called reconstruction process of hologram. Hologram is widely used in many areas for various purposes. It is not surprising that the digitalized variation of hologram appeared quite early. Computer-Generated Hologram (CGH) is the holographic interference patterns generated in a digital way. In CGH, a holographic interference pattern can be generated by e.g. digitally computing, then print or by other method onto a film or other materials for the subsequent reconstruction process by a suitable coherent light source. Alternatively, the holographic image can be brought to life by other ways of holographic reconstruction procedure. Similarly, if the holographic data of existing objects is generated optically, but recorded and processed digitally, and brought to display subsequently, it is termed CGH as well. Therefore, the term of CGH is increasingly being used to denote the whole process of synthetically preparing holographic light wave fronts which is suitable for observation[29, 30]. CGHs can be synthesized completely in a digital way, without going through any physical process of a traditional optical holography. Ultimately, computer-generated holography might serve all the roles of current computer-generated imagery: holographic computer displays for a wide range of applications from CAD to gaming, holographic video and TV programs, automotive and communication applications (cell phone displays) and many more.

Polarization-selective CGHs are CHGs which are sensitive to the polarization state of the incident light and can separate the readout light by its polarization so that different holographic images can be reconstructed. Polarization-selective CGHs can be used in multiple level optical switching, image processing[31] and other applications. Traditionally, polarization-selective CGHs are made through etching a birefringent substrate with a surface-relief profile[32] or an isotropic substrate with sub-wavelength structures to generate effective birefringence[33]. Although birefringent crystals can be used to make polarization-dependent optical devices [31, 32, 34], however, the magnitude and form of this birefringence is limited to natural crystals. As an alternative way, materials with sub-wavelength structures can provide enhanced and more controllable birefringence. However, the extreme anisotropy involved requires high aspect ratio features which leads to the complexity in the fabrication process. Additionally, the variation in height levels causes shadowing effects which will limit the projection angle of the hologram[35]. Moreover, most of the current polarization-selective CGHs suffer from narrow operating bandwidth which means the phase function and the diffraction efficiency change significantly if the incident wavelength drifts from the designed value. In the next part and Chap.4, we experimentally demonstrate how a metasurface can be used to generate the CGHs, and how the metasurface based holograms can be integrated with other functionalities.

## 3.4 Multichannel metasurface for simultaneous control of holograms and twisted light beams

In this part of the thesis we designed one metasurface which can control phase of light in four different channels, two of which are polarization-sensitive hologram in horizontal direction and two are polarization-controllable OAM superposition in vertical directions. The approach provides a new possibility to realize a multi-channel device with tunable multiple functionalities. Although this type of metasurface devices are still in their infancy, they provide in the long run opportunities to integrate multiple channels and multiple tuneable functions to a single ultrathin flat nanoscale device.

### 3.4.1 Design

Figure 3-3a is the schematic illustration of experimental setup and expected results based on the designed metasurface device that can simultaneously control the holographic images and the OAM superposition. In this approach, the arbitrary control of the

polarization sensitive holograms and the superposition of light beams with different topological charges is realized in vertical and horizontal directions, in four-channel manner.

In order to generate arbitrary polarization state of the incident light, a polarizer and a quarter wave plate are used. Two separate holographic images and two OAM light beams with a topological charge of $\ell = 1$ (or -1) (see Fig. 3-3a) are predicted when the designed metasurface device is illuminated with an input light beam with pure circular polarization, i.e., right circular polarization (RCP) or left circular polarization (LCP). When the helicity of the incident light is changed to its opposite, both the holographic image and the superposition patterns of the vertex beams will be changed. In the horizontal direction, the holographic image will be changed to its centrosymmetric counterpart, and in the vertical direction the topological charge of the OAM pattern will be changed to $-\ell$. Thus when the pure linearly polarized light shines on the sample, one can predict that both in the horizontal direction and vertical direction, the overlap of the above two situations will occur, as shown in Fig.3-3b.

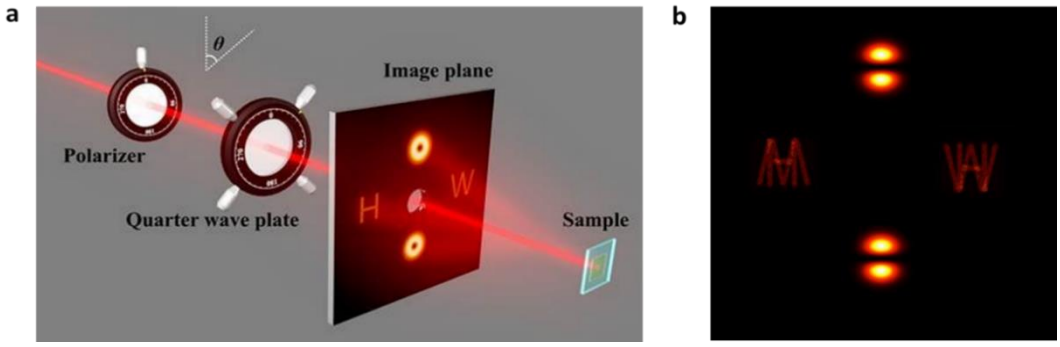


**Figure 3-3 Schematic illustration of simultaneous control of hologram and superposition of orbital angular momentum (OAM)[1].** (a) Under the illumination of LCP light, the holographic images 'H' and 'W' (Heriot-Watt University) are reconstructed on the left and right side along the horizontal direction, respectively. Two pure OAM beams with the same topological charges $\ell = 1$ are generated along the vertical direction. (b) The simulation results for the case when the polarization state of the incident light is linear polarization.

Please be advised that the intensities of two overlapping holographic images are the same. In the same way, two superpositions of OAM states with $\ell = 1$ and $\ell = -1$ in the vertical direction with equal components will generate a radially polarized vector beam which can be verified by an analyser in the light path. In Fig.3-3b, a polarizer with a transmission axis along the vertical direction is applied when the simulation is carried out. However, the two holographic images will overlap, and OAM superposition will

occur upon the illumination of a light beam with elliptical polarization since it can be decomposed into a LCP light beam and a RCP light beam with different weight.

To realize the above proposed tunable multi-channel optical device with different functionalities, first, as detailed in Fig.3-4a where *d* is the distance between neighboring nanorods with a value of 424 nm along both *x* and *y* directions here, two metasurfaces with different functionalities, e.g., one for two holographic images along the horizontal direction(green nanaorods) and another for two OAM beams along vertical direction(pink nanorods), are designed to operate with opposite incident helicities. Secondly, these two metasurfaces are merged together with a displacement vector of (*d*/2, *d*/2). In order to do so, one need to generate two different types of phase profile to realize these two functionalities respectively and the size of each pixel of the sample is the same before and after merging. In this design, the equivalent pixel size in the merged metasurface is 300 nm×300 nm.

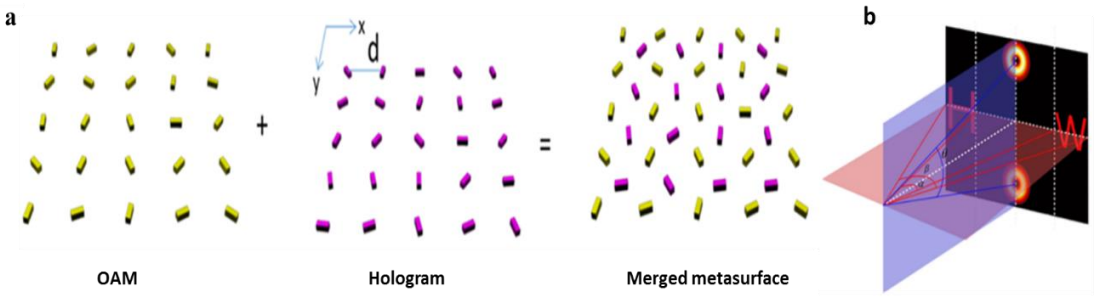


**Figure 3-4 Design schematic of the multi-channel metasurface device with tunable functionalities[1].** **(a)** One metasurface for two holographic images along the horizontal direction and the other for two OAM beams along vertical direction are merged together with a displacement vector of (d/2, d/2) where d is the distance between neighboring antennas with a value of 424 nm. The size of the sample is still the same and the equivalent pixel size is 300 nm× 300 nm. (b) Geometric parameters of the projected holographic images and OAM beams that correspond to the merged hologram. The full off-axis angle α, β and $\theta$ are designed to be 22.2°, 32.5° and 17.4°, respectively.

In order to mathematically describe the designed phase distribution generated by the metasurface, the coordinate system in Fig.3-4 can be rotated counter clockwise through an angle 45°. The new coordinates of the point (x, y) are described as

$$\begin{bmatrix} x' \\ y' \end{bmatrix} = \frac{\sqrt{2}}{2}\begin{bmatrix} 1 & -1 \\ 1 & 1 \end{bmatrix}\begin{bmatrix} x \\ y \end{bmatrix} \tag{3-11}$$

where (x′, y′) are the coordinates of the point after rotation. The general phase distribution for the transmission function of the device can be written as follows,

$$\emptyset(x', y') = 0.5[1 + (-1)^{m+n}]\emptyset_{OAM}(x', y') + 0.5[1 - (-1)^{m+n}]\emptyset_{HOLO}(x', y') \quad (3\text{-}12)$$

where (x′, y′) is the location of the nanorods in the new coordinate system, $m = \sqrt{2}x'/d$, $n = \sqrt{2}y'/d$, d = 424 nm. $\Phi_{OAM}$(x′,y′) and $\Phi_{HOLO}$(x′,y′) are the generated phase profiles for the off-axis OAM states and the hologram, respectively.

Regarding the geometric parameters of the projected holographic images, as shown in Fig.3-4b, the following equations are adopted to do the design and calculations.

$$d_x = m\lambda/(2\tan(\alpha_x/2)) \quad (3\text{-}13)$$

$$d_y = n\lambda/(2\tan(\alpha_y/2)) \quad (3\text{-}14)$$

Where the period of the hologram in two orthogonal directions of $x$ and $y$ are $d_x$ and $d_y$ , and $m \times n$ is the pixel array of the target hologram image at the projection angle of $\alpha_x \times \alpha_y$ in the far field, and λ is the wavelength used in the design. Thus, the number of the pixels of the hologram can be determined by

$$M = d_x/\Delta p \quad (3\text{-}15)$$

$$N = d_y/\Delta p \quad (3\text{-}16)$$

Where $\Delta p$ is the pixel size of the hologram in both x and y directions. According to the theoretical models and equations given above, the phase-only hologram in horizontal direction with the pixel size of 300 nm×300 nm is designed based on the classical Gerchberg−Saxton algorithm. In the vertical direction, two OAMs are designed with the topological charge of $\ell = 1$ and $\ell = -1$.

The reflective geometric metasurface is used in the design. The structure of designed metasurface has three layers with gold nanorod array on the top (30 nm), a gold background layer (150 nm) sitting on the silicon substrate and a SiO2 spacer layer of 85 nm sandwiched between the top and bottom metallic layers(shown in Fig.3-5a).

The designed sample is based on the Pancharatnam-Berry (PB) phase which is a geometrical phase associated with the polarization of light. When the polarization state of a light beam traverses a closed loop on the Poincaré sphere, the final state differs from the initial state by a phase factor equal to half the area encompassed by the loop on the

sphere. Thus upon the illumination of a RCP light beam, the emitted light from the metasurface with the same circular polarization picks up an abrupt phase change of $2\varphi(x,y)$ (PB phase)[2, 36] where $\varphi(x,y)$ is the spatial distribution of orientation angle of the nanorods in the designed sample. When the polarization state of incident

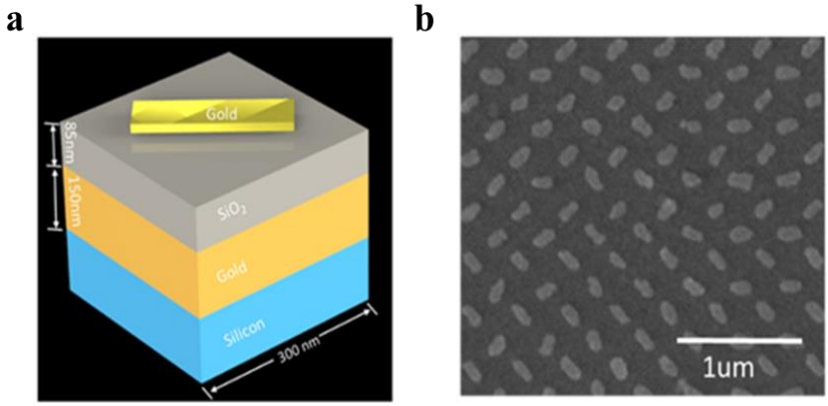


**Figure 3-5 Designed metasurface device[1].** (a) Schematic illustration of a single unit of the reflective-type metasurface. The finished sample consists of gold nanorods with spatially varying orientations on the top, a $SiO_2$ spacer layer (80 nm) and a gold background layer (150 nm) resting on a silicon substrate. (b) SEM image of the fabricated metasurface sample. The scale bar is 1 μm. The equivalent pixel size is 300×300 $nm^2$, and the size of fabricated metasurface is 300×300 $um^2$.

light is changed from RCP to LCP, the abrupt phase change is flipped to$-2\varphi(x,y)$. Therefore in this way, the metasuface that is designed based on the geometric metasurfaces can be an efficient way to modify not only the phase profile of light in a space-variant manner at subwavelength resolution, but also the polarization profile of the light[1].

In order to reconstruct two symmetrically distributed off-axis holographic images along the horizontal direction, Gerchberg−Saxton algorithm is adopted here to generate the required phase profile. Both images ('H' and 'W') have a projection angle of ($8.71^\circ \times 12.02^\circ$) and an off-axis angle of $11.10^\circ$ in the imaging area (see Fig.3-4b). To realize OAM superposition along the vertical direction, the phase distribution of off-axis OAM states is described as[1, 2]

$$\Phi(x,y) = \arg\left(\sum_{j=1}^{2} E_j \exp(i(\ell_j \theta + \Delta\varphi_{j,y}))\right) \tag{3-17}$$

Where $j=1,2$ means totally there are two OAM states, $E_j$ is the amplitude component of OAM state $\ell_j$, $\theta$ is the azimuthal angle and $\Delta\varphi_{j,y}$ is the phase difference between

neighboring pixels to generate a phase gradient along the *y* direction, which results in the off-axis deflection for the OAM mode of interest. It is worth mentioning that the off-axis deflection here is only introduced in the vertical direction (the *y* direction) as there are holographic images in the horizontal direction. A $\pi/5$ phase difference between neighboring pixels is introduced here in order to generate the off-axis phase gradient along the vertical direction. The off-axis angle of two OAM patterns is $8.7^{\circ}$ ($\theta$ in Fig.3-4b). The topological charges for the two OAM beams have the same value of $\ell = 1$ upon the illumination of RCP light.

### 3.4.2 Results

To experimentally verify our design, we fabricate the reflective-type metasurface (Fig.3-5b) using the standard electron-beam lithography, metal deposition and lift-off process. Firstly, a silicon substrate is deposited by a gold background layer (150 nm), then a $SiO_2$ spacer (85 nm) using an electron beam evaporator is deposited. The nanostructures are defined on the poly methyl methacrylate (PMMA) film by EBL (Raith PIONEER). Prior to gold film (30 nm) deposition, a titanium layer of around 3 nm is deposited on the silicon dioxide ($SiO_2$) layer for adhesion purpose. Finally, the metasurfaces' structure is achieved by a subsequent lift-off procedure.

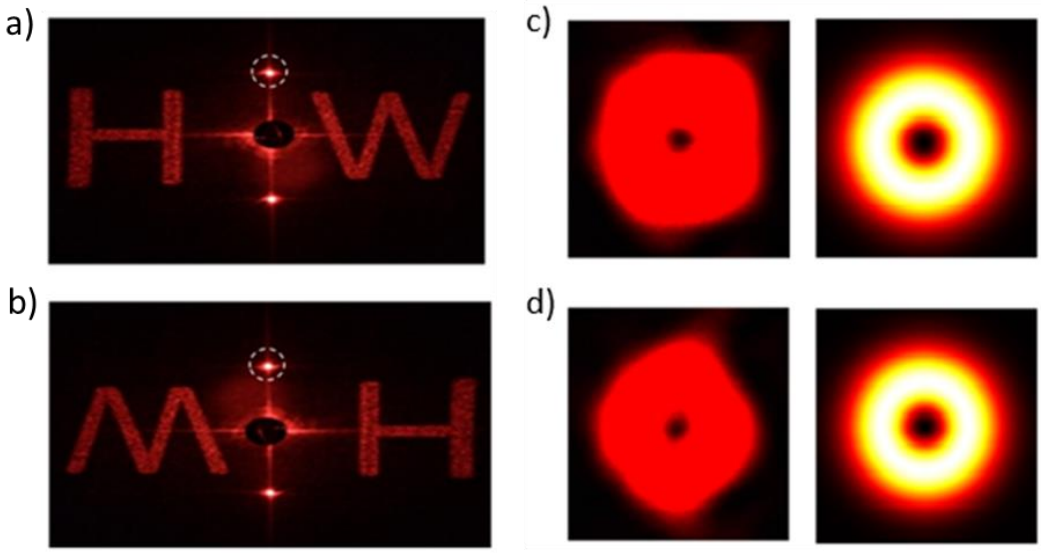


**Figure 3-6 Dependence of experimental results on the helicity of the incident light[1].** The experimentally obtained images for the incident light with (a) LCP and (b) RCP. The incident light impinges normally onto the metasurface and the reconstructed images are projected onto the image plane. The screen is a white paper board with an opening (diameter 6 mm) in the middle, which allows the incident light and zero order reflected light passing through. The wavelength of the incident light is 640 nm. The dashed circles mark the generated OAM beam. Simulated and measured intensity profiles of the OAM beam for

c)LCP and d) RCP incidence after the light beam passes through the polarizer with the transmission axis along the vertical direction.

The experimental setup to characterize the fabricated metasurface device is shown in Fig.3-3a. The sample is mounted on a 3D translational stage, allowing for fine adjustment of sample position. The incident light at the wavelength of 640 nm is from a tunable supercontinuum laser source (NKT-SuperK EXTREME). The experimental setup consists of a polarizer, a quarter-wave plate, a white paper board with an opening (diameter 6 mm). When the LCP light shines on the sample, two separate holographic images of 'H' pattern on the left and the 'W' pattern on the right of the opening in the center of the paper screen, along the horizontal direction, are cleared observed when viewed from where the sample is. In the vertical direction, two 'donut'-shaped OAM patterns are symmetrically located, as shown in left column of Fig.3-6a. Since our design is based on the PB phase which means the sign of the phase profile will be changed when the helicity of the incident light is flipped. That is the 'H' and 'W' pattern will be swapped in horizontal direction and flipped in vertical direction when the helicity of the incident light is changed from LCP to RCP (shown in left column of Fig.3-6b). Meanwhile in the vertical direction, the propagating directions of two generated OAM beams are swapped as well with respect to the surface normal of the metasurface, and the signs of two topological charges are flipped to $\ell = -1$. However, during the experiment no swap of OAM patterns can be observed on the paper screen since these two OAM states along the vertical direction are exactly the same, as shown in the right column of Fig.3-6.

In order to further characterize the purity of the OAM beams, the simulated and experimentally measured results of the transmitted intensity profile are given as well (right columns in Fig.3-6). Please be advised that one cannot spot clear difference before and after the beam passing through the polarizer if it is located after the metasurface device along the light path. This indicates that the OAM beams generated by our sample are with high purity.

As indicated by Eq.3-3, an arbitrary polarized light beam can be considered as the superposition of two circularly polarized beams with opposite helicity, therefore one can predict the result of superposition of hologram images and OAM patterns if the polarization states of incident light is known, for example to linearly polarized light or elliptically polarized light. For five commonly used polarization states such as RCP, right-handed elliptical polarization (REP), linear polarization (LP), left-handed elliptical

polarization (LEP) and LCP, the simulated and experimental measured results are given in Fig.3-7. Under the illumination of pure LCP light at the wavelength of 640nm, two reconstructed clear images of ‘H’ and ‘W’ lie on the left and right sides of the image plane, respectively. When the RCP light impinges on the sample, both holographic images change to its centrosymmetric counterpart, e.g. flipped ‘W’ and ‘H’. Here please note that ‘H’ and flipped ‘H’ are the same, so the flip of ‘H’ cannot be observed in the experiment.

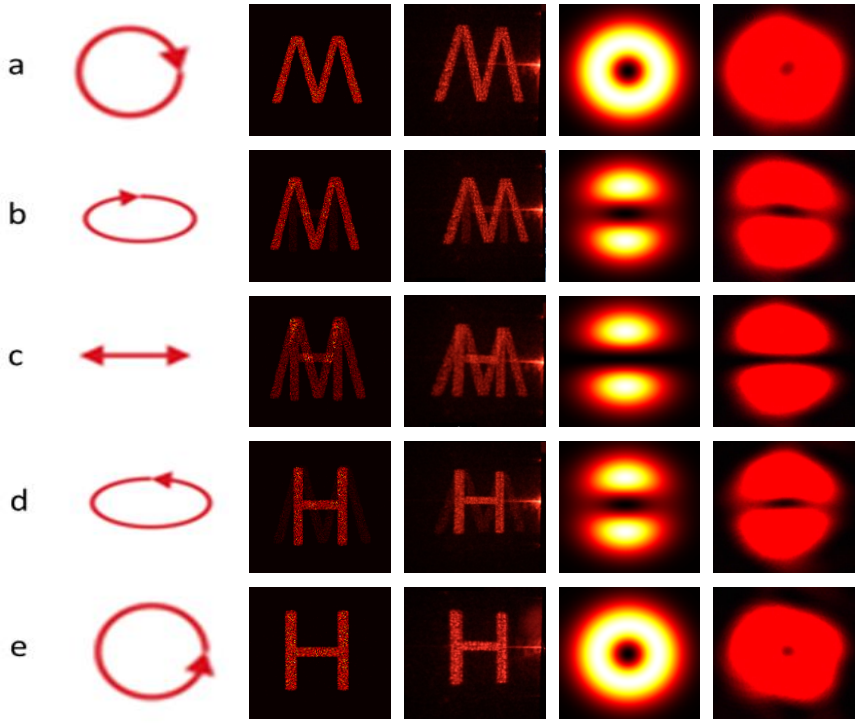


**Figure 3-7 Measured results and simulation results versus polarization states of the incident light at 640 nm[1].** The polarization states of the incident light are chosen to be (a) RCP, (b) right-handed elliptically polarized, (c) linearly polarized, (d) left-handed elliptically polarized and (e) LCP. The second and third columns represent the simulated and experimental results of holographic images in one channel. The fourth and fifth columns show the simulated and measured results for the generated intensity profiles for corresponding polarization states after the resultant OAM beam passes through the linear polarizer whose transmission axis is along the vertical direction.

However, when the elliptically or linearly polarized light impinges on the metasurface sample, the two images (mentioned above) overlap. When REP light is used, the left pattern with higher intensity of flipped ‘W’ and lower intensity of ‘H’, while the right pattern has higher intensity pattern of ‘H’ and lower intensity pattern of ‘W’, and vice versa for the LCP light. The intensities of two overlapping images rise and fall according to the change of ellipticity of various incident polarized light, which is realized by changing the angle between the polarization axis of the polarizer and the fast axis of the

quarter wave plate during the measurement. When the polarization state changes to the linear polarization, the images are overlapped with the same intensity of flipped 'W' and 'H' (or 'H' and 'W'). During the measurement the distance between the screen and the metasurface sample is kept at about 15 mm.

To characterize the functionality of polarization-controlled OAM superposition, the simulated and measured intensity profiles of the OAM superposition are given in the fourth and fifth columns of Fig.3-7 for the corresponding polarization states of the incident light. By continuously changing the polarization state of the light, the evolution process of the intensity distribution can be observed after the resultant OAM beam passes through the rotating polarizer (before the sample). When the linearly polarized (LP) light is incident onto the metasurface, the resultant output beams are the superposition of $|R, \ell = 1\rangle$ and $|L, \ell = -1\rangle$ with equal power, which is a radially polarized vector beam that has been found in many applications due to its unique properties[37]. It is worth mentioning that there is a clear gap between the two petals for linear polarization of the incident light. All the simulation results in Fig.3-7 are carried out in Matlab. First step, Gerchberg-Saxon method is used to reconstruct the phase profile of the hologram in horizontal direction. Then, a phase profile which are the same as the OAM modes with topological charges needed and a phase gradient in vertical direction are introduced in the vertical direction during the Matlab coding process. When the above two steps are done, these two phase profiles are merged together by following the method suggested by Eq.3-12 so that the final phase that we need can be generated.

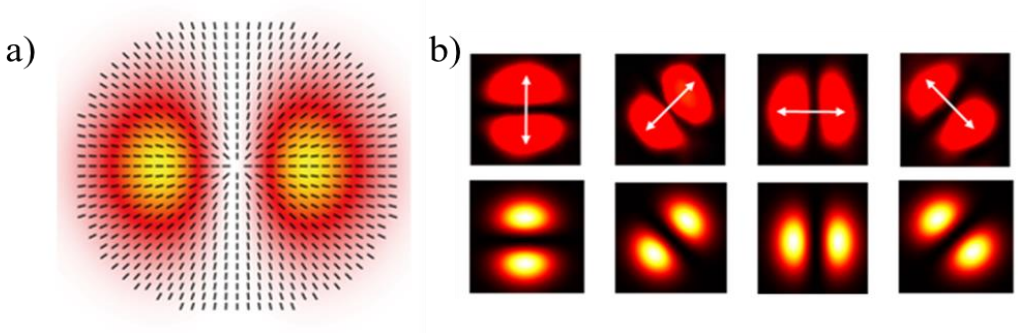


**Figure 3-8 Polarization profile of a radially polarized vector beam and intensity profile of the resultant beam for the incident light with linear polarization.** (a) Polarization distribution of the radially polarized vector beam. (b) Under the illumination of linearly polarized light beam, the resultant beam from the superposition of two OAM beams with topological charges $\ell = 1$ and $\ell = -1$ in the vertical channel is a radially polarized vector beam. To characterize these beams, two petals in the intensity profile are predicted and observed after the light beam passes through the polarizer. The two petals are rotated when

the transmission axis of the polarizer is changed. The white double-headed arrows show the direction of the analysing polarizer's axis[1].

One of the advantages designing our metasurface device based on PB phase is that the designed device works broadbandly which means if the wavelength of incident light is changed, the system designed here still works. The sample is mainly characterized at the wavelength of 640 nm. When the wavelength of incident light is 530nm and 600nm, the experimentally captured results is given in Fig.3-9 to Fig.3-12. All these results agree well with the simulation.

### 3.4.3 Discussion

The efficiency of this device is defined as the ratio between the power sum of the output light from the four channels and the power of incident light. The measured efficiency at designed working wavelength of 640 nm is around 9%, which agrees well with the value in the Reference 2. In the future work, there are two options which can be adopted to increase the efficiency of the design. First, replacing the gold in the design with silver which has higher efficiency in the spectrum of visible to infrared range. Secondly, the dielectric metrsurface consisting of TiO2 nanofins can be used in the design to improve the efficiency[38].

The combination of two different phase profiles brings in a crosstalk between them after merging, and the performance of the designed metasurface device can be improved by design optimization [17].

For other wavelengths, we experimentally observed the performance of the designed metasurface under the green light of 530nm and amber light at 600nm. Some of the results are presented in Fig.3-9 to Fig.3-12.

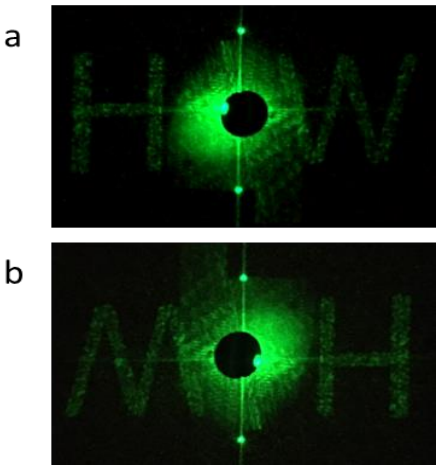

**Figure 3-9 Experimental results of hologram and OAM superposition at wavelength of 530nm**. a) LCP incidence b) RCP incidence

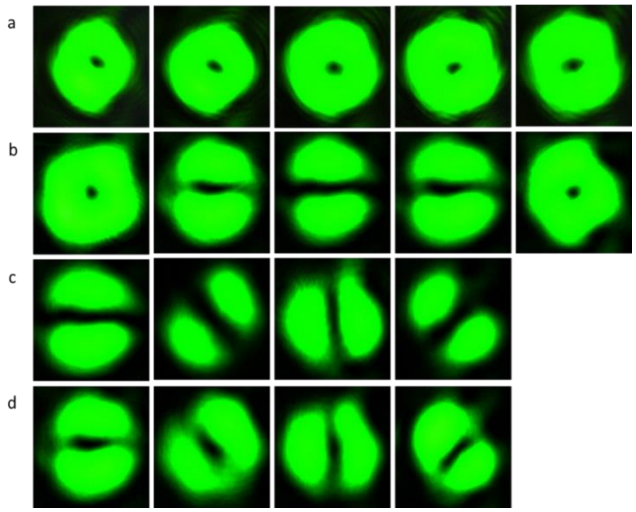


**Figure 3-10 The experimental measured results of OAM superpositions**, a) five different polarization incidence (RCP, REP, LP, LEP, LCP)and without the analyzing polarizer after the sample, b) five different polarization incidence and with the analyzing polarizer at vertical position after the sample, c)when the incidence light is LP light, analyzing polarizer at at 0, pi/4, pi/2, 3pi/4, respectively, d) when the incidence light is EP light, analyzing polarizer at at 0, pi/4, pi/2, 3pi/4, respectively

The design adopted here is a combination of multiple functionalities and multiple channels, which significantly decreases the size of the optical component, and therefore increase the density of functionality. This single metasurface experimentally realizes the polarization-controlled OAM superposition and hologram. If adding other advantages, such as subwavelength resolution, broadband and compactness, it may have a broad impact in the areas of photonics, quantum sciences, and fundamental physics. Without the metasurface device designed here, in order to realize the same functionalities, one must rely on a complicated experimental setup which normally includes the optical devices such as beam-splitters, prisms, mirrors etc. The linear combination of equal-weighted RCP optical vortex beam with topological charge $\ell = 1$ and LCP optical vortex beam with topological charge $\ell = -1$ can generate a radial vector beam (see Fig.3-8a), which has been applied in metrology [20], lithography[14], and quantum memory [21]. The intensity profile of two petals will be rotated if the transmission axis of the polarizer is rotated, as shown in Fig. Fig.3-8b.

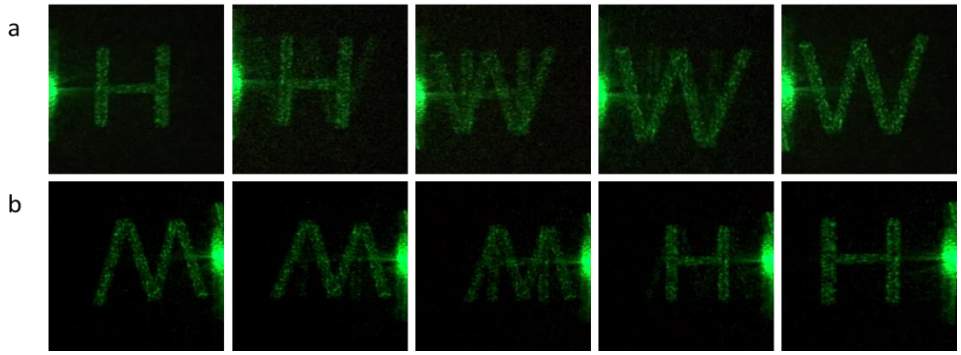


**Figure 3-11 Holographic imges measured in the experiment when the wavelength of incident light is 530nm.** Five different polarization states (LCP, LEP, LP, REP, RCP) of incident light is used, from left column to right.

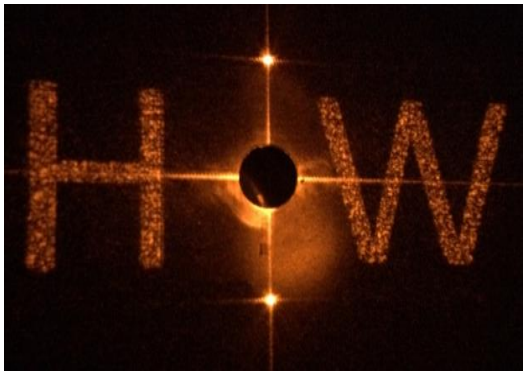

**Figure 3-12 Experimental results of hologram and OAM superposition together when the wavelength of incident light is 600nm.** a) LCP incidence b) RCP incidence.

To summarize this piece of work, a single metasurface device is presented which can realize polarization-dependent hologram and continuously control the superposition of OAM in multiple channels. By controlling the polarization state of incident light, different superpositions of OAM states and holographic images are realized. Good agreement between the simulated and experimental measured results is found. The developed device provides a new tool to modify the polarization and phase simultaneously.

### 3.5 Multichannel Metasurfaces for controllable OAM superpositions

Following the demonstration in Chap.3.4, we further verify the capability of metasurface for controlling the phase of light in multiple channel manner by choosing vortex beams with different topological charges as the candidate. Fig.3-13 is the schematic illustration of the design for the purpose of OAM superpositon. Please note this work has been published. In the context below, only the parts that I contributed is covered. For more detailed results, please refer to Ref [2].

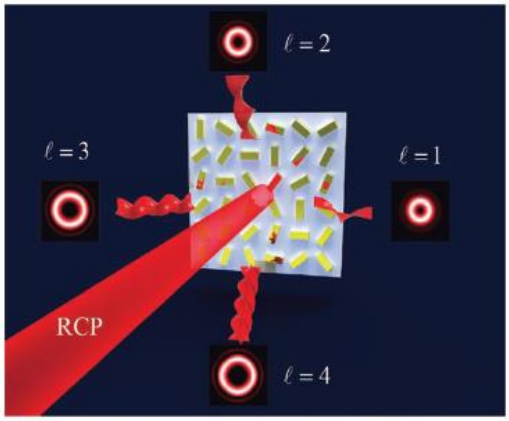


**Figure 3-13 Schematic illustration of off-axis multichannel OAM generation[2].** Four OAM states with different topological charges ranging from ℓ = 1 to ℓ = 4 are generated under the illumination of RCP light. The positions of all four OAM beams are steered to their centrosymmetric positions when the handedness of the incident light is changed LCP. Meanwhile, the signs of these four topological charges is changed from plus to minus.

As shown in Fig.3-13, when a RCP Gaussian beam shines on the designed metasurface device four OAM beams with topological charges ranging from ℓ = 1 to ℓ = 4 are generated in two orthogonal directions. When the handedness of the incident light is changed LCP, the positions of all OAM beams will be changed to their centrosymmetric positions with respect to the axis of incident light. Meanwhile, the signs of all four topological charges are changed from plus to minus, as given in detail in the Fig.3-14 (i) to (ii).

Under the illumination of RCP Gaussian beam ($|R\rangle$), two off-axis centrosymmetric OAM beams $|R,\ \ell_1\rangle$ and $|R,\ \ell_2\rangle$ along two propagating directions (see Fig.3-14(i)) are generated simultaneously. The deflection angle $\alpha$ is determined by the phase differences $\Delta\varphi_{i,x}$ and $\Delta\varphi_{i,y}$. By switching the handedness of incident CP light from right handedness to left handedness, the propagating directions of two resultant OAM beams are swapped with respect to the axis of incident light. Meanwhile, the signs of two topological charges are flipped, as shown in Fig.3-14(ii)). Since an arbitrary polarized light beam can be decomposed into the superposition of two circularly polarized beams with opposite helicity (see Fig. 3-14 (iii)), which can be described as[2]

$$|\Psi| = A\cdot|R\rangle + B\cdot|L\rangle e^{i\vartheta} \tag{3-18}$$

where $A$ and $B$ are the amplitude coefficients of RCP and LCP light, $\vartheta$ is the relative phase difference between two different polarization states. Thus, the resultant beam is a superposition of two OAM beams $|R,\ \ell_1\rangle$ and $|L,\ \ell_2\rangle$ (see Fig. 3-13 (iii) and (iv)), and it would be $(|R,\ \ell_1\rangle + B|L,\ \ell_2\rangle e^{i\vartheta})$. It is clear that the superposition of two eigenstates is exactly dependent on the polarization state of incident light. Consequently, multi-channel, arbitrary superposition of two or more OAM beams can be realized by using a single reflective-type metasurface with the predesigned phase distribution.

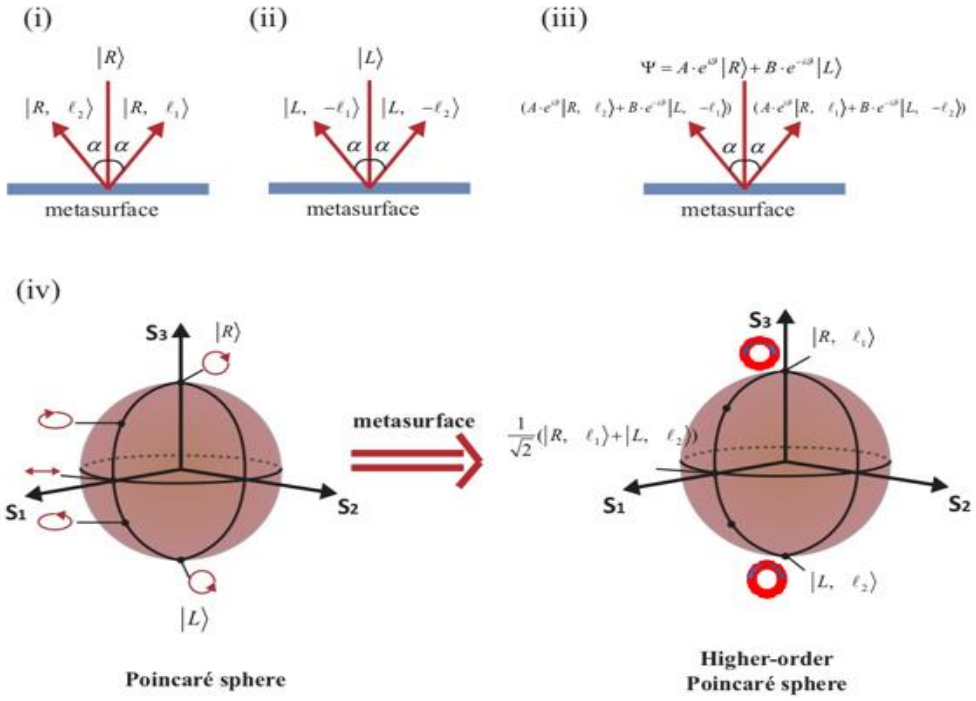


**Figure 3-14 Schematics illustration of polarization-controllable superpositions of OAM states[2].** The polarization states of the incident light in (i), (ii), and (iii) are RCP, LCP, and arbitrary polarization state, respectively. For case (iii), the resultant beam is the superposition of RCP and LCP OAM beams with different components (A for RCP and B for LCP) and a phase difference $e^{i\vartheta}$. iv) Illustration of the superposition process with the aid of two types of Poincare spheres. The polarization state of the incident light is represented by a point on the fundamental Poincare sphere, while the superposition of OAM eigenstates ℓ1 and ℓ2 is represented by a higher order Poincare sphere. Here the metasurface bridges the gap between the two different types of Poincare spheres.

For the purpose to investigate different superpositions, three samples (Sample1, Sample2 and Sample3) were made. Sample1 was designed to superpose the OAM beam with odd number. Fig.3-15 shows the SEM image of sample META1, and the experimental results of superposition of OAM states with odd number topological charges of same absolute values but opposite signs in four output channels. Similarly, sample Sample2 was

designed to superpose the OAM beam with even number. A good agreement of therotical and experimental results are found for this sample, as shown in Fi.3-16.

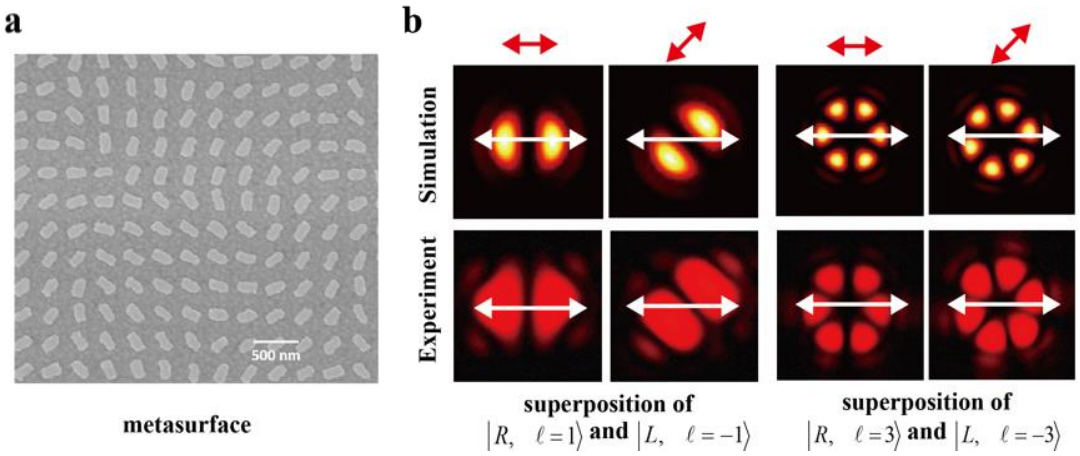


**Figure 3-15 SEM image, theoretical simulation and experimentally obtained superpositions of OAM states[2].** This metasurface produces two superpositions, OAM states with $\ell=1$ and $\ell=-1$, and OAM states with $\ell=3$ and $\ell=-3$. **a).** Part of the SEM image of the fabricated metasurface. **b).** The simulation and experimental results. The polarization angle of incident LP light and the direction of the analysing polarizer's transmission axis (in front of the CCD camera) are represented by the double-headed red and white arrows.

To further explain the mechanism of OAM superposition, the recent concept of Higher-order Poincaré sphere is introduced[23][2] here which extend the traditional Poincaré sphere to the totally angular momentums which includes spin and orbital angular momentum. On the Higher-order Poincaré sphere, two poles represent two eigenstates with different spin and orbital angular momentum $|R, \ell_1\rangle$ and $|L, \ell_2\rangle$, corresponding to two Laguerre-Gauss (LG) transverse modes with opposite circular polarization states, respectively. It is worth mentioning both the signs and values of OAM eigenstates $\ell_1$ and $\ell_2$ can be different [25]. The superposition of two LG modes with orthogonal circular polarization states can produce Poincaré beams, which have a spatial mode that correlates transverse spatial coordinates with states of polarization [25]. The detailed theoretical information is provided in Chapter3.2. Fig.3-14(iv) shows how a metasurface device can be a link bridge between the easily manipulated polarization states represented on the Poincaré sphere and the higher-order states (spin and angular momentum) on the Higher-order Poincaré sphere with circular polarized OAM eigenstates $\ell_1$ and $\ell_2$, through a metasurface. By controlling the polarization state of the incident light, the generation of required OAM eigenstates and their superposition process can be realized on the same metasurface.

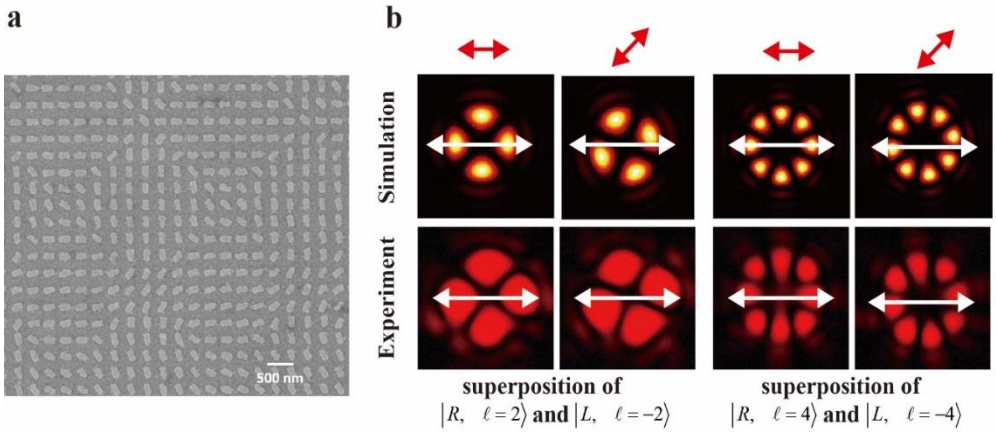


**Figure 3-16 SEM image and numerically calculated and experimentally observed superpositions of OAM states[2].** Sample2 produces two superpositions which are superposition of OAM states with topological of $\ell = 2$ and $\ell = -2$, and superposition of OAM states with $\ell = 4$ and $\ell = -4$. **a.** SEM image of the fabricated metasurface Sample2. **b.** Simulation and experimental results for Sample2. The polarization angle of incident LP light and the direction of the analysing polarizer's transmission axis (in front of the CCD camera) are represented by the double-headed red and white arrows.

To demonstrate the versatility and high performance of the design approach, a third (Sample3) sample was further developed, which can realize hybrid superpositions of OAM states with different absolute value of topological charges in four separate channels (Fig.3-18a(ii)). OAM beams with topological charges ranging from ℓ = 1 to ℓ = 4 in separate channels are observed for an incident Gaussian beam with right-handed circular polarization. The intensity distribution of an OAM beam with topological charge of ℓ is doughnut shaped with a dark area in the centre. The radius of the "doughnut," defined by the distance from the centre to the maximum intensity points, is expressed by $r = \tau\sqrt{\ell/2}$, where τ is the beam radius [27]. By controlling the polarization of incident beam, four cases of superpositions of OAM states in four separate output channels are realized, which are $cos\theta \cdot e^{i\vartheta}|R, \ell = 1\rangle + sin\theta \cdot e^{-i\vartheta}|L, \ell = -3\rangle$ , $cos\theta \cdot e^{i\vartheta}|R, \ell = 2\rangle + sin\theta \cdot e^{-i\vartheta}|L, \ell = -4\rangle$, $cos\theta \cdot e^{i\vartheta}|R, \ell = 3\rangle + sin\theta \cdot e^{-i\vartheta}|L, \ell = -1\rangle$ and $cos\theta \cdot e^{i\vartheta}|R, \ell = 4\rangle + sin\theta \cdot e^{-i\vartheta}|L, \ell = -2\rangle$, where $\theta$ denotes the ratio of the amplitudes of two component OAM beams. Each OAM superposition can be represented by a point on a hybrid-order Poincaré sphere [25]. A similar method as above is used to characterize this metasurface device. Although there are four different superpositions, the simulation and experimental results of the OAM superposition $cos\theta \cdot e^{i\vartheta}|R, \ell = 1\rangle + sin\theta \cdot e^{-i\vartheta}|L, \ell = -3\rangle$ is given in Figure 3-18b. By continuously changing the polarization state of incident light, one can notice that from RCP to LCP, the diameter of dark hole in the centre of the generated intensity profile increases, indicating the superposition of two OAM states

evolves from the OAM state with $\ell 1 = 1$ to that with $\ell 3 = -3$. For elliptically polarized incidence, the resultant beam is the superposition of two OAM states with different components, which is further verified by the transmitted intensity profiles through a horizontal linear polarizer. Actually, the output beam becomes a composite-vortex beam, which contains a vortex of charge $\ell 1 = 1$ in the centre of the beam surrounded by $|\ell 1 - \ell 3| = 4$ singly charged peripheral vortices with the same sign of $\ell 3$ located at the same radial distance.

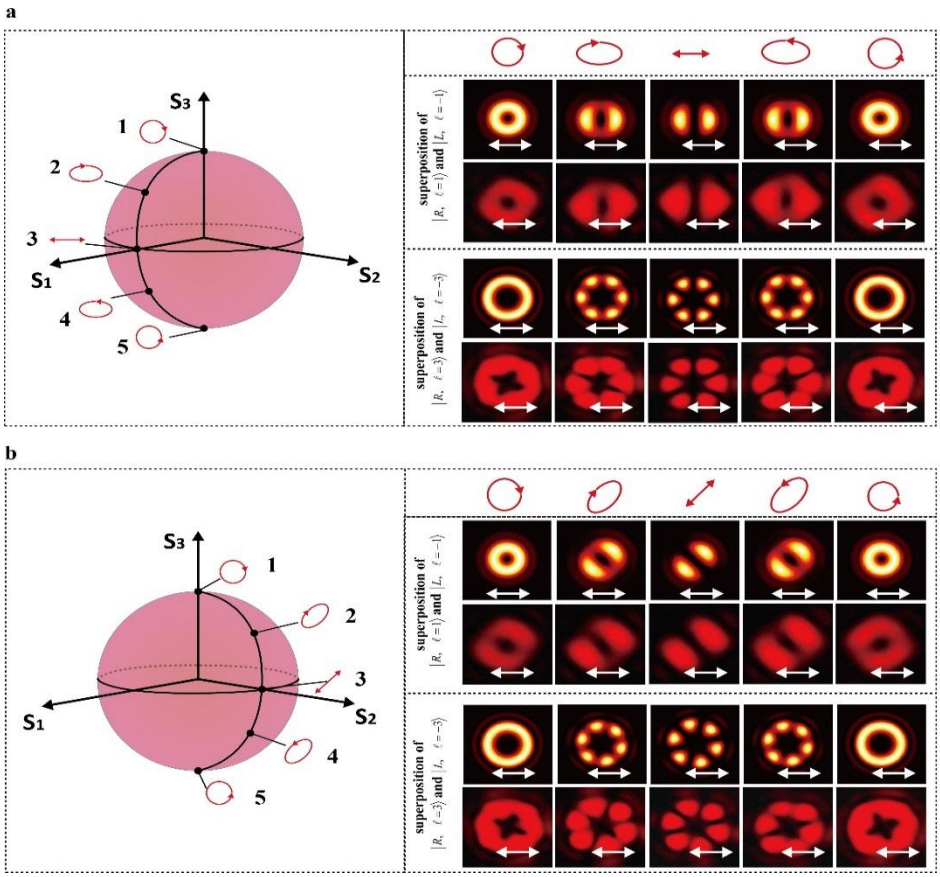


**Figure 3-17 Simulation and experimental measured results of polarization-controllable superposition of OAM states with the metasurface Sample1[2].** Poincaré sphere is adopted here to analyse different polarization states. **a** and **b,** simulated and experimental intensity profiles of generated. Points 1 to 5 on the Poincaré sphere represent different polarization states of incident light. The transmission axis of the analysing polarizer before the CCD camera is denoted by the white double-headed arrows.

Next step, we are going to investigate the relationship between the polarization state of incident light and the OAM superpositions, for Sample1 five polarization states are chosen which are RCP, REP, horizontal linear polarization, LEP, and LCP are chosen. The well-known Poincaré sphere is used to demonstrate the state of polarization of the incident light, and the five chosen polarization states are geometrically represented by the points located along a meridian trajectory on the Poincaré sphere shown in Fig.3-17. The

simulation and experimental measured output intensity profiles in four channels are given in the right part of Fig.3-17a, for each of five chosen polarization states. Then another five points located along the second meridian trajectory on the Poincaré sphere are chosen and corresponding output intensity profile are given in Fig.3-17b. The circular eigenstates of the above two group of five points have a π/2 phase difference which results in the rotation of the intensity profiles in Fig.3-17b.

The superposition of optical beams with opposite circular polarizations and orbital angular momenta can be used to create a light beam with non-trivial polarization and phase properties. A linear combination of an equal-weighted RCP optical vortex beam with topological charge of $\ell = 1$ and an LCP optical vortex beam with topological charge $\ell = -1$ can generate a radial vector beam, which has been applied in high resolution lithography [6], quantum memory [5], and metrology [13]. Complex superposition of light beams with opposite circular polarizations and different orbital angular momentum states may lead to interesting polarization topologies such as polarization singularities [29] and polarization Mobius strips [30]. The preparation of these structured light modes like Mobius strips may be important for complex light beam engineering. Our approach to realize the superposition of OAMs provides an efficient and fast way to produce the controllable superposition of OAM beams with opposite circular polarizations, which can also be used to generate optical beams with complex topological structures of phase and intensity. The novelty of this approach includes subwavelength resolution, multichannel OAM generation and polarization-controlled OAM coherent superposition, broadband, and compactness, which will have a broad impact in the optical communication, photonics, quantum sciences and other fundamental physics areas since it offers the opportunity to investigate extraordinary phenomena associated with spin and orbital conversion and further in further afield.

### 3.6 Summary

To summarize, we propose and experimentally demonstrate ultrathin metasurface devices which can simultaneously realize different functionalities in a multichannel manner. In order to demonstrate its capability, two examples are chosen to realize the OAM coherent superposition, and the polarization-controllable hologram and superposition of OAM, both are in multiple channels. By controlling the polarization state of the incident light, both the polarization-dependent holographic images and the OAM states and their superpositions are controlled at the same time. This facile approach provides a fast and efficient way for the generation, superposition and manipulation of the OAM states, and

the hologram images in multiple channels, which significantly simplifies the experimental system and is of great impact for the current efforts in reducing the size of the experimental setups in fields like quantum sciences, optical communication and so on.

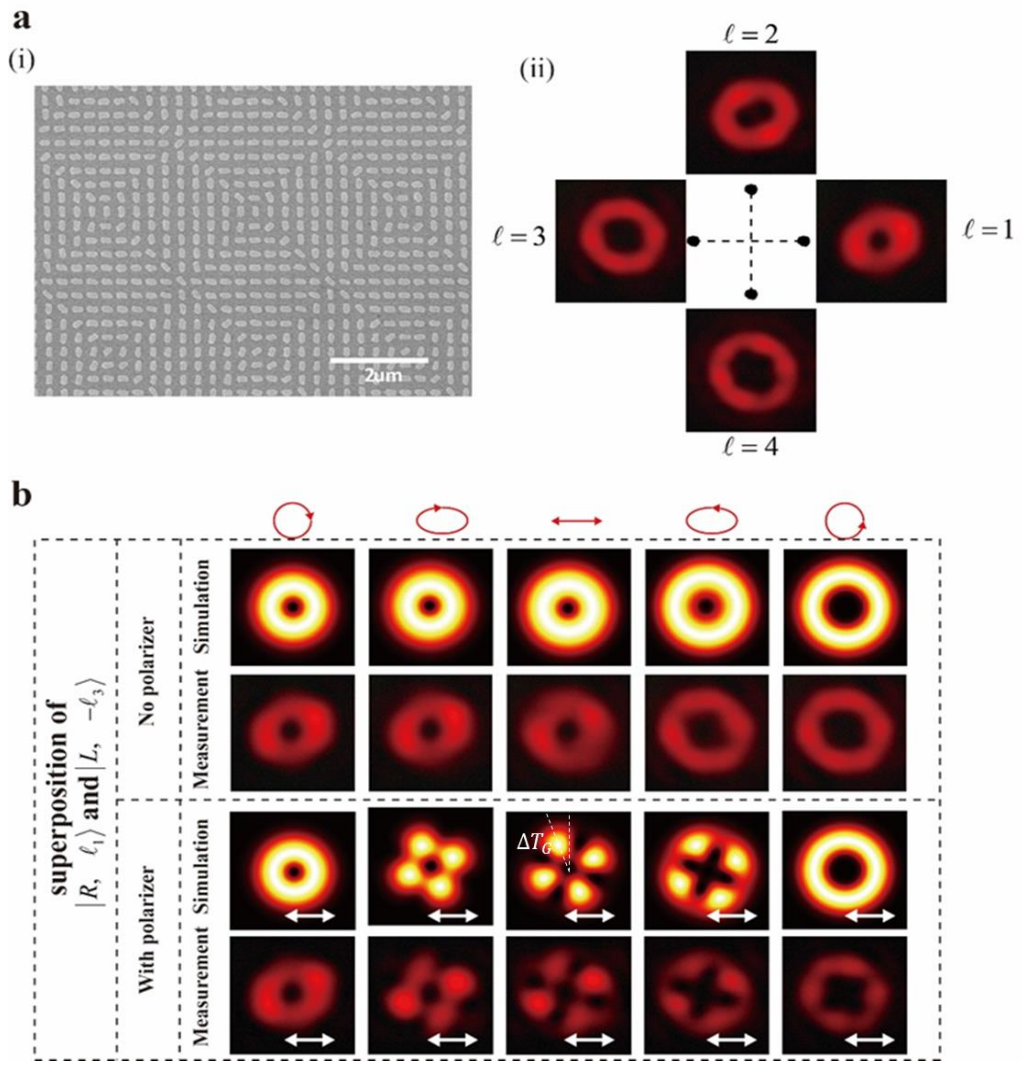


**Figure 3-18 Metasurface for realization of the four-channel OAM hybrid superpositions[2]. a)** (i) SEM image of the fabricated sample META3. (ii) Measured intensity profiles at four channels when the incident light is RCP Gaussian beam. **b)** Theoretical and experimental intensity profiles of the hybrid superpositions of OAM modes $|\boldsymbol{R}, \quad \ell = 1\rangle$ and $|\boldsymbol{L}, \quad \ell = -3\rangle$ . $\Delta\Gamma_G$ is the Gouy rotation introduced by the Gouy phase difference between the component beams during the propagation.

## 3.7 References


1. Zhang, C., et al., *Multichannel metasurface for simultaneous control of holograms and twisted light beams.* ACS Photonics, 2017. **4**(8): p. 1906-1912.

2. Yue, F., et al., *Multichannel Polarization-Controllable Superpositions of Orbital Angular Momentum States.* Advanced Materials, 2017. **29**(15): p. 1603838.

3. Allen, L., et al., *Orbital angular momentum of light and the transformation of Laguerre-Gaussian laser modes.* Physical Review A, 1992. **45**(11): p. 8185.

4. He, H., et al., *Direct observation of transfer of angular momentum to absorptive particles from a laser beam with a phase singularity.* Physical Review Letters, 1995. **75**(5): p. 826.

5. Nagali, E., et al., *Quantum information transfer from spin to orbital angular momentum of photons.* Physical review letters, 2009. **103**(1): p. 013601.

6. Karimi, E., et al., *Polarization-controlled evolution of light transverse modes and associated Pancharatnam geometric phase in orbital angular momentum.* Physical Review A, 2010. **81**(5): p. 053813.

7. Naidoo, D., et al., *Controlled generation of higher-order Poincaré sphere beams from a laser.* Nature Photonics, 2016. **10**(5): p. 327-332.

8. Nicolas, A., et al., *A quantum memory for orbital angular momentum photonic qubits.* Nature Photonics, 2014. **8**(3): p. 234.

9. Vaziri, A., G. Weihs, and A. Zeilinger, *Superpositions of the orbital angular momentum for applications in quantum experiments.* Journal of Optics B: Quantum and Semiclassical Optics, 2002. **4**(2): p. S47.

10. Marrucci, L., et al., *Spin-to-orbital conversion of the angular momentum of light and its classical and quantum applications.* Journal of Optics, 2011. **13**(6): p. 064001.

11. Fickler, R., et al., *Real-time imaging of quantum entanglement.* Scientific reports, 2013. **3**: p. 1914.

12. Padgett, M. and R. Bowman, *Tweezers with a twist.* Nature photonics, 2011. **5**(6): p. 343.

13. Willner, A.E., et al., *Optical communications using orbital angular momentum beams.* Advances in Optics and Photonics, 2015. **7**(1): p. 66-106.

14. Wang, J., et al., *Terabit free-space data transmission employing orbital angular momentum multiplexing.* Nature photonics, 2012. **6**(7): p. 488.

15. Lavery, M.P., et al., *Detection of a spinning object using light's orbital angular momentum.* Science, 2013. **341**(6145): p. 537-540.

16. D'ambrosio, V., et al., *Photonic polarization gears for ultra-sensitive angular measurements.* Nature communications, 2013. **4**: p. 2432.

17. Wen, D., et al., *Helicity multiplexed broadband metasurface holograms.* Nature communications, 2015. **6**: p. 8241.

18. Dorn, R., S. Quabis, and G. Leuchs, *Sharper focus for a radially polarized light beam.* Physical review letters, 2003. **91**(23): p. 233901.

19. Berg-Johansen, S., *S. Berg-Johansen, F. Töppel, B. Stiller, P. Banzer, M. Ornigotti, E. Giacobino, G. Leuchs, A. Aiello, and C. Marquardt, Classically entangled optical beams for high-speed kinematic sensing, Optica 2, 864 (2015).* Optica, 2015. **2**: p. 864.

20. Andersen, M., et al., *Quantized rotation of atoms from photons with orbital angular momentum.* Physical review letters, 2006. **97**(17): p. 170406.

21. Kovalev, A., V. Kotlyar, and A. Porfirev, *Asymmetric laguerre-gaussian beams.* Physical Review A, 2016. **93**(6): p. 063858.

22. Mair, A., et al., *Entanglement of the orbital angular momentum states of photons.* Nature, 2001. **412**(6844): p. 313.

23. Karimi, E., et al., *Spin-orbit hybrid entanglement of photons and quantum contextuality.* Physical Review A, 2010. **82**(2): p. 022115.

24. Fickler, R., *Quantum entanglement of complex structures of photons*. 2015: Springer.

25. Bhatti, D., J. von Zanthier, and G.S. Agarwal, *Entanglement of polarization and orbital angular momentum.* Physical Review A, 2015. **91**(6): p. 062303.

26. Yi, X., et al., *Hybrid-order Poincaré sphere.* Physical Review A, 2015. **91**(2): p. 023801.

27. Galvez, E.J., et al., *Poincaré-beam patterns produced by nonseparable superpositions of Laguerre–Gauss and polarization modes of light.* Applied optics, 2012. **51**(15): p. 2925-2934.

28. Baumann, S., et al., *Propagation dynamics of optical vortices due to Gouy phase.* Optics Express, 2009. **17**(12): p. 9818-9827.

29. Slinger, C., C. Cameron, and M. Stanley, *Computer-generated holography as a generic display technology.* Computer, 2005. **38**(8): p. 46-53.

30. Yaraş, F., H. Kang, and L. Onural, *Real-time phase-only color holographic video display system using LED illumination.* Applied optics, 2009. **48**(34): p. H48-H53.

31. Xu, F., J.E. Ford, and Y. Fainman, *Polarization-selective computer-generated holograms: design, fabrication, and applications.* Applied optics, 1995. **34**(2): p. 256-266.

32. Ford, J.E., et al., Optics letters, 1993. **18**(6): p. 456-458.

33. Yu, W., et al., *Polarization-multiplexed diffractive optical elements fabricated by subwavelength structures.* Applied optics, 2002. **41**(1): p. 96-100.

34. Kostuk, R.K., M. Kato, and Y.-T. Huang, *Polarization properties of substrate-mode holographic interconnects.* Applied optics, 1990. **29**(26): p. 3848-3854.

35. Jacob, S. and Y. Yuval, Nature Nanotechnology, 2015. **10**(4).

36. Lavery, M.P.J., et al., Science (New York, N.Y.), 2013. **341**(6145): p. 537.

37. Zhan, Q., Optics Express, 2012. **20**(6): p. 6058-6059.

38. Khorasaninejad, M., et al., *Metalenses at visible wavelengths: Diffraction-limited focusing and subwavelength resolution imaging.* Science, 2016. **352**(6290): p. 1190-1194.

# Chapter 4 Metasurface devices for polarization manipulation

The main focus of last chapter was how metasurface device can be used to manipulate the phase of light. In many occasions of the modern optics, it is desirable to be able to control polarization state of light beam at will. In this chapter, we will demonstrate how to manipulate the polarization state of light by using metasurface devices. Three metasurface devices [1-3] are designed, fabricated and verified for this purpose. The first two samples are used to demonstrate how we hide an image in a laser beam. The object we hide here are images, either a grayscale image or a color image. First, a high-resolution grayscale image of James Clark Maxwell hiding in a laser beam with a spatially inhomogeneous state of polarization is presented[2]. Then as an application of the presented approach, a black-and-white QR code is hidden in a laser beam, which can be of great interest for the field of anti-counterfeiting and security[1]. Finally, a dielectric metasurface is designed to encode a color image into the generated polarization profiles[3].

## 4.1 Introduction

Hide-and-seek is a popular children's game in which some players hide themselves in the surrounding environment, to be found by the seekers. In order to make the game more fun, normally a spacious place is required in such a game. However, it is more challenging to play such a game in a laser beam due to its extreme small beam size. Benefiting from the unique advantage of the metasurfaces, it is possible to hide a high-resolution image in the inhomogeneous polarization profile of the laser beam and transfer the hidden information along the propagation direction of the light. Unlike the optical holograms[4, 5], recently demonstrated color images hidden in a terahertz metasurface [6], and a QR code encoded in the spatial amplitude modulation of a light beam generated by a metasurface [6], the images in the following three demonstrations are all encoded in the inhomogeneous polarization profile of light beam which has uniform intensity distribution.

## 4.2 Malus law

Polarization of light refers to a direction in which the electric component of the light field oscillates. A light beam becomes polarized in a specific direction after it passes through a linear polarizer. When a completely plane polarized light impinges on an analyser, the intensity of the light transmitted by the analyser is proportional to the square of the cosine

of angle between the transmission axes of the analyser and the polarizer (see Fig.4-1). Suppose the angle between the transmission axis of the analyser and the polarizer is θ, the intensity of light transmitted by the analyser is I = I0cos2θ, where I0 is the intensity of incident light. This is the well-known Malus law in optics[7]. Such a beam usually has a homogeneous polarization states after passing through a polarizer, while a structured beam can have an inhomogeneous distribution of polarization in the transverse plane perpendicular to its propagation, providing a new degree of freedom to hide an image in the light beam. Based on the Malus law, an arbitrary grayscale image can be hidden in the polarization profile of a light beam.

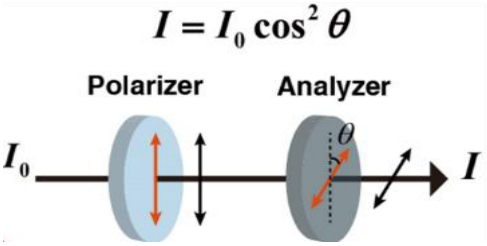


**Figure 4-1 Malus law.** The intensity of a beam of plane-polarized light after passing through a rotatable polarizer varies as the square of the cosine of the angle between the transmission axes of these the polarizer and the analyser[3].

## 4.3 Hiding a grayscale image in the laser beam through a reflective metasurface

### 4.3.1 Design and method

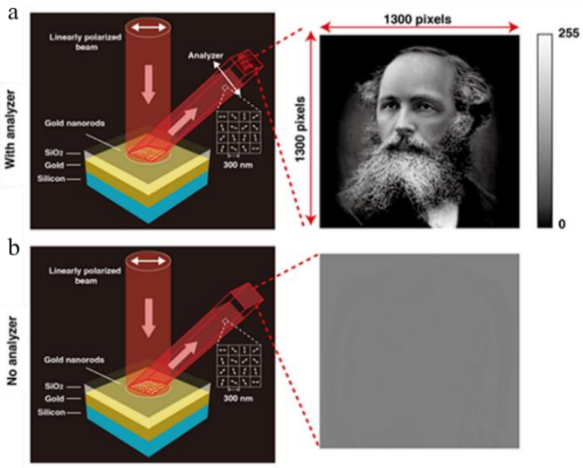


**Figure 4-2 The design schematic for hiding a high-resolution grayscale image[2].** Under the illumination of linearly polarized light, two reflected beams with a spatially variant linear polarization profile are generated, which can be used to hide a high-resolution grayscale image (256 levels, grayscale). The two beams are exactly the same apart from the propagation direction, and for demonstration purpose only one reflected beam is presented here. (a) The hidden image is revealed by an analyser (linear polarizer), and (b) No image can be observed without the analyser.

Fig.4-2 shows the schematic of our approach for hiding an image in a laser beam. When the metasurface sample is illuminated by a linearly polarized laser beam at normal incident, structured beam with a spatial-variant polarization profile is generated, and a grayscale image is hidden in this beam. The hidden image will be revealed if an analyser is used, otherwise the target image cannot be observed. It is worth mentioning that actually two centro-symmetrically identical reflected beams are generated in this approach, and only one reflected beam is given in Fig.4-2 for demonstration purpose. An analyser (linear polarizer) is used to reveal the hidden image in the generated structured beam. In memory of the milestone work of James Clerk Maxwell in electromagnetics, one of his grayscale portraits (1300×1300 pixels) is used here as an example image, to be hidden in the laser beam. The right column in Fig.4-2a and Fig.4-2b shows the simulation results with and without an analyser in the reflective light path.

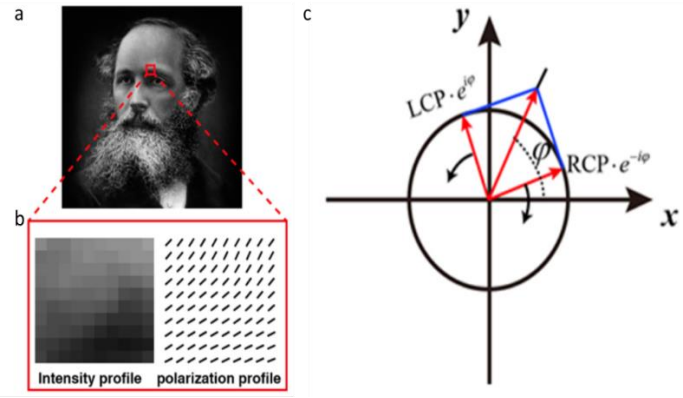


**Figure 4-3 Image intensity profile and polarization distribution.** (a) The target image of James Clerk Maxwell's grayscale portrait (1300×1300 pixels). (b) The details of selected area from the eyebrow area with 10×10 pixels. The left side gives the grayscale profile and the right side shows the required polarization distribution for the analyser with a transmission axis along the vertical direction. (c) A linear polarization can be generated by a coherent superposition of two planar circularly polarizations with opposite handedness which propagate along the same direction[2].

Fig.4-3a shows the high-resolution grayscale image of James Clerk Maxwell that we are going to hide in our design. The target image has a dimension of 390 um by 390 um with 1300×1300 pixels, and each pixel has a size of 300 nm by 300 nm, demonstrating a subwavelength resolution. To explain the method adopted here, an area from the eyebrow area with 10×10 pixels (Fig.4-3a) is selected and showed in detail (Fig.4-3b). The enlarged intensity profile and the corresponding polarization distribution in each pixel are given in the left and right of Fig.4-3b, respectively. In this design, the first polarizer before

the metasurface and the analyser (second polarizer) after the metasurface are along horizontal and vertical directions, respectively.

To elucidate the design method in detail, the required light beam with an inhomogeneous linear polarization profile used as incident light in our approach can be decomposed into the superposition of two circularly polarized beams with equal components and opposite helicity (Fig.4-3c), which can be described as

$$\vec{E}(x,y) = E_0(\vec{x}cos\varphi(x,y) + \vec{y}sin\varphi(x,y))$$

$$= \frac{1}{\sqrt{2}}\left(\exp\left(i\varphi(x,y)\right)\hat{e}_R + \exp\left(-i\varphi(x,y)\right)\hat{e}_L\right) \quad (4\text{-}1)$$

where $\varphi(x,y)$ is the relative phase difference between the two orthogonal polarization states, $\hat{e}_L = (\hat{x} + i\hat{y})/\sqrt{2}$ and $\hat{e}_R = (\hat{x} - i\hat{y})/\sqrt{2}$ are unit vectors of the left circular polarization (LCP) and the right circular polarization (RCP). $\hat{x}$ and $\hat{y}$ are unit vectors along *x* and *y* directions. A geometric metasurface has already been used to realize the handedness-dependent phase profile while maintaining constant amplitude [7-9]. The key point in this approach is to combine these two sets of phase profiles which have opposite incident handedness on the same metasurface, and to realize the image hidden functionality. In order to ensure the co-propagation of these two circularly polarized light beams and make sure they will meet and interfere with each other, the metasurface sample is used to generate the final desired structured beams through manipulating the superposition of these two beams with opposite circular polarization states emerging from the identical metasurface (Fig.4-4a). To eliminate the effect of the non-converted beam, the off-axis configuration is adopted in this design. The important step of this method is to generate a phase profile that, upon the illumination of circularly polarized light, a pair of centrosymetrically distributed off-axis beams with identical phase profile with respect to the surface normal can be generated simultaneously. The phase distribution can be written as[10],

$$\Phi(x,y) = \arg(\exp(i\varphi(x,y) + \delta_x)) + \exp(i\varphi(x,y) - \delta_x))) \quad (4\text{-}2)$$

Where $\varphi(x,y)$ represents the position-dependent phase difference between the two orthogonal polarization states. $\pm\mathcal{S}(x)$ is an additional phase profile that is used to

produce the phase gradient for the off-axis reflection (±1 order) along x direction. The angle of reflection is determined by the equation [11, 12]

$$\sin(\alpha_r) - \sin(\alpha_i) = \frac{\lambda_0}{2\pi n_i} \frac{d\delta(x)}{dx} \tag{4-3}$$

where $\alpha_r$ and $\alpha_i$ are the reflection and incident angle, $\lambda_0$ is the wavelength in vacuum, $n_i$ is the refractive index of the medium. Due to the sign of the geometric phase generated at the interface of metasurface depending on the handedness of the incident light, when the incident beam is changed from RCP to LCP, or from LCP to RCP, a pair of off-axis beams with the phase profile of $-\Phi(x,y)$, or $\Phi(x,y)$ , are generated. Obviously, when the incident light is of linear polarization, the reflected beams with opposite handedness (beams with RCP and LCP) will meet, interfere, and generate the desired polarization profile which is used for the purpose of hiding the image on both sides, as shown in Fig.4-4.

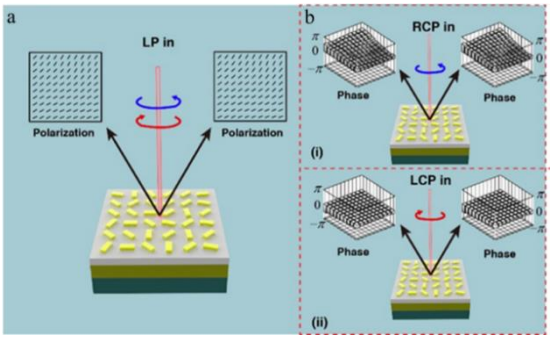


**Figure 4-4 The mechanism of the polarization manipulation via the metasurface[2].** The polarization states of incident beam in b(i) and b(ii) are right circular polarization (RCP) and left circular polarization (LCP), respectively. A pair of off-axis beams with phase profile $\Phi(x,y)$ (or $-\Phi(x,y)$ ) are generated by shining the metasurface with light beam with RCP (or LCP). When a linearly polarized (LP) beam is incident on the metasurface, the reflected beam with opposite circular polarization and equal components will meet and generate the required polarization profile on both sides (a).

### 4.3.2 Sample fabrication

The reflective metasurface is composed of three layers: a gold ground layer, a silicon dioxide (SiO2) spacer layer, and a top layer of gold nanorods with space-variant orientations and same geometry. Standard electron-beam lithography (EBL) and the following lift-off process are used to fabricate the designed metasurface. First, silicon substrates are cleaned with acetone in ultrasonic bath for 10 min followed by isopropyl alcohol (IPA) for 10 min. Then the substrates are rinsed in deionized water and dried with

compressed air. After that, the gold layer (150 nm) is deposited onto the silicon substrate by using the electron beam evaporator followed by the deposition of silicon dioxide (SiO2) layer (85 nm). The film thickness is controlled by using a calibrated film thickness monitor. The positive poly methyl methacrylate (PMMA) 950 A2 resist is spin coated on the SiO2 layer at 1000 rpm for 60s followed by 1500 rpm for 15s, producing a PMMA film with a thickness of 100 nm. Then the sample is baked on a hotplate at 180°C for 5 minutes. The nanopatterns are defined in the PMMA film using EBL (Raith PIONEER, 30 KV). The sample is developed in the developer (MIBK:IPA=1:3) for 45 s, followed by the stopper (IPA) for 45 s. A thin gold layer (30 nm) is deposited on the developed sample using electron beam evaporator. For the adhesion purpose, a thin titanium layer (3 nm) is deposited on the SiO2 layer prior to the gold layer. Finally, the metasurface (see Fig.4-5) is ready for characterization after the lift-off process in acetone.

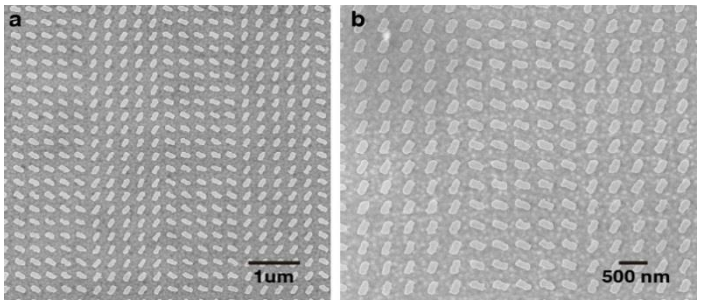


**Figure 4-5 The scanning electron microscope (SEM) images of the fabricated metasurface sample at (a) scale bar 1 μm. (b) Scale bar 500nm.**

### 4.3.3 Results

The experimental setup consists of a linear polarizer before the metasurface sample, 3D adjustable sample holder, objective, an analyser and a CCD camera, as shown in Fig. 4-6.

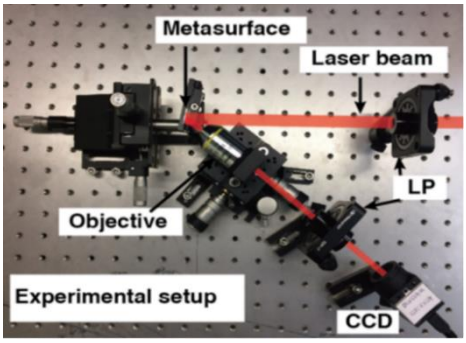


**Figure 4-6. Experimental setup for the sample characterization[1].** A linear polarizer is used to generate the linearly polarized incident light, upon reflection, an objective, analyser and a CCD camera together to reveal the hidden image.

Human eyes are naturally not sensitive to the polarization topology or its change of light, therefore an analyser (analysing liner polariser) is used to reveal the hidden grayscale image, as shown in Fig.4-6. Upon doing so, we confirm the existence of target image indirectly through its intensity profile (grayscale image), rather than directly observing the spatially-variant polarization profile of the laser beam. The pixel size of the CCD camera used in the experiment is 4.65um which is larger than the pixel size of the image hidden in the resultant beam, therefore the hidden image cannot be resolved directly by the CCD camera. An objective with a magnification of 10X is used to expand the hidden image for visualization purpose.

Fig.4-7a shows the simulation result and the image captured in the experiment, when the transmission axis of the polarizer is fixed along horizontal direction and the transmission axis of the analyser along the vertical direction. Because in the theoretical model and the design procedure, the amplitude of the two beams are assumed to be the same, so there will be no image in the beam (Fig.4-7a top left) without the aid of the analyser. The experimental result in Fig.4-7a (top right) indicates that the image-hidden functionality is realized. The slight discrepancy between experiment and simulation is mainly due to the imperfection of the experimental setup and the fabrication errors. Unsurprisingly, a high-quality image is revealed when the analyser is in place and its transmission axis is fixed along the vertical direction. Good agreement between the simulation results and the images acquires during the experiment can be found. Based on the off-axis design adopted here, another identical image can be observed in the reflected beam on the other side of metasurface sample with respect to the surface normal. During the experiment, the whole image of James Clerk Maxwell and his moustache, eyeball, eyebrow and other details of the picture are clearly observed, indicating the ultrahigh resolution of the proposed method. The pixel numbers of the monochrome CCD (1280×1024) in our experiment is slightly less than that of the target image (1300×1300).

To characterize the grayscale distribution, an area from the experimentally measured picture is selected (see red rectangular in Fig. 4-7b) and the histogram that shows the distribution of intensities against grayscale level (see Fig.4-7b) is plotted. This histogram clearly shows that the experimentally captured picture covers the grayscale range of 0-255, agreeing well with the original grayscale image.

Next step of the observation would be to analyze the dependence of simulated and measured results on the direction of transmission axis of the analyser. By fixing the position of transmission axis of the polarizer before the metasurface sample, and rotating the analyser before the CCD camera, at four points of the angles between these two

transmission axes of $0$, $\pi/4$, $\pi/2$ and $3\pi/4$, a good agreement between experimental and simulation results is found, which is given in Fig.4-8. During this procedure one of the interesting findings is that two images for the analyser with orthogonal directions of transmission axis (e.g. $0$ and$\pi/2$, $\pi/4$ and $3\pi/4$ ) are complementary grayscale images. The evolution process of the revealed images can be clearly observed when the analyser is rotated gradually.

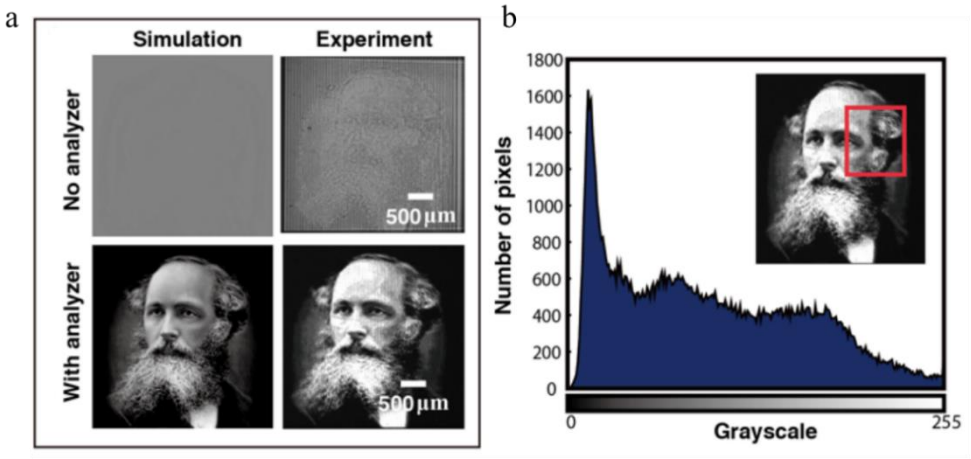


**Figure 4-7** (**a**) The simulated and experiment results with and without the analyser. Note that the direction of the transmission axis of the analyser is along vertical direction. (b)The image histogram of a selected area of experimently measured image. The histogram is plotted with 256 equally spaced intervals, and then calculating the total number of pixels for each value[2].

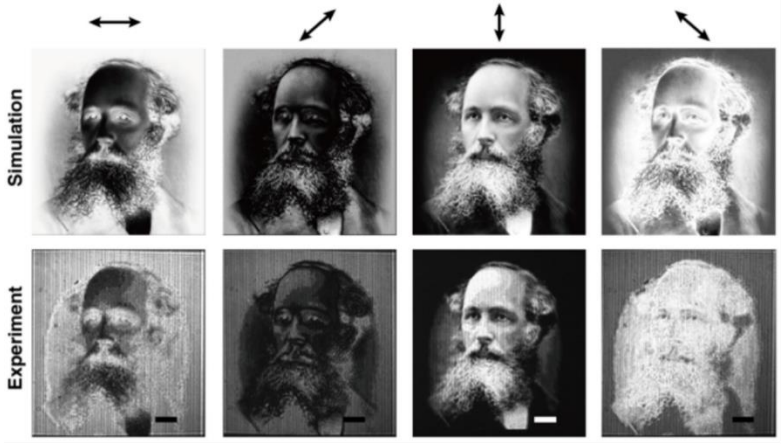


**Figure 4-8 The simulated and experimental results for the analyser with various directions of transmission axis (represented by the black arrows at the top)**. Results at of $0$, $\pi/4$, $\pi/2$ and $3\pi/4$ are given. The scale bar of the images is 500µm[2].

According to the Malus' Law, the intensity of the light transmitted by an analyser is directly proportional to the square of the cosine of angle between the transmission axes of the analyser and the polarizer. Thus, the quality of the hidden image (in comparison

with target image) should be the same once the angle between the transmission axes of the analyser and the polarizer is fixed. Therefore what we did as the next step of our characterization procedure is to set the transmission angle of the polarizer at $0$, $\pi/4$, $\pi/2$ and $3\pi/4$(see double-headed red arrows in Fig.4-9), then adjust the analyser to make sure that the transmission axis of the analyser (double-headed black arrows in Fig.4-9) is perpendicular to that of the polarizer. The simulation and experiment result for this setting is given in Fig.4-9, indicating that the clear images are revealed in these different cases. The experimentally obtained images are captured with a monochrome CCD camera at the wavelength of 640 nm. From all the results so far, we can conclude that the best image quality is found when the angle between the transmission axes of the analyser and the polarizer fixed at $\pi/2$.

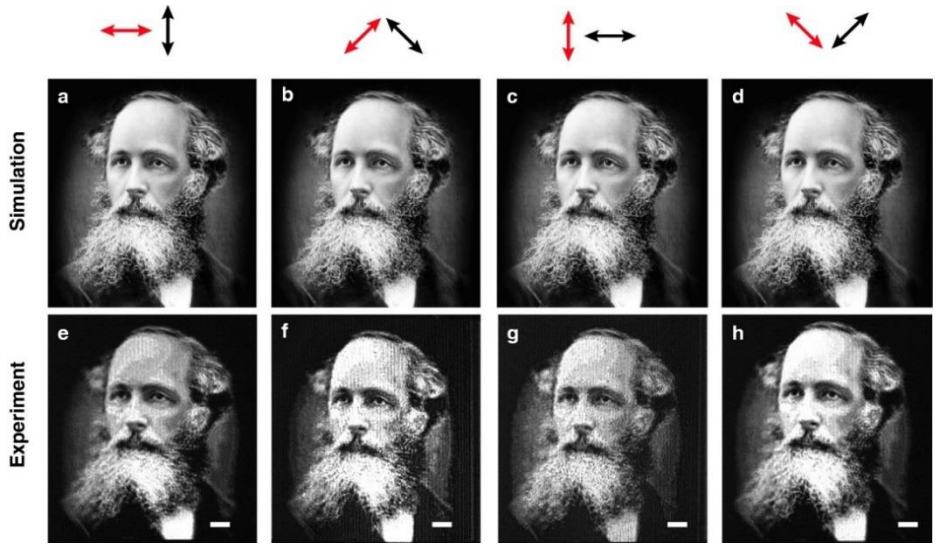


**Figure 4-9 The simulated and experimentally obtained images when the angle between the transmission axes of the analyser and the polarizer is fixed at 90º**[2].The red and black double-headed arrows represent the transmission axes of the linear polarizer and the analyser, respectively. The transmission axis of the polarizer is set at $0$, $\pi/4$, $\pi/2$ and $3\pi/4$ with respect to the horizontal direction, and the analyser is adjusted to maintain the transmission axis of the analyser perpendicular to that of the polarizer.(**a-d**) Simulated images and (**e-h**) Experimental images. Scale bar 500μm.

To better understand the image hidden approach, the dependence of image on the incident polarization state is also investigated during the characterization process. Although the metasurface device is designed to work on linearly polarized incident light, it should also work when the incident light is of elliptical polarization, since an elliptically polarized light consists of LCP light and RCP light components, which therefore will meet and interfere with each other as what a linearly polarized incident light does, as stated before. However, the image quality will be deteriorated when comparing with the case when the incident light is of linear polarization. When we investigate the impact of different

polarization states of the incident light, the transmission axis of the analyser is fixed along the vertical direction. In order to generate different states of polarization of incident light, a quarter wave plate is inserted into the light path, located between the metasurface sample and the polarizer. By changing the angle between the transmission axis of the polarizer and the fast axis of the quarter wave plate, five typical polarization (see Fig.4-10) state can be generated. The simulated and experimentally observed images are given under different circumstances in Fig.4-10. Although the image quality at LCP and RCP incident light is different from the corresponding simulation results, the dependence of the observed images on the polarization states of the incident light agrees well with the prediction. The difference between the experiment results and the corresponding simulated results for circular polarization states is mainly due to the imperfection of the experimental setup (e.g., our design is based on ideal plane wave) and errors introduced in the sample fabrication process.

Unsurprisingly, benefiting from the broadband nature of the geometric metasurface, the developed metasurface device can operate in the broadband. Within the visible range, the wavelengths of 500 nm, 550 nm, 600 nm, 633 nm and 700 nm are chosen, and the revealed vivid images (Fig.4-11) during the experimental measurement clearly show the capability of the designed and fabricated metasurface. From this point of view, we can say that a brand new image hidden approach is experimentally demonstrated here, which can have an immediate impact in security and anti-counterfeiting which will be demonstrated in the next part of this thesis.

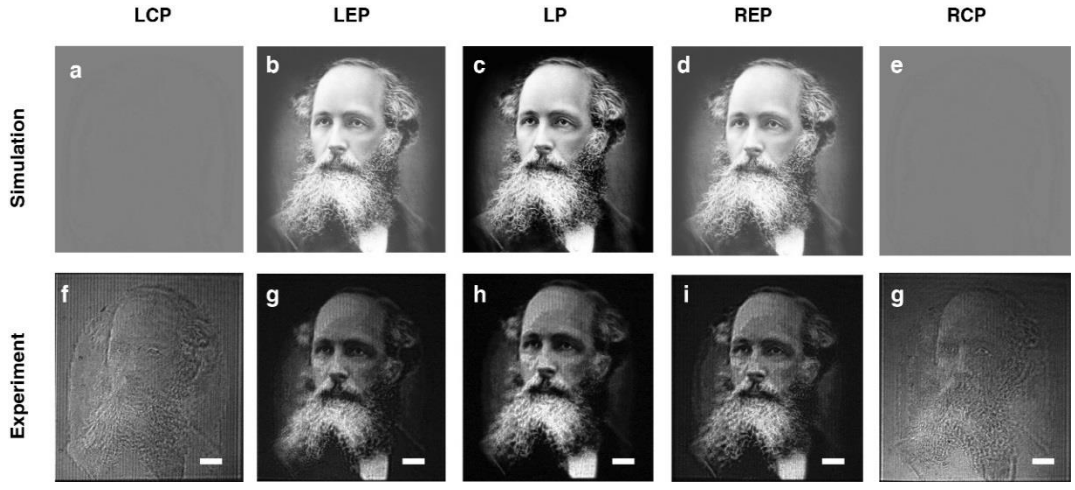


**Figure 4-10 Simulated and experimentally measured results versus incident polarization states at 640 nm[2].** The polarization states of the incident light are chosen to be LCP, left-handed elliptically polarized (LEP), linearly polarized (horizontal) (LP), right-handed elliptically polarized (REP) and RCP.(**a-e**) Simulated images.(**f-g**) Experimental images. Scale bar, 500 $\mu m$ .

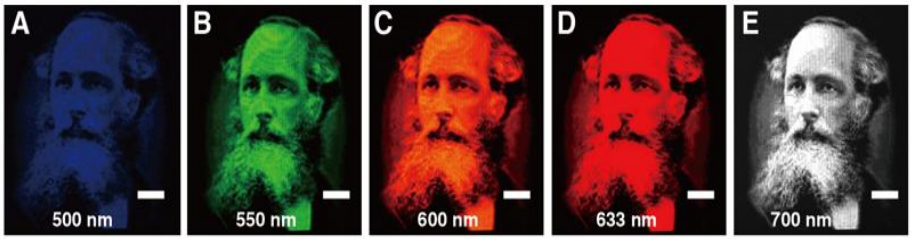


**Figure 4-11. Broadband performance of the fabricated metasurface[2].** In the visible range, 500nm, 550nm, 600nm, 633nm and 700nm are chosen to showcase the performance of the sample, and vivid images are obtained in the experiment in these wavelengths. Note that the images of (**A-D**) are captured by the colour CCD with pixel numbers 1024×768. The image of (**E**) is captured by the monochrome CCD with pixel numbers 1280×1024. Scale bar here is 500 μm .

It is well known that the mirror reflection and lens modulation can deteriorate the polarization states of a polarized light beam. Since this sample is designed on the basis of polarization profile of the light, therefore, we need to further investigate the performance of the sample when mirrors or lenses are within the optical system. To explore such an effect, an experimental setup including several lenses and mirrors are used. Fig.4-12b presents the measured images at the distance of 4 meters (from metasurface to CCD camera) after the generated structured beams are reflected several times. Although the image quality deteriorates, it can still be clearly seen at such a long distance, showing potential applications in areas like optical communications and so on.

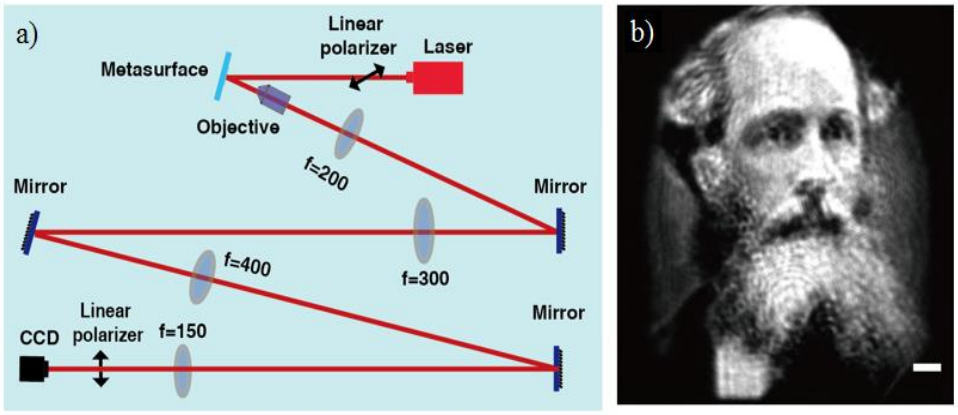


**Figure 4-12 Robustness of the proposed approach [2].** (a) The experimental setup for the characterization of the hidden image for long distance propagation. Three mirrors and four lens with various focus lengths are adopted in the experimental setup. (b) The obtained image at the point 4 meters after the metasurface. Scale bar, 500 μm

Then a hexagonal light pipe is used as a waveguide to test the image quality. Fig.4-13a and Fig.4-13c are the image captured before and after the waveguide, respectfully. One can see that the details of the image, such as eyeball, moustache and other parts are all

very clear and nearly the same as the image before entering the waveguide. Here the image is flipped due to the times of total reflection inside of the light pipe.

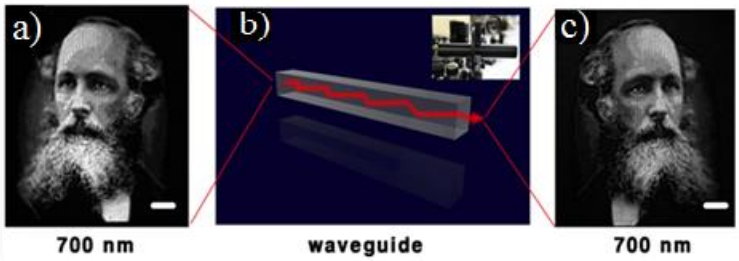


**Figure 4-13 Experimental results when the light beam with hidden image (a) before and (b) after a waveguide [2].**

To characterize the performance of the developed device, the metasurface is exposed to a tunable light beam from a supercontinuum laser source (NKT-SuperK EXTREME) to calculate the conversion efficiency. Our design is to generate the required linear polarization distribution, which is realized by the superposition of two orthogonal circularly polarized beams with certain phase profile. The two orthogonal circularly polarized beams should have the equal power and propagate exactly along the same direction. The key point is to design a phase profile that, upon the illumination of circularly polarized light, can simultaneously generate a pair of centro-symetrically distributed off-axis beams with identical phase profile with respect to the normal axis. During the experiment, the output power of two reflected off-axis beams at both sides under the illumination of right-handed circularly polarized light is measured. The total power of two beams is then normalized to unity. The relative power of two beams is shown in Fig. 4-14 (a). It is clear that the power of the two beams remains equal over a broadband wavelength range (640-960 nm). The conversion efficiency is defined by the total power of two output beams divided by the power of incident light (see Fig. 4-14 (b)). The maximum conversion efficiency reaches about 60% at the wavelength of 820 nm. The difference between simulation and experimental results is mainly caused by the titanium adhesion layer which lies between nanopattern layer and $SiO_2$ layer and the fabrication errors.

To summarize this part, we propose and design a metasurface device which can successfully hide a high-resolution grayscale image in the polarization topology of a laser beam, and this image will be revealed when the angle between the transmission axis of analyser and that of the polarizer is fixed at $\pi/2$. The uniqueness of this approach lies in image hidden and precise polarization manipulation and high performance in resolution, bandwidth, and compactness of the device, making it very attractive for diverse

applications in the areas such as encryption, imaging, anti-counterfeiting, optical communications, quantum science, light-matter interactions and fundamental physics.

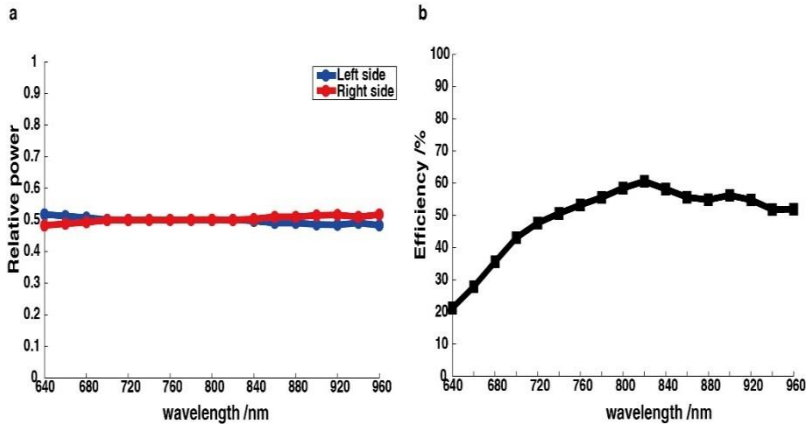


**Figure 4-14 The relative power of two reflected beams and the conversion efficiency of the designed metasurface device[2].** (**a**) The measured relative power of two reflected beams at two sides under the illumination of right-handed circularly polarized light. (**b**) The measured conversion efficiency is defined as the power sum of the two reflected beams divided by the power of incident beam.

### 4.4 Hiding a QR code for anti-counterfeiting purpose

Quick response (QR) codes are two-dimensional barcodes consisting of usually black and white patterns with spatially varying intensity profile, which can be processed by a QR reading machine, such as a smart phone. QR codes have been widely used in many fields, including product identification, item tracking and document management.

As another demonstration of above proposed idea, we experimentally demonstrate a single reflective metasurface device that can generate a quick response (QR) code which is embedded in the polarization profile of a laser beam. The desired structured beam is generated by manipulating the superposition of two beams with opposite circular polarization states emerging from the identical metasurface (Fig.4-15).

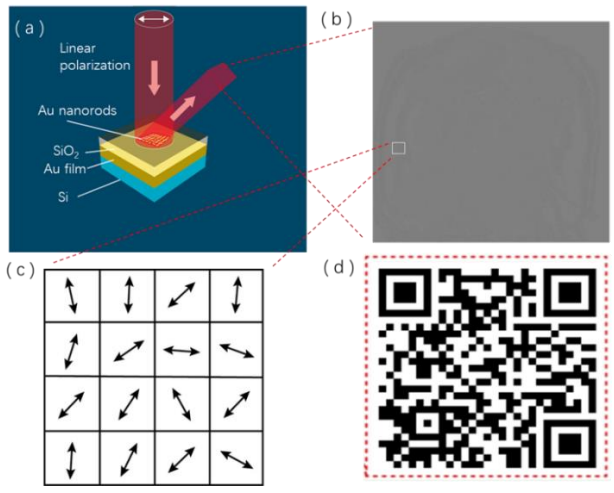

**Figure 4-15 Schematic of the mechanism to hide a QR code in a laser beam[1].** (a) Schematic of design. (b) Intensity profile. (c) Schematic of polarization distribution in the white square area in (b). (d) Target QR code.

Figure 4-15a shows the schematic of our proposed approach for hiding a QR code. The vector beam that can be used to hide the QR code is created by a reflective metasurface illuminated by a linearly polarized light beam at normal incidence. The resultant vector beam has a uniform intensity profile (Fig.4-15b) and an inhomogeneous spatial polarization profile (Fig.4-15c), which cannot be detected by human naked eyes or cameras. The hidden QR code (see Fig.4-15d) is revealed by using a linear polarizer (analyser), which can reconstruct the encoded pattern.

A single reflective metasurface is designed to generate the desired structured beams by manipulating the superposition of two beams with opposite circular polarization states emerging from the identical metasurface (see Fig.4-4a). Different from a common polarized laser beam, which typically has only one polarization state, here different parts of the beam have different polarization states (spatially variant). The generation of desired polarization profiles with two opposite handedness and their superposition process occur on the same metasurface by controlling the polarization state of the incident light. The required light beam with an inhomogeneous linear polarization profile can be decomposed into the superposition of two circularly polarized beams with equal components and opposite handedness. A linear polarization is generated by a coherent superposition of two planar circularly polarized beams with opposite helicity but propagating along the same direction. Therefore, under the illumination of incident light with circular polarization, one needs a phase profile that can simultaneously generate a pair of centrosymetrically distributed off-axis beams with same phase profile with respect to the propagation axis of the incident light[10]. Since the sign of the geometric phase generated at the interface of metasurface only depends on the handedness of the incident light, under the illumination of a linearly polarized beam, the off-axis reflected beams with opposite handedness will meet and interfere with each other resulting the desired polarization profile for the hidden image on both sides.

The reflective metasurface consists of three layers: a top layer of gold nanorods, a gold ground layer, and a silicon dioxide ($SiO_2$) spacer layer sandwiched between them. It is worth mentioning that all the nanorods have same geometry but different orientation angles. The standard electron-beam lithography (EBL) and subsequent lift-off process are used to fabricate the designed metasurface. Initially, silicon substrates are cleaned with acetone in ultrasonic bath for 10 min followed by isopropyl alcohol (IPA) for 10 min.

Then the substrates are rinsed in deionized water and dried with compressed air. After that, the gold layer (150 nm) is deposited onto the silicon substrate by using the electron beam evaporator followed by the deposition of silicon dioxide ($SiO_2$) layer (85 nm). The film thickness is controlled by using a calibrated film thickness monitor. The positive poly methyl methacrylate (PMMA) 950 A2 resist is spin coated on the $SiO_2$ layer at 1000 rpm for 60s followed by 1500 rpm for 15s, producing a PMMA film with a thickness of 100 nm. Then the sample is baked on a hotplate at 180$^{o}$C for 5 mins. The nanopatterns are defined in the PMMA film using EBL (Raith PIONEER, 30 KV). The sample is developed in MIBK: IPA (1:3) for 45 s followed by stopper (IPA) for 45 s. A thin gold layer (30 nm) is deposited on the developed sample using electron beam evaporator. For the adhesion purpose, a thin titanium layer (3 nm) is deposited on the $SiO_2$ layer prior to the gold layer. Finally, the metasurface is ready for characterization after the lift-off process in acetone. The metasurface device has a dimension of 300 μm by 300 μm. Fig.4-17a shows the SEM image of the metasurface. In order to visualize the hidden QR code, an analyser is used to reveal the hidden information in the polarization topology of the laser beam. In doing so, we do not directly observe the spatially-variant polarization profile of the laser beam but rather indirectly confirm its existence through the intensity profile behind the analyser and the interference fringes resulted from the right and left circular components. The experimental setup used to characterize the fabricated sample is shown in Fig.4-17b.

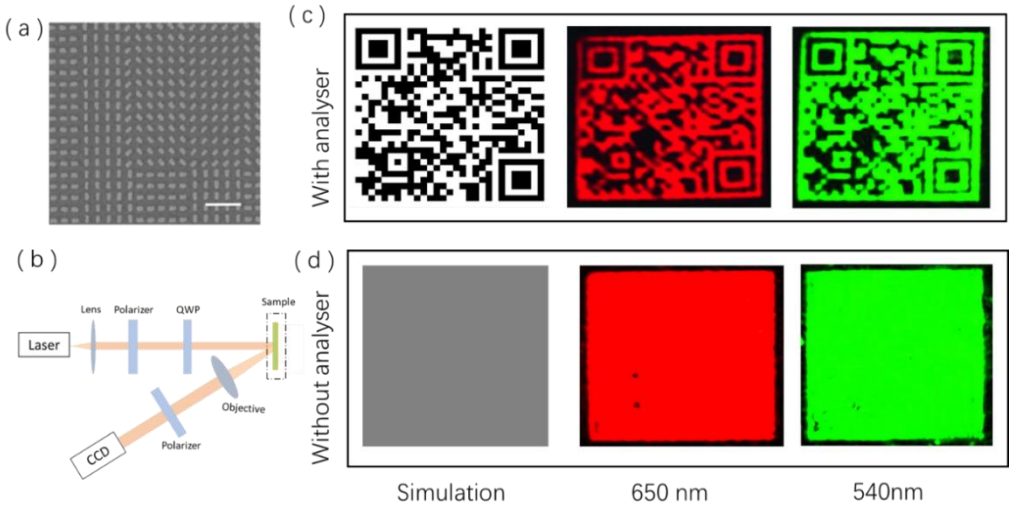


**Figure 4-16 Simulation and experimental results[1].** (a) SEM image of the fabricated sample. The scale bar is 1 μm. The size of fabricated sample is 300 μm by 300 μm. Each unit cell is 300 nm by 300 nm. (b) Schematic of experimental setup. QWP: quarter waveplate. Simulation and experimental results (c) with and (d) without the analyser.

Fig.4-16b is the schematic of experimental setup. To characterize the performance of the active metasufaces, a tunable laser source (NKT-SuperK EXTREME) is used to generate the desired laser beam with various polarization states after passing through a quarter-wave plate (QWP) and a polarizer in front of the sample. An objective with a magnification of 10× is used to expand the image for visualization with a charge-coupled device (CCD) camera. Fig.4-16c and 4-16 show the simulation and experimental results with and without the analyser under the illumination of linearly polarized light beams. The figures in Fig.4-16c and Fig.4-16d on the left, middle and right columns represent the simulation results and experimental results at 650 nm and 540 nm, respectively. The slight difference between experiment and simulation is due to the imperfection of the sample and measurement error. Although the device is designed at the operating wavelength of 650 nm, it can operate in a broad wavelength range due to the broadband nature of the geometric metasurface. The experimental results at 540 nm (see right column of Fig.4-16c and Fig.4-16d) are given as well. By using a QR code reader, such as a smart phone, one will be directed to our research group website (http://nanophotonicslab.eps.hw.ac.uk/). Please note that due to the off-axis design, another identical image exists in the reflected beam on the other side with respect to the surface normal.

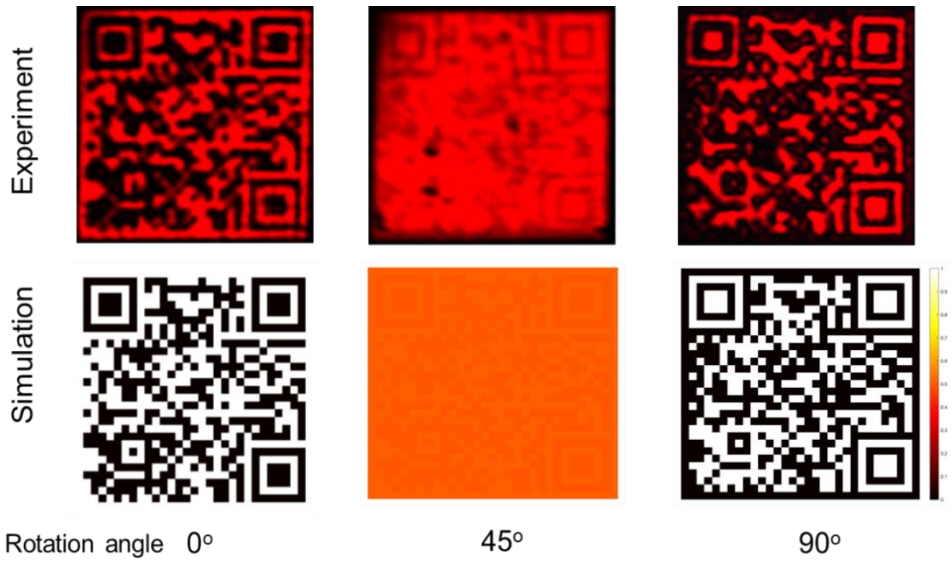


**Figure 4-17 The dependence of experimental results on the rotation angles of the transmission axis of the analyser away from the vertical direction[1].** The incident light is linearly polarized along the horizontal direction.

We further characterize the device by studying the relationship between the obtained QR code images and the transmission axis of the analyser. It is worth mentioning that the

transmission axes of the polarizer (before the sample) and the analyser (after the sample) are designed along the horizontal and vertical directions, respectively. Various QR codes are obtained by rotating the transmission axis of the analyser (designed along the vertical direction), while that of the polarizer is fixed along the horizontal direction. Interestingly, both the original and the complementary QR code work. Fig.4-17 shows the simulation and experimental results when the rotation angles of the analyser (away from the designed direction) are 0, $\pi/4$, and $\pi/2$, respectively. Interestingly, the two QR codes for the analyser with orthogonal directions of transmission axis (0 and $\pi/2$) are complementary images, i.e., the brightest area becomes the darkest area and vice versa. The hidden target QR code can hardly be observed when the rotation angle is $\pi/4$.

Further on, the dependence of experimental results on the incident polarization state is investigated. Although our design is based on the incident light with linear polarization, the experimental results for other polarization states are also obtained. Various polarization states are generated by controlling the angle between the transmission axis (fixed along the *x* direction) of a linear polarizer and the fast axis of a quarter waveplate. Fig.4-18 shows the simulation and experimental results for the incident light with linear polarization and elliptical polarization, respectively. Obviously, the image contrast is deteriorated when incident polarization state is away from the desired one (linear polarization). Furthermore, the generated QR code Fig.4-18 (b) doesn't work anymore due to the low image contrast.

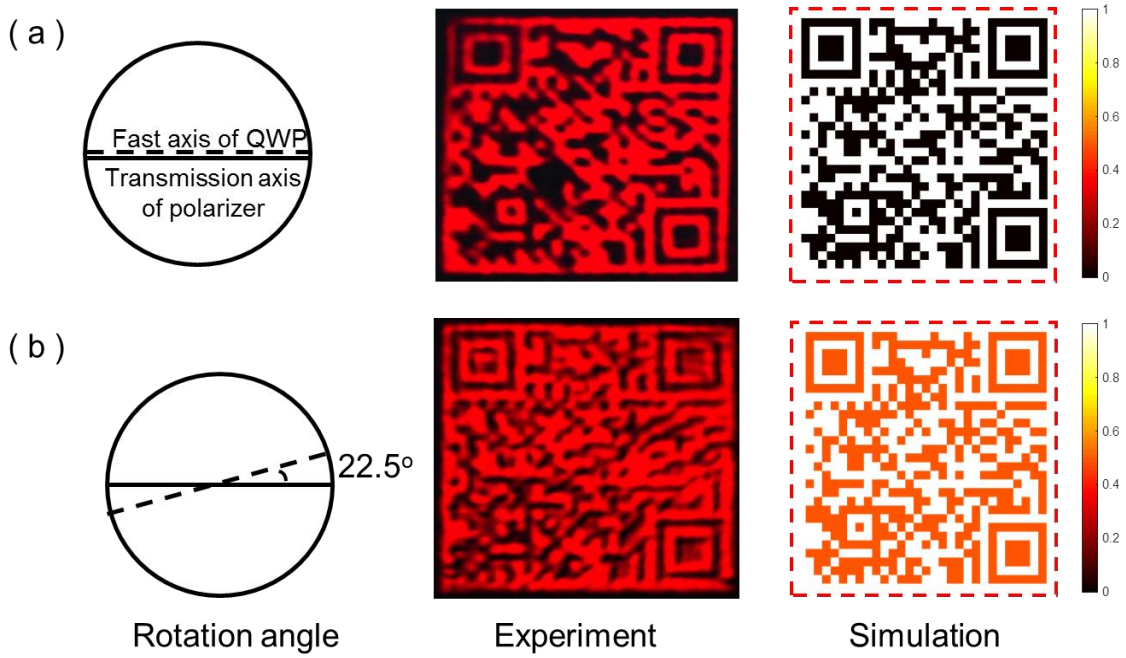

**Figure 4-18. The dependence of experimental results on polarization states of incident light[1].** The angles between the transmission axis (fixed along the horizontal direction) of a linear polarizer and the fast axis of the quarter waveplate (QWP) are 0 and 22.5 degrees, respectively.

From Eq.2-3 one can see that various polarization states can be generated by controlling the angle between the transmission axis (fixed along the *x* direction) of a linear polarizer and the fast axis of a quarter waveplate (QWP). Fig.4-19 shows the simulation results when the angle between the fast axis of the QWP and the transmission axis of the linear polarizer is changed. Obviously, the image contrast is deteriorated with the increase of this angle since the incident polarization state is away from the desired one (linear polarization).

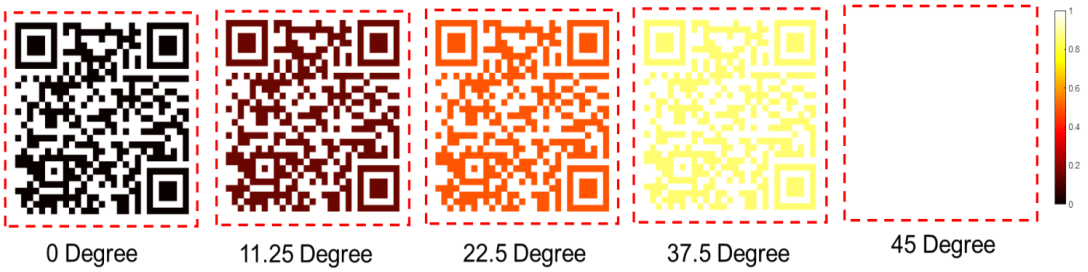


**Figure 4-19. Effect of the angle between the fast axis of the QWP and the transmission axis of the linear polarizer on the revealed QR code[1].**

To summarize, we experimentally demonstrate a metasurface device which can encode a QR code into the polarization profile of a laser beam. These hidden QR codes demonstrate the rich structure of a generated light beam by an optical metasurface that can possess at subwavelength scales.

### 4.5 Encoding a colour image into the laser beam through a dielectric metasurface

In the previous part of this chapter, we demonstrate how we successfully hide the grayscale and black-and-white image in the space-variant polarization profile of a laser beam through a reflective metasurface device. Not surprisingly, in order to further test the robustness of our approach, in this part a transmissive metasuface device is designed, fabricated and verified. The results show that a transmissive metasurface can be adopted so that a color image can be encoded in the polarization profile of a laser beam. Please note in this part I only briefly review this research work. For more detailed please refer to Ref.[3]. My contribution to this work includes the characterization of the fabricated metasurface devices and data analysis.

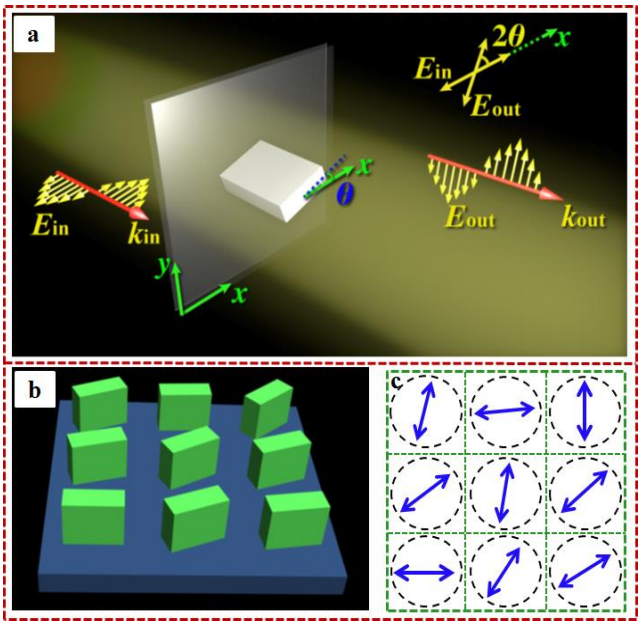


**Figure 4-20. Polarization rotation generated by the dielectric metasurface[3].** (a)The polarization of a linearly polarized light beam is rotated by $2\theta$ counterclockwise after passing through a nanoblock with in-plane orientation angle of $\theta$. (b) nine nanoblocks with different in-plane orientations on the metasurface can generate nine corresponding polarization states (c).

As stated in Chapter 2.2.2, dielectric metasurface which consists of amorphous silicon nanopillars with spatially variant orientations offers higher efficiency and better performance. For better understanding, we recapture the Fig.2-3 here as Fig.4-20. Based on the mechanism of linear polarization rotation (see Chapter 2.2.2), if there are various nanopillars with different in-plane orientations on the metasurface (see Fig. 4-20b)), a homogeneously incident light beam with linear polarization will be converted into an inhomogeneous polarization profile of the light beam, providing the desired polarization-rotating states for image encoding, as shown in Fig. 4-20c). Different from the grayscale image, hiding a color image into a laser beam needs more than one wavelength, or even the white light, which means that the above reflective system cannot be used here due to the dispersion of light. Instead the transmissive system is what we use below to carry out the color image hidden (see Fig. 4-21 and Fig.4-24).

To verify this approach and make it easier at the beginning, a vivid red-and-green image of a rose with 1200×1200 pixels is chosen as the target image. By optimizing the geometric parameters, e.g., dimension and orientation angle of each nanoblock, a light beam with wavelength-dependent polarization profile can be generated after it passes through the transmissive dielectric metasurface. The schematic of the design process is

shown in Fig.4-21b to Fig.4-21d. The SAM image of fabricated sample is given in Fig.4-22b.

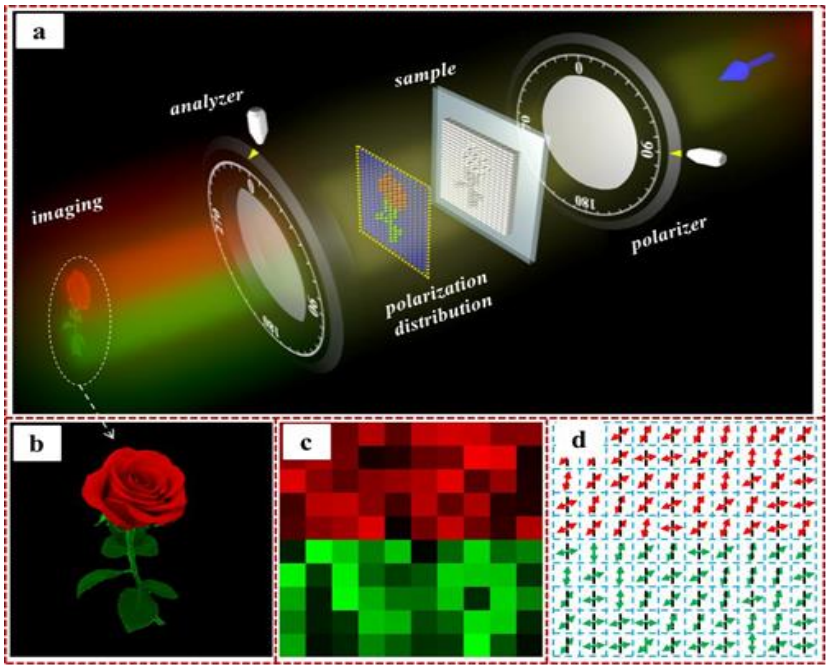


**Figure 4-21 Mechanism of polarization encoding and decoding[3].** (a) Schematic of the experimental setup. (b)The target image of a rose with green leaves. (c) Part of image with spatial distribution of brightness and color and (d) the corresponding desired polarization distribution. The green and red arrows represent the wavelength-dependent polarization states with different polarization orientations (red and green arrows for the wavelength at λ=665nm and λ=550nm, respectively).

To characterize the fabricated sample, a tunable supercontinuum laser source (NKT-SuperK EXTREME) is used as the light source for providing incident laser beam with two wavelengths of 550 nm and 660 nm. To be able to adjust the sample in all the directions, during the experiment the sample is mounted on a three-dimensional translational stage. This sample is fabricated in National Nano Science Centre of China, Beijing. A specific analyser is required in order to reveal color and brightness profiles of the image. An objective with a magnification 10× is placed just after the sample to expand the image for visualization with a charge-coupled device (CCD) camera.

The simulation and experimentally observed image for the incident light beam at the wavelength of 660 nm are presented in Fig. 4-23a and Fig. 4-23d, while when the wavelength of incident light is 550 nm, the results are given in Fig. 4-23b and Fig. 4-23e, with a slight discrepancy of the flower head part which may be caused by the fabrication errors. When these two wavelengths are together used as the incident light, a vivid rose

with red petals, green leaves, the stem and even the veins on the leaves can be observed, as shown in Fig. 4-23f, which agree well with the simulation result in Fig. 4-23c.

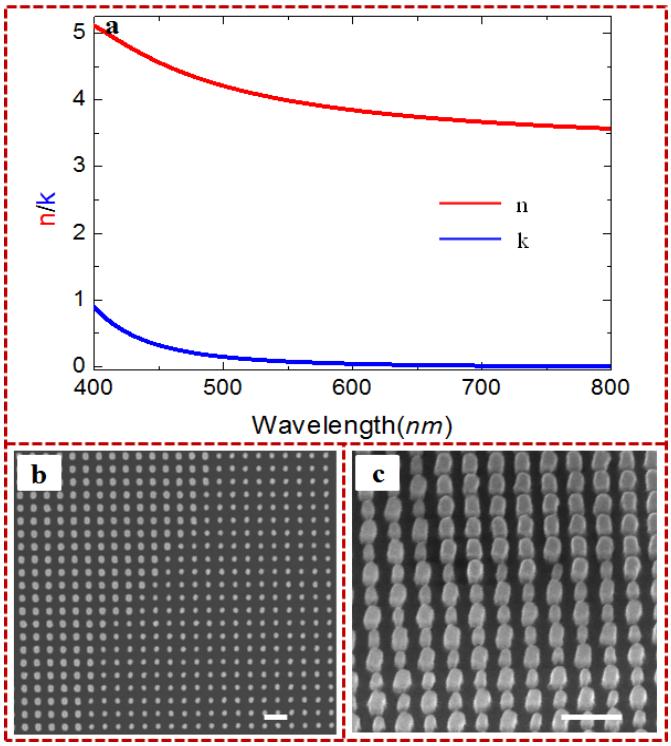


**Figure 4-22. The refractive index of the amorphous silicon film with the thickness of 310 nm and the SEM images of the fabricated samples[3].** (a) Red and blue curves represent the real and imaginary parts of the refractive index, respectively. (b) SEM image of the flower sample. (c) SEM image of the fruit sample with a tilt angle. The scale bar in (b) and (c) is 500 nm.

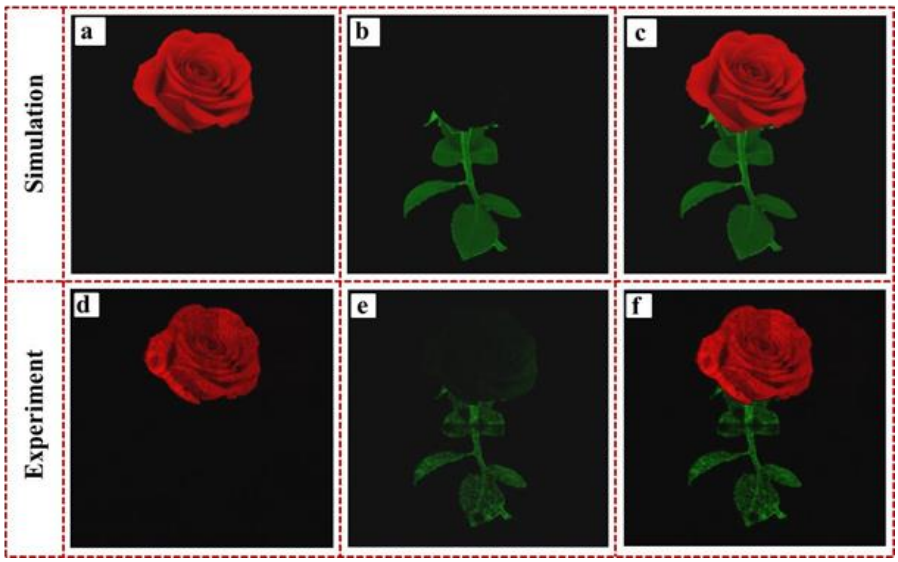


**Figure 4-23 Simulation and experimental results of the polarization encoded image of rose[3].** The experimentally revealed color image when the wavelength of the incident light is (d) λ=660 nm; (e) λ=550 nm; and (f) λ=660 nm and 550 nm. (a)-(c) are the corresponding simulation results.

Encouraged by the good results of rose image, a dielectric metasurface device is then designed which can generate additive color mixing, which means that a color image to be encoded in the laser beam. Red, green and blue are three primary colors for the common additive color mixing. The designed metasurface consists of supercells, and one of them is shown in the illustration schematic in Fig.4-24a. There are four nanoblocks of two different types which distributed diagonally in each supercell of the fabricated sample. To better understand the mechanism of this design, each supercell here can be treated as one pixel, and each pair of nanopillars in the supercell will respond to a specific wavelength if a light beam containing red and green color shines on the surface. Therefore, by customizing the in-plane orientations of these nanoblocks in a supercell, arbitrary combinations of polarization states (double-headed arrows in Fig.4-24b) for two colors of red and green can be generated. Since these two colors are polarization-dependent, an arbitrary additive color (e.g., a pixel with orange in Fig.4-24c) can then be generated by using an analyser which modulates the ratio between the transmitted intensity of these two colors, according to the Malus' Law (see Chap. 4.2). Thus, a multicolor image can be embedded into the polarization topology of a modulated light beam. In the design, the transmission axis of the analyser after the metasurface device is fixed at the direction perpendicular to which of the linear polarizer before the metasurface device, for the generation of the incident light beams.

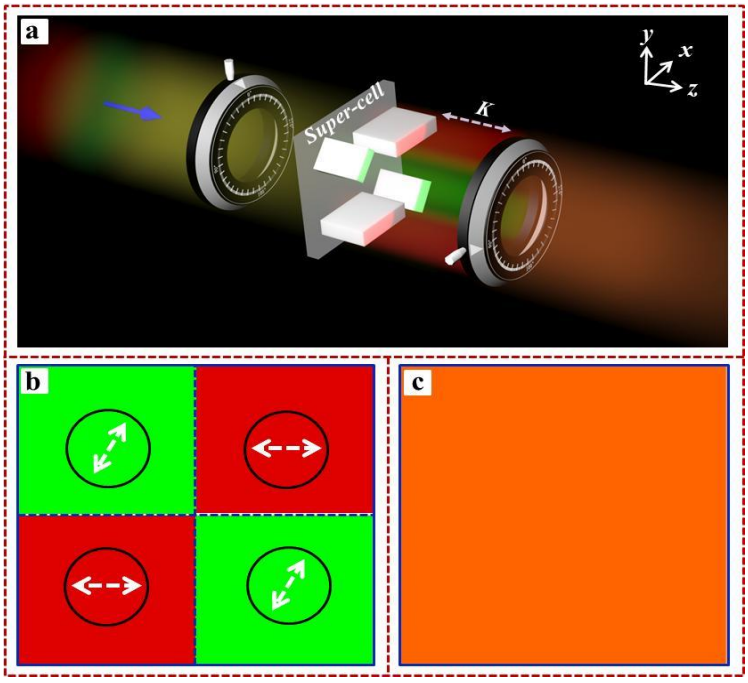


**Figure 4-24 Mechanism of additive color mixing in one supercell [3].** (**a**) A vertically polarized light beam containing red and green colors impinges on a supercell which consists four nanoblocks of two types which is distributed diagonally. Here the transmission axis of the analyser is perpendicular to that of the

linear polarizer for the generation of incident light with linear polarization. (**b**) The polarization distribution (arrows in each sub cell) of the transmitted light beam after the incident light passing through the supercell. (**c**) A new color is generated based on the polarization states for red and green colors in (**b**).

Fig.4-25 shows the simulation and experimentally observed images when the incident light is linearly polarized red light, green light and both at the same time. At the wavelength of 660 nm, 550 nm and the combination of these two wavelengths, a very good agreement between simulation and experimental results is found. When the incident light contains the combination of 550 nm and 660 nm, a high-resolution multicolor image is revealed which contains eight different types of fruits (see Fig.4-25f). Apart from the original colors of red and green which are used in the design, yellow, orange and dark red are also observed which demonstrates the color mixing ability of the method explained above.

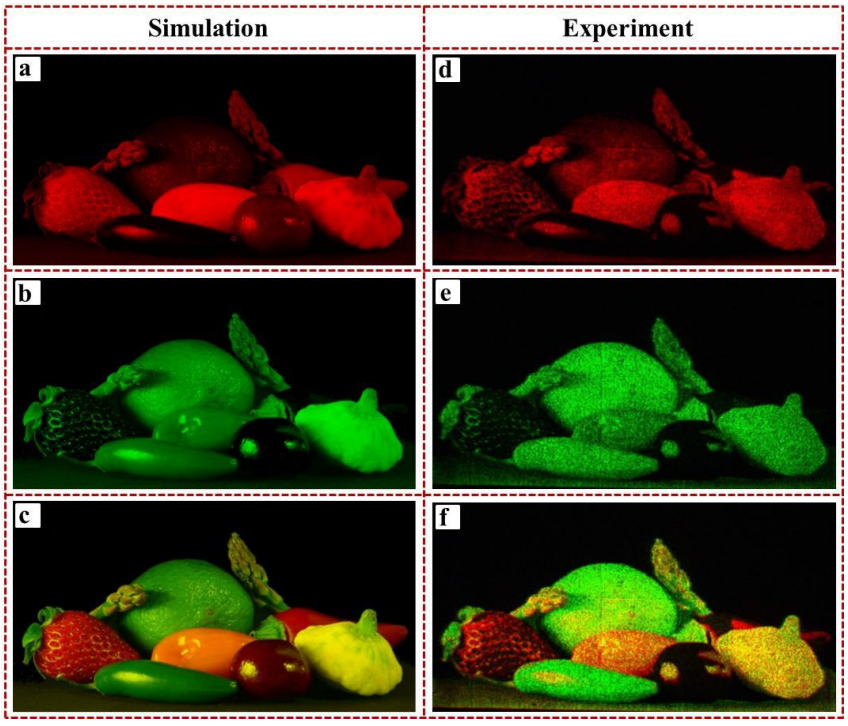


**Figure 4-25. Simulation and experimental results of the full-color-like image[3].** The left column is simulation and the right is the image obtained in the experiment. (**a**) and (**d**) are the simulation and experimentally observed images when the wavelength of incident light is λ=660nm, while (**b**) and (**e**) are the cases with the green(λ=550nm) light illumination. (**c**) and (f) are the results when both red and green light are used together.

It is worth to mention that one of the advantages of this approach is the developed metasurface device works under the white continuum light, as shown in Fig.4-26b, c for the rose and fruit plate sample, respectively. For this purpose, two metasurface consisting of uniform array of nanoblocks are fabricated, and the Dolan-Jenner MI-150 Fiber Optic

Illuminator is used as the source of the white continuum light.

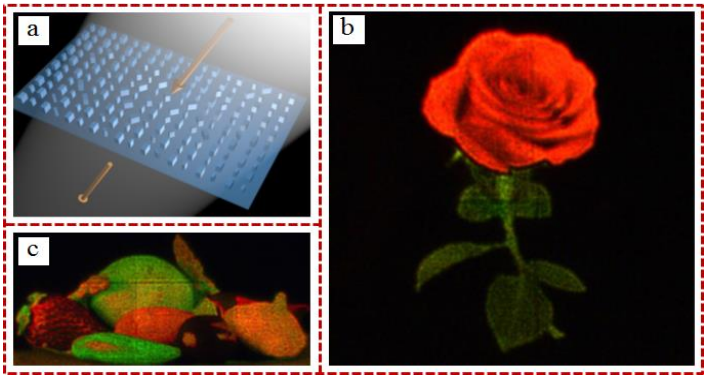


**Figure 4-26 Designed sample and experimental results when white continuum light is illuminated on the samples [3].** (a) Schematic of optical measurement under the illumination of white continuum light. (b) and (c) are the measured results for rose and fruit samples, respectively.

Fig.4-27a and Fig.4-27b show the theoretical conversion efficiency and diffraction efficiency of the designed nanoblocks with two different geometrical structures (red, green). The resonant wavelength of each silicon nanoblock is dependent on its length (Lx) and width (Ly). As a showcase, here two examples of nanoblock with different lateral dimension and same thickness (h=310 nm) are given. For Lx=100 nm (150 nm), Ly=75 nm (105 nm), the simulated conversion efficiency is over 60% (90%) with a wavelength range from 535 nm (630 nm) to 560 nm (670 nm), while the diffraction efficiency is over 23% (40%) (See Figs. 4-27a and 4-27b). To perform optical measurement, we fabricated two metasurfaces with nanoblocks of uniform orientations. The experimental results for the red and green color are shown in Fig. 4-27c and 4-27d, respectively. The experimental conversion efficiency is more than 70% (70%) for wavelength range of 560 nm (670 nm) to 578 nm (695 nm), which shows the high polarization purity (conversion efficiency) of the light. In comparison with the simulation results, the red shift of response wavelength is mainly to the fabrication error, in which the lateral size of fabricated nanoblocks are larger than the designed ones.

To summarize this part, the spatial-variant and wavelength-selective polarization profile can be encoded into a dielectric metasurface is experimentally demonstrated. Upon this high-resolution color image can be hidden into, and revealed later from a structured beam. The dielectric metasurface provides an extraordinary capability in additive color mixing and tailoring the polarization of light at the nanoscale. Another advantage is that the developed metasurface device can work when the white continuum light shines on it.

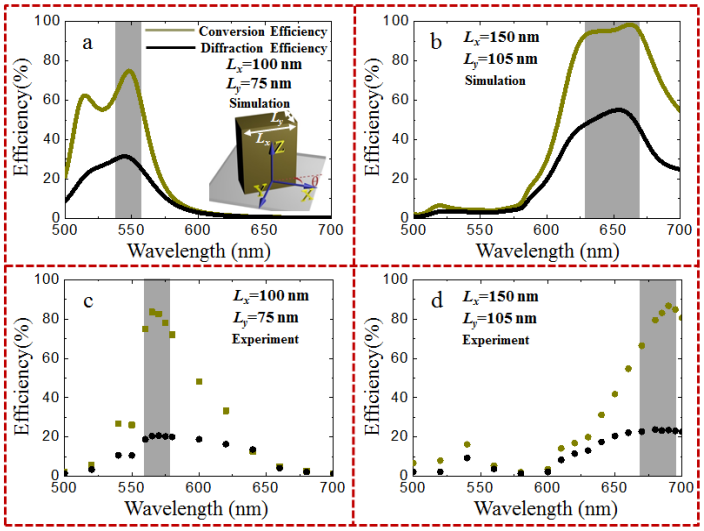


**Figure 4-27. Conversion efficiency (dark yellow line/dot) and diffraction efficiency (black line/dot) for the nanoblocks with two different geometrical structures**: (a) and (c) with $L_x$=100 nm, $L_y$=75 nm; (b) and (d) with $L_x$=150 nm, $L_y$=105 nm. The first and second rows are the simulation and experimental results, respectively. Inset is the simulation model [3].

## 4.6 Summary

In this chapter, we demonstrated how metasurfaces can be used to manipulate polarization state of light through a metasurface device. Either the wavelength-selective, spatial-variant or both of them can be encoded into the polarization profile of a laser beam by using only one single metasurface device. To realize this function, a couple of linear polarizer and analyser are placed before and after the metasurface device. In all three demonstrations, the transmission axis of the polarizer and analyser are perpendicular to each other. Also, please note that our approach is not hologram (or color hologram) because the image is directly hidden into the polarization profile of the light beam passing through it, while the hologram is based on the phase or wavefront manipulation. We believe that this approach of color tuning and polarization manipulation can be applied in information security, data storage and other diverse areas in the near future.

## 4.7 References


1. Zhang, C., et al., *Optical Metasurface Generated Vector Beam for Anticounterfeiting.* Physical Review Applied, 2018. **10**(3): p. 034028.

2. Yue, F., et al., *High-resolution grayscale image hidden in a laser beam.* Light: Science & Applications, 2018. **7**(1): p. 17129.

3. Zang, X., et al., *Polarization Encoded Color Image Embedded in a Dielectric Metasurface.* Advanced Materials, 2018. **30**(21): p. 1707499.

4. Zheng, G., et al., *Metasurface holograms reaching 80% efficiency.* Nature nanotechnology, 2015. **10**(4): p. 308.

5. Wang, L., et al., *Grayscale transparent metasurface holograms.* Optica, 2016. **3**(12): p. 1504-1505.

6. Chanana, A., et al., *Hiding multi-level multi-color images in terahertz metasurfaces.* Optica, 2016. **3**(12): p. 1466-1470.

7. Born, M. and E. Wolf, *Principles of optics: electromagnetic theory of propagation, interference and diffraction of light*. 2013: Elsevier.

8. Hu, D., et al., *Ultrathin terahertz planar elements.* Advanced Optical Materials, 2013. **1**(2): p. 186-191.

9. Wang, L., et al., *Active display and encoding by integrated plasmonic polarizer on light-emitting-diode.* Scientific reports, 2013. **3**: p. 2603.

10. Yue, F., et al., *Multichannel Polarization-Controllable Superpositions of Orbital Angular Momentum States.* Advanced Materials, 2017. **29**(15): p. 1603838.

11. Yu, N., et al., *Light Propagation with Phase Discontinuities: Generalized Laws of Reflection and Refraction.* Science (Washington), 2011. **334**(6054): p. 333-337.

12. Huang, L., et al., *Dispersionless phase discontinuities for controlling light propagation.* Nano letters, 2012. **12**(11): p. 5750-5755.

# Chapter 5 Simultaneous control of phase and polarization

Multifunctional devices based on pure phase or polarization manipulation were discussed in Chapter three and Chapter four, respectively. In this chapter, we are going to concentrate on the multichannel, multifunctional metasurface device based on simultaneous control of phase and polarization profiles of light beams, which will be experimentally realized by using dielectric metasurface devices with spatially variant orientations. Instead of the reflection type metasurface, the transmission type metasurface was used in this demonstration.

## 5.1 Introduction

Optical metasurfaces are two-dimensional counterparts of metamaterials, which can tailor light's amplitude, phase and polarization at subwavelength resolution, enabling compact optical devices that can outperform conventional bulky components [1-3]. In the last several years, the broad appeal of this emerging technology has been focused on new discovery, performance improvement, device miniaturization, system integration, and new functionalities. Rapid advances in metasurfaces have brought new design methodology, enabling the development of flat-optics devices for various applications, ranging from metalenses [3-5], holograms [6-9], cloaking [10] and orbital angular momentum manipulation [11-12] to nonlinear optics [13].

To meet the growing requirement of device miniaturization and system integration, new design approach based on metasurface has been proposed to develop ultrathin optical devices that integrates multiple functionalities into one single device while preserving their independent functionalities. The unprecedented capability of metasurface in the light propagation provides a compact and flexible platform to realize various types of metasurface devices with multiple functionalities, including helicity multiplexed hologram [8], integration of multiple polarization manipulation channels [14], polarization beam splitters [15], and multifunctional light sword lens [16]. As two fundamental properties of light, the spatial distribution of polarization and phase can be used to record, process and store information. For example, a high-resolution image can be hidden in the polarization profile of a light beam [17]. How to realize a multichannel device that can realize image-switchable hologram and non-uniform polarization profile for image encryption in different channels has not been reported. By integrating different functionalities (polarization-sensitive holograms and arbitrary polarization manipulation)

onto the same metasurface device, a highly versatile ultra-compact multichannel device with minimal spatial footprint can be achieved. Due to the independent control of phase and polarization based on the geometric phase, such a device is also capable of realizing dynamic change of the holographic images and hiding a grayscale image.

## 5.2 Results

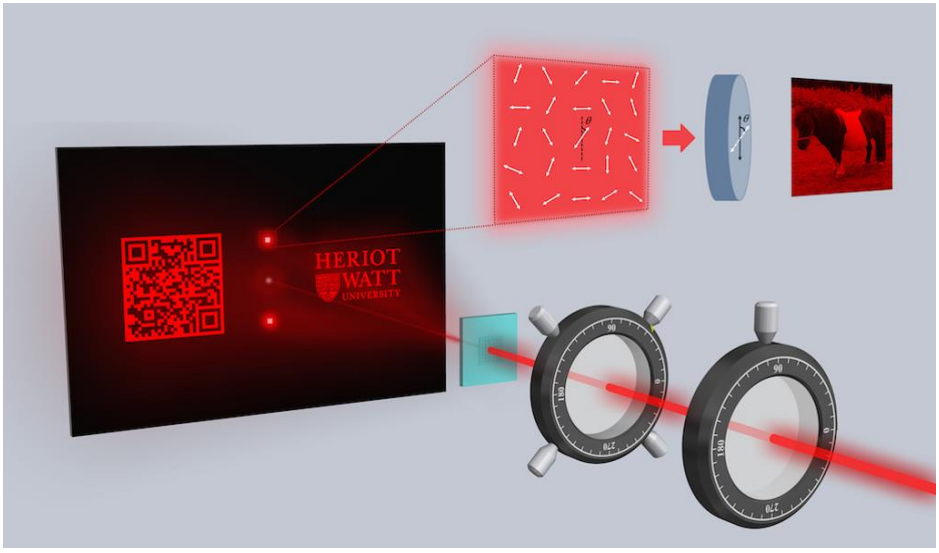


**Figure 5-1 Schematic of the multichannel metadevice with different functionalities.** A metasurface device can realize an image-switchable hologram and arbitrary polarization manipulation for a hidden image. The two holographic images are switchable, depending on the helicty of the incident light. The polarization files of the laser beams along the vertical direction are used to encode a grayscale image, which can be revealed by passing through a polarizer.

Fig.5-1 shows a schematic illustration of our proposed multichannel device. Two different functionalities are realized, depending on the polarization state of the incident light. Two holographic images (QR code and logo of Heriot-Watt University) along two symmetrically distributed horizontal channels can be reconstructed by controlling the helicity of the incident light. Upon the illumination of a linearly polarized light beam, a grayscale image of a miniature horse is encoded in the polarization profile of a light beam in the two vertical channels and revealed by a rotating polarizer (analyser). Fig. 5-2a shows the design parameters of the projected holographic images along the horizontal direction and the arbitrary polarization manipulation along the vertical direction. The full off-axis angle $\beta_1$, $\beta_2$ and $\beta_3$ are designed to be 65.7°, 19.0° and 17.6°, respectively. The projection angles of QR code and University logo are 23.4°×23.4° and 23.3°×14.4°, respectively.

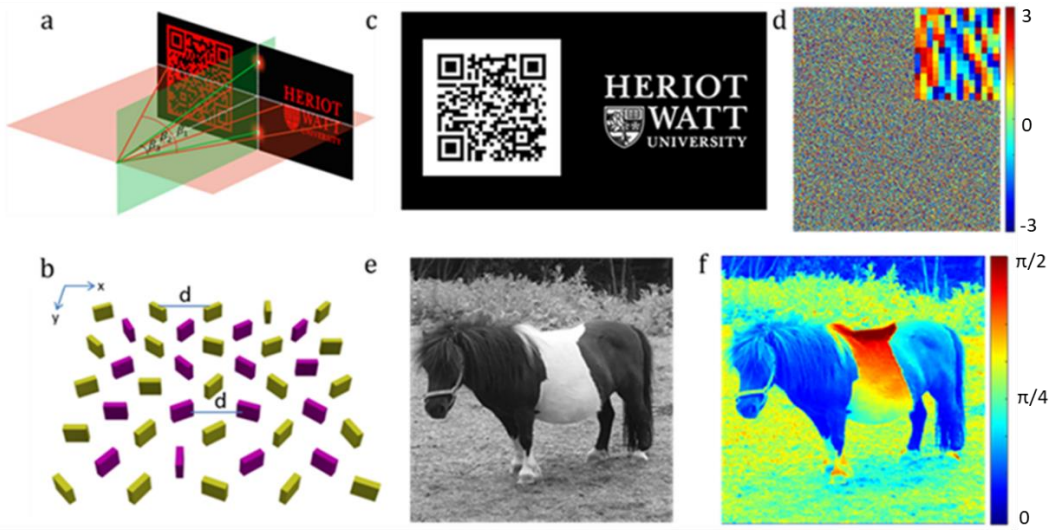


**Figure 5-2 Design and simulation.** (a) Geometric parameters of the projected images and the off-axis vector beams for image encryption. The full angle $\beta_1$, $\beta_2$ and $\beta_3$ are designed to be 65.7°, 19.0° and 17.6°, respectively. The full off-axis angle $\beta_1$, $\beta_2$ and $\beta_3$ are designed to be 65.7°, 19.0° and 17.6°, respectively. The projection angles of QR code and University logo are 23.4°×23.4° and 23.3°×14.4°, respectively. (b) Two metasurfaces represented by gold and purple colors are merged together with a displacement vector of (d/2, d/2). d is the distance between neighboring antennas with a value of 424 nm. The size of the sample is the same and the equivalent pixel size is 300 nm× 300 nm. (c)The target holographic image and (d) the calculated phase profile based on Gerchberg−Saxton algorithm. The inset in (d) shows the phase distribution in the central area with high magnification. There are 16 phase levels (- π to π with the interval of π/8) that are used in the design. (e) Target object for image encryption and (f) the required distribution of polarization direction for linearly polarized light.

To realize different functionalities in multiple channels, metasurfaces for pure phase control [8] or simultaneous control of phase and polarization [14, 15] have been employed. In comparison with phase control, simultaneous control of phase and polarization is more challenging for nanofabrication due to the precise control of the feature size. Instead of using dielectric nanopillars with various feature sizes, a combined metasurface consisting of nanopillars with same feature size (e.g., height, length, width) and spatially variant orientations are used to facilitate the fabrication process. Two metasurfaces (one for the holographic image along the horizontal direction and one for arbitrary polarization manipulation along vertical direction) are designed and merged together with a displacement vector of (*d*/2, *d*/2), as detailed in Fig.5-2b. Where *d* is the distance between neighboring nanopillars with a value of 424 nm along both *x* and *y* directions. Each dielectric nanopillar in the dielectric metasurface functions as a half waveplate, which can generate the required independent phase profile for the designed hologram and the polarization profile for the hidden image based on Malus' Law. The sample size before and after metasurface merging is the same and the equivalent pixel

size in the merged metasurface is 300 nm×300 nm ($d/\sqrt{2}$). The resonant wavelength of each nanopillar is dependent on its feature size such as length ($L_x$) and width ($L_y$), which are used for the efficiency optimisation. The thickness $h$ of metasurface is 310 nm ($\frac{2\pi}{\lambda} \cdot h \cdot \Delta n = \pi$) along $z$ direction. By rotating the fast axes of half-wave plates with their orientations according to a function θ (x, y), a circularly polarized light beam can be fully transformed to a beam with opposite helicity and a geometric phase (known as Pancharatnam–Berry phase) equal to ±2φ($x$, $y$), where $\varphi$ is the orientation angle of each nanorod. "+" and "-" represent the sign of the phase change for the incident RCP light and that for the incident LCP light, respectively. Hence the reversion of the phase profile can be achieved by changing the helicity of the circularly polarized light. By controlling the local orientations of nanopillars between 0 and π, a phase profile that can cover the full 0-2π range while maintaining the equal transmission amplitude pickups can be achieved.

The Gerchberg−Saxton algorithm is used to calculate the phase profile of the hologram via a propagating function, which can reconstruct two off-axis images on the different sides of the incident light. The phase profile is pre-compensated in order to avoid image distortion because the final projected image has a large field of view of 65.7°×23.4°. The target image includes a QR code and a University logo of Heriot-Watt University (see Fig.5-2c). Fig.5-2d shows the calculated phase distribution and the inset shows the phase distribution in the central area with a higher magnification. To realize arbitrary polarization manipulation, a grayscale image (miniature horse) with 1125×1125 pixels is selected as a target image for polarization encoding (Fig.5-2e). Each pixel is 424 nm along two perpendicular directions. The Malus' Law tells us that the intensity of the light transmitted by an analyser is directly proportional to the square of the cosine of angle between the transmission axes of the analyser and the polarizer. In our experiment, the transmission axes of the polarizer and the analyser are set along the x axis and y axis, respectively. The calculated polarization angle distribution of linearly polarized light is shown in Fig. 5-2f. To realize off-axis configuration, an additional phase gradient profile is added. For this metasurface, the additional phase difference between neighboring pixels to along x direction is $\pi/5$, where the corresponding off-axis angle is $8.8^o$. The required phase profile for the hologram and polarization profile for the hidden images are realized by controlling the orientation angles of nanopillars. The scanning electron microscope (SEM) image of part of fabricated sample is shown in Fig.5-3a.

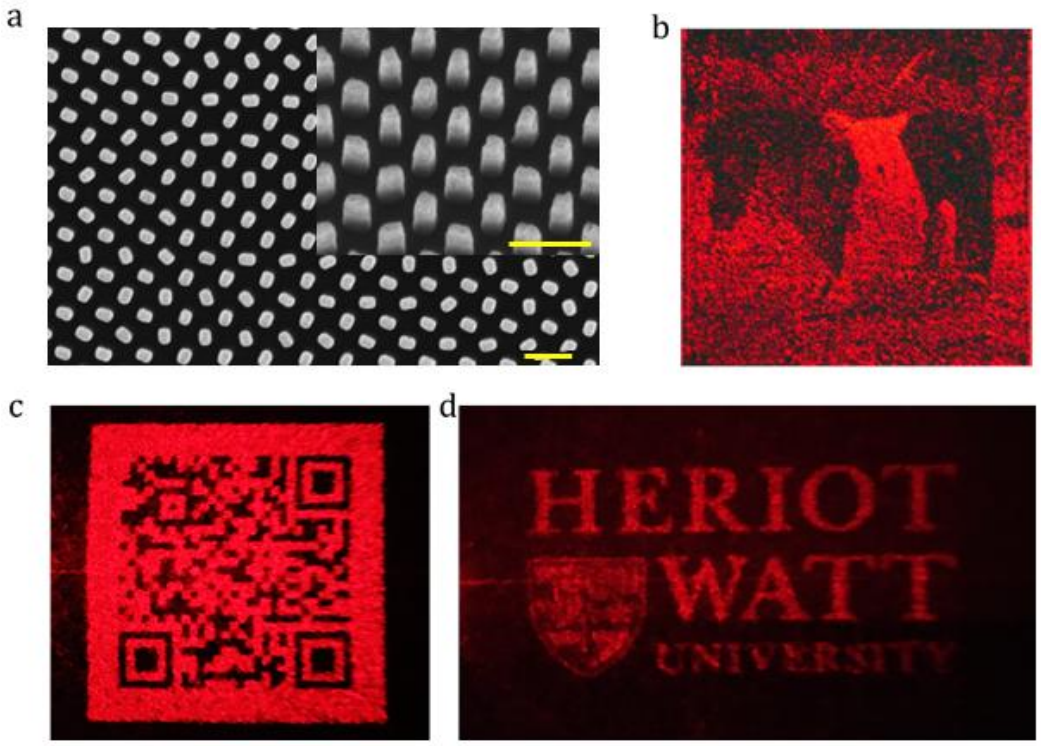


**Figure 5-3. Scanning electron microscope (SEM) of the fabricated device and experimental results.** (a) SEM image of the fabricated sample. The scale bar is 500 nm. (b) The revealed hidden image in the polarization profile of the light beam. The reconstructed holographic images consist of (c) a QR code and (d) a University logo upon the illumination of LCP light.

For the fabrication process of the metasurface device, quartz substrates are used to fabricate the designed silicon nanoblocks. First, an amorphous silicon film with a thickness of 310 nm is deposited on the quartz substrate by using an Inductively Coupled Plasma Enhanced Chemical Vapor Deposition System (ICPECVD, Sentech SI 500D). Then, an electron beam evaporator is used to deposit an aluminum film with a thickness of 50 nm, which is used as a charge-dissipation layer and hard mask for etching. The positive electron beam resist (ZEP-520A) with a thickness of 200 nm is spin coated on the sample. After that, nanostructures are defined on the resist film based on the standard electron-beam lithography (EBL, Vistec EBPG 5000+). The nanopatterns are transferred into the aluminum layer and silicon layer by subsequent etching using an Inductively Coupled Plasma etcher (ICP, Sentech PTSA SI 500). Finally, the silicon nanoblocks are obtained on the quartz substrate by removing the aluminum layer with aluminum etchant. To characterize the fabricated sample, a tunable supercontinuum laser source (NKT-SuperK EXTREME) provide a laser beam with a wavelength of 650 nm, whose polarization state is controlled by a polarizer and a quarter-wave plate (QWP). The laser beam impinges on the metasurface device, which is mounted on a 2D translational stage, allowing for the adjustment of sample position. The transmitted holographic images are

projected to a screen in the far field for the inspection of the image quality. A normal camera is used to capture images on the image screen. Upon the illumination of LCP light, the fabricated device can reconstruct the 'QR code' on the left and the 'University logo' on the right side of the metasurface, respectively (Fig. 5-4(a)). By scanning the QR code with a smart phone, one can access our group website (http://nanophotonicslab.eps.hw.ac.uk/). Although the two bright laser beams along the vertical direction can be seen clearly, their detailed information (e.g., intensity, polarization) cannot be directly measured due to the smaller beam size. In order to evaluate the generated polarization profile for the hidden image, the metasurface is rotated by 90 degrees so that the two vector beams can be easily characterized in horizontal direction. An objective with magnification of 10× is adopted to expand the image so that the image can be visualized on charge-coupled device (CCD) camera. An analyser with a transmission axis along x-axis is used to reveal the encoded grayscale image. No image is obtained without the analyser due to the uniform intensity distribution. The hidden image is decoded with the analyser when its transmission axis is along the vertical direction.

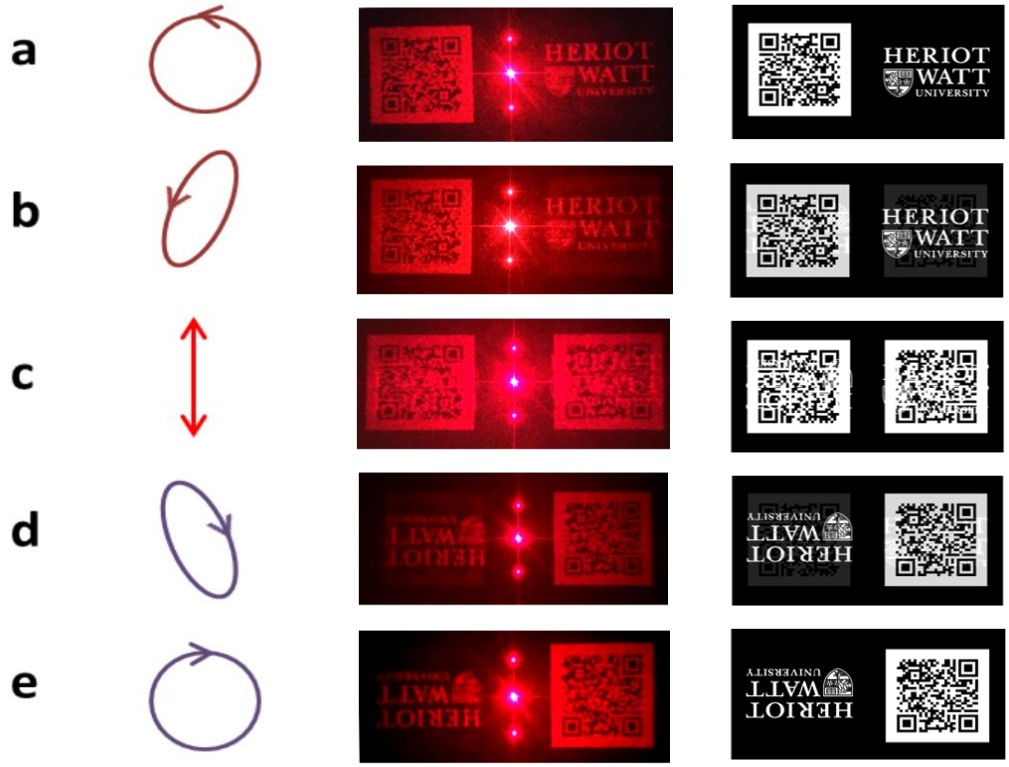


**Figure 5-4 Experimental results and simulation results of holographic images versus the polarization states of the incident light at 650 nm.** The polarization states of the incident light are chosen to be (a) LCP, (b) left-handed elliptically polarized, (c) linearly polarized, (d) right-handed elliptically polarized and (e) RCP. The figures in the middle column and right column represent the experimental results and the corresponding simulation results, respectively.

Fig.5-4 shows the experimental and simulation results upon the illumination of incident light with various polarization states. Two separate holographic images (see Fig. 5-4a and Fig.5-4e) are observed when the device is illuminated by a circularly polarized light beam (RCP or LCP). The holographic images will overlap when a light beam with elliptical polarization impinges on the device since any polarized light beam can be decomposed into two beams with opposite circular polarization states. The rise and fall of intensities of two overlapping images is determined by the ellipticity of polarized light, which is controlled by the angle between the fast axis of the quarter wave plate and the transmission axis of the polarizer. The intensities of two overlapping images are the same (see Fig. 5-4c) for the linearly polarized light since it contains a LCP light beam and a RCP light beam with same components. The intensity of the 'QR code' dominates (see Fig. 5-4d) for the right-handed elliptically polarized light. Finally, two separate images are obtained again but they are swapped and upside down (see Fig. 5-4e) compared to those in Fig. 5-4a. Good agreement is seen between the experimental measurements and the simulation results.

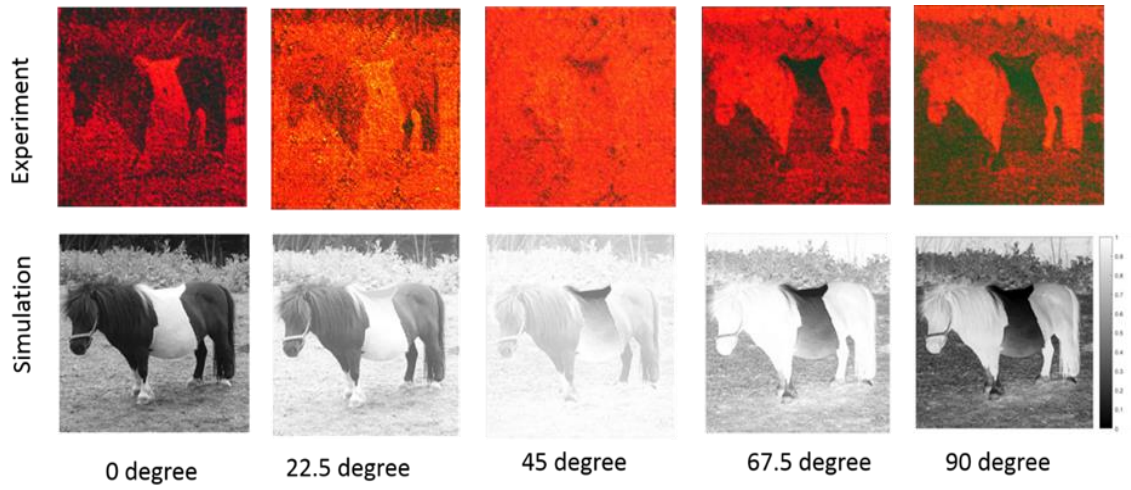


**Figure 5-5 The dependence of experimental results on the rotation angles of the transmission axis of the analyser away from the vertical direction.** The incident light is linearly polarized along the horizontal direction.

We further evaluate the second functionality of the developed device – arbitrary polarization profile for the image encryption. It is worth mentioning that the transmission axes of the polarizer and the analyser are along horizontal and vertical directions, respectively. A plane wave with uniform intensity is used for the simulation, whereas a collimated laser beam with Gaussian profile is used in the experiment. The dependence of simulation and experimental results on the direction of transmission axis of the analyser are provided in Fig.5-5, indicating that the transmission axis of the analyser plays an

important role in the decryption process. The two images for the analyser with orthogonal directions of transmission axis ($0^o$ and $90^o$) are complementary grayscale images, i.e., the brightest area becomes the darkest area and vice versa. Under the illumination of the incident light with various polarization states, the numerically calculated and experimentally observed images are provided in Fig.5-6. Despite the fact that the metadevice can work for the elliptical polarization, the image quality is deteriorated.

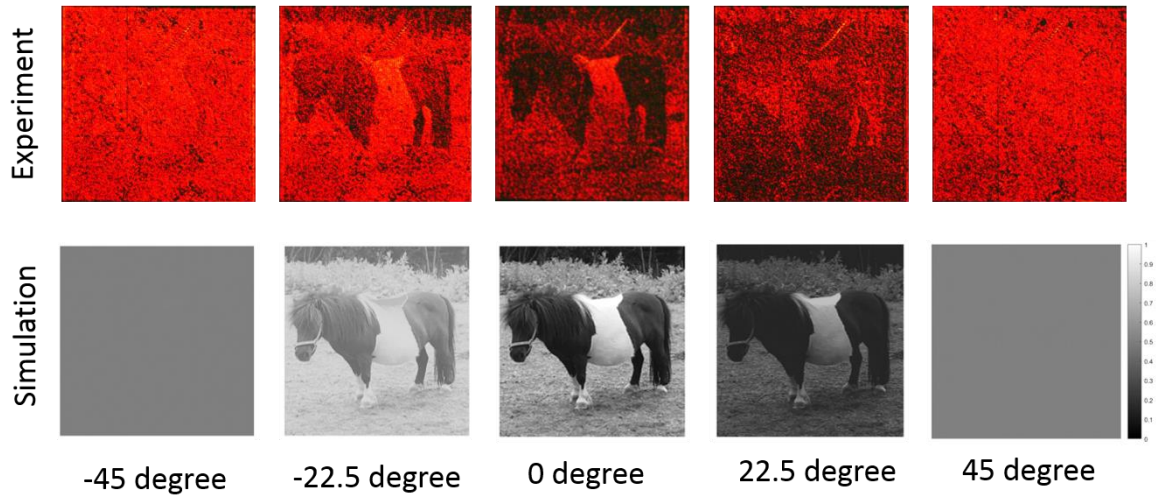


**Figure 5-6 The dependence of experimental results on polarization states of incident light.** The angles between the transmission axis of a linear polarizer (fixed along the horizontal direction) and the fast axis of the quarter waveplate (QWP) are set at -45, -22.5, 0, 22.5 and 45 degrees, respectively.

### 5.3 Discussion

The uniqueness of this multichannel device is the integration of totally different functionalities on the single device by the independent control of the phase and polarization profiles. Although it can be realized based on the precise control of feature sizes for the simultaneous control of phase and polarization, which is more challenging for nanofabrication, the metasurface consisting of nanopillars with same feature size can facilitate fabrication. Holography is one of the most attractive approaches for reconstructing optical images. As the largest part of the hologram market, security holograms have been used widely in our daily lives (e.g., passports, credit cards, quality products). However, despite tremendous advances in the fundamental principles of optical holography, traditional security holograms are not secure any more since they can be easily forged. Industry is always looking for holograms with unique properties which are not easy to design and copy. In this work, the reconstructed holographic image is dependent on the polarisation state of the incident light, while the hidden image is embedded in the inhomogeneous polarization distribution of the generated laser beam and

can be revealed by using a linear polarizer. The invention of this brand new device will possess a unique advantage over traditional security holograms due to the combination of image-switchable functionality and the hidden image in the laser beam. The holographic images are intensity patterns that can be observed with naked eyes, while an analyser is necessary for the acquisition of the hidden image's intensity profile since the spatially-varying polarization profile of the modulated light beam has a uniform intensity profile. In the terms of fabrication, the proposed hologram is much more tolerant to fabrication errors such as misalignment and etch-depth deviation since geometric phase concept that can provide a continuous phase profile with only a single lithography step.

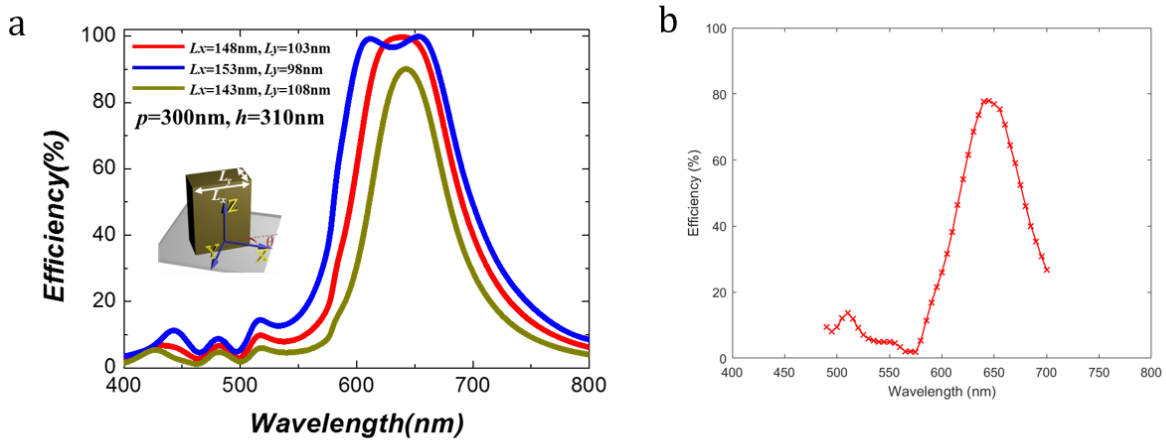


**Figure 5-7. Simulation and experimental measurement of the conversion efficiency.** (a) Simulated results. (b) Experimental measurement.

The conversion efficiency is defined as the ratio between the optical power with desired polarization rotation and the transmitted power. To perform optical measurement of the conversion efficiency, a metasurface consisting of nanopillars with uniform orientations is fabricated. The simulated and experimental conversion efficiency are shown in Fig.5-7. For the design parameters in Fig.5-7a, the resonance peak is localized at around λ=650 nm with a conversion efficiency over 90%. In our design, the target geometric parameters are $L_x$=150 nm and $L_y$=105 nm. In addition to the ultrathin nature and compactness, this multifunctional metadevice can provide entirely new functions that are very challenging or impossible to achieve with traditional optical components even with highest quality.

## 5.4 Conclusion

Optical metasurfaces are capable of generating optical fields with inhomogeneous spatial distribution in terms of phase and polarization, providing a powerful tool to develop multichannel devices with unusual functionalities. We experimentally demonstrate a

metasurface device that can realize image-switchable hologram and spatial polarization manipulation in different channels. The metadevice consists of amorphous silicon nanopillars with same geometry and spatially variant orientations. The feasibility study of the multichannel device based on the independent control of phase and polarization renders this technique very attractive for compact optical devices with high density of functionalities.

### 5.5 References


1. N. F. Yu, P. Genevet, M. A. Kats, F. Aieta, J. P. Tetienne, F. Capasso, Z. Gaburro. Science 2011, 334, 333;

2. X. Ni, N. K. Emani, A. V. Kildishev, A. Boltasseva, V. M. Shalaev. Science 2012, 335, 427;

3. X. Chen, L. Huang, H. Mühlenbernd, G. Li, B. Bai, Q. Tan, G. Jin, C. Qiu, S. Zhang, T. Zentgraf. Nat. Commun. 2012, 3, 1198;

4. J. Lin, M. J. P. B. Mueller, Q. Wang, G. Yuan, N. Antoniou, X. Yuan, F. Capasso. Science 2013, 340, 331.

5. M. Khorasaninejad, W. T. Chen, R. C. Devlin, J. Oh, A. Y. Zhu, F. Capasso, Science 2016, 352, 1190.

6. L. Huang, X. Chen, H. Mühlenbernd, H. Zhang, S. Chen, B. Bai, Q. Tan, G. Jin, K. Cheeah, C. Qiu, J. Li, T. Zentgraf. S. Zhang. Nat. Commun. 2013, 4, 2808;

7. G. Zheng, H. Mühlenbernd, M. Kenney, G. Li, T. Zentgraf, S. Zhang. Nat Nanotechnol. 2015, 10, 308;

8. D. Wen, D. F. Yue, G. Li, G. Zheng, K. Chan, S. Chen, M. Chen, K. F. Li, P. W. H. Wong, K. W. Cheah, E. Y. B. Pun, S. Zhang, X. Chen. Nat. Commun. 2015, 6, 8241;

9. W. T. Chen, K. Y. Yang, C. M. Wang, Y. W. Huang, G. Sun, I. Chiang, C. Y. Liao, W. L. Hsu, H. T. Lin, S. L. Sun, L. Zhou, A. Q. Liu, D. P. Tsai. Nano. Lett. 2014, 14, 225;

10. Yin, X.; Ye, Z.; Rho, J.; Wang, Y.; Zhang, X. Photonic spin Hall effect at metasurfaces. Science 2013, 339, 1405-1407.

11. Yue, F.; Wen, D.; Zhang, C.; Gerardot, B. D.; Wang, W.; Zhang, S.; Chen, X.; Multichannel Polarization-Controllable Superpositions of Orbital Angular Momentum States. Adv. Mater. 2017, 29, 1603838.

12. Y. Chen, X. Yang, and J. Gao, "Spin-selective second-harmonic vortex beam generation with Babinet-inverted plasmonic metasurfaces," Adv. Opt. Mater. 2018, 6, 1800646.

13. G. Li, S. Chen, N. Pholchai, B. Reineke, P. W. H. Wong, E. Y. B. Pun, K. W. Cheah, T. Zentgraf, S. Zhang, Nat. Mater. 2015, 14, 607.

14. R Zhao, B Sain, Q Wei, C Tang, X Li, T Weiss, L Huang, Y Wang, T. Zentgraf, Multichannel vectorial holographic display and encryption, Light: Sci. Appl. 2018, 7, 95.

15. Amir Arbabi, Yu Horie, Mahmood Bagheri, Andrei Faraon, Dielectric metasurfaces for complete control of phase and polarization with subwavelength spatial resolution and high transmission, Nature Nanotechnology 10, 937–943 (2015).

16. Z Zhang, D Wen, C Zhang, M Chen, W Wang, S Chen, X Chen, Multifunctional light sword metasurface lens, ACS Photonics 5 (5), 1794 (2018).

17. F Yue, C Zhang, XF Zang, D Wen, BD Gerardot, S Zhang, X Chen, High-resolution grayscale image hidden in a laser beam, Light: Science & Applications 7, 17129.

# Chapter 6 Summary and outlook

## 6.1 Summary

In this thesis, we have concentrated on the arbitrary control of phase and polarization profiles of a laser beam at subwavelength scales on demand, by using the metasurfaces. Our work will not only yield fundamental insights into physical phenomena not easily accessible using even the highest quality commercial devices, but also lead to novel applications in polarization encoded nanophotonic devices. The uniqueness of our approach in the generation and manipulation of OAM beams, simultaneous control of holograms and twisted light beams, image hidden, and arbitrary polarization manipulation makes this technology very attractive for diverse applications in the areas such as encryption, imaging, optical communications, quantum science, and fundamental physics.

To investigate arbitrary control of phase and polarisation profiles by using metasurfaces and their applications in the realization of multichannel devices for OAM control, hologram control, polarization encoded nanophotonics, what we have done can be summarized as follows:

1. To simulate, optimise and design metasurface devices which have polarization and phase controlling functionalities and engineered spatial distribution of polarisation and phase.
2. To fabricate reflection-type plasmonic metasurfaces consisting of nanorods and transmission-type dielectric metasurfaces composed of nanopillars, which have been used to generate the required polarisation and phase profile in each particular case.
3. To experimentally demonstrate the novel optical components with tailored functionality, such as a multichannel device for OAM control, hologram control, high-resolution grayscale image (Maxwell's portrait) hidden in a light beam, and colour image embedded in a metasurface with colour-mixing functionality.
4. To demonstrate the metasurface devices in various applications, such as continuous control of the superposition of OAM beams, simultaneous control of holograms and OAM superposition, image-switchable hologram with a hidden image for anti-counterfeiting.

## 6.2 Outlook

Understanding and controlling the phase and polarization between light and nanostructures is fundamental to science and technology development. Optical metasurfaces have gained considerable interests due to their unprecedented capabilities for the modulation of amplitude, phase and polarization at subwavelength scale. Using the technology and experimental expertise that we already have, we can further push the boundaries of this technology to achieve more novel functionalities. For example, to improve our approach of the color image hiding discussed in Chap.4, where red and green are used as two primary colors, I would like to extend the two colors to three primary colors (RGB). Arbitrary color image can then be encoded into the polarization profile of structured light generated by the meatasurfaces. Further ahead, and in my opinion the applications of metasurfaces in the following research areas are very promising in the near future.

### 6.2.1 Full polarization measurement

Polarization contains valuable information about the imaged environment (e.g., material and tissue properties, surface roughness, shape and texture of reflecting surfaces, the orientation of light emitters, or the optical activity of various materials), which is typically unavailable in spectral content, color and intensity information of light. The polarization state of light over a scene of interest can be measured by polarimetric imaging, which has led to many applications ranging from astronomy and remote sensing to biology (e.g., early cancer formation), medicine and microscopy. A good example is the recently demonstrated full Stokes characterization of the polarization states by using the dielectric metasurface [1] (see Fig.6-1). This method overcomes the 50% theoretical efficiency limit of division of focal plane polarization cameras (DoFP-PCs). This figure was achieved by splitting and focusing light in three different polarization bases, rather than using the polarization filtering approach.

### 6.2.2 Metasurface devices for particle trapping

The detection of optical scattering and gradient forces over the micron sized particles was first discovered in 1970s by Arthur Ashkin, who won the Nobel prize in 2018 for his work in the research and development of optical tweezers. Optical tweezers have provided very useful tools for the research fields in biology, biochemistry, biophysics, and medical sciences.

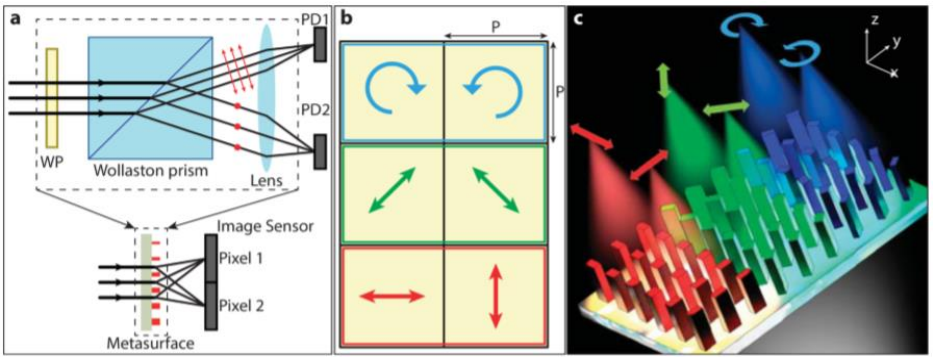


**Figure 6-1 Concept of a metasurface polarization camera [1].** (a) Top: Schematics of a traditional setup of a polarimetry which consists a waveplate (quarter or half), a Wollaston prism and a lens which focuses the incident light onto detectors. Bottom: A compact metasurface unit which can be used to realize the same functionality and can be directly integrated on an image sensor. WP: waveplate; PD: photodetector. (b) Possible arrangement for a super-pixel of the polarization camera, comprising six image sensor pixels. Three independent polarization bases (H/V, ±45°, and RHCP/LHCP) are chosen to measure the Stokes parameters at each super-pixel. (c) Three-dimensional illustration of a super-pixel focusing different polarization states to different spots. The colors are used only for clarity purpose and are not related to wavelength information.

There have been different methods adopted for the particle trapping, such as optical cell rotator, which is a fiber-based laser that can hold and manipulate the living cells. The bulky optical elements in the conventional optical tweezers and the limited functionalities make them difficult to be integrated into a compact platform. Although highly focused optical vortex has been proposed to trap particles, it is technically challenging to realize that with compact devices. In last several years, the unprecedented capability of metasurface in the arbitrary manipulation of phase, amplitude and polarization with subwavelength resolution has provided new approaches to realize optical tweezers. In a recent paper, authors demonstrated how a plasmonic polarization-sensitive metalens provided different stable trapping centers along the optical axis [2]. Based on the content of this thesis, I am very interested in the research that how OAM can be used to trap and rotate particles precisely. It is possible to extend the current state of the art in biological sample trapping, rotation and tomographic imaging by using bespoke nanophotonics in the form of optical metasurfaces to shape the light into complex patterns.

### 6.2.3 Ultracompact devices for quantum sciences

The compact metasurface devices can replace traditional bulk optical components. Recently, metasurfaces have been extended to the quantum science. The results in the determination of quantum state of multiple photons and the generation of entanglement between spin and OAM of single photons are very promising, which can aid the

development of integrated quantum systems based on the metasurface platform [3]. Recently, the ground-to-satellite quantum key distribution has attracted a lot of research attention. How to simplify the experimental setup and complete the same task is a big technical challenge. On the other hand, miniaturization and integration are two continuing trends in the production of photonic devices and construction of optical systems. Ultrathin optical components with multiple functionalities are desirable for future high-performance portable optical devices and systems with smaller footprints and lower weight. There are numerous challenges, either fundamental or technological, in building devices that are compact, efficient and integrable. Traditional beam splitters have useful properties, but are typically bulky, heavy, and costly. Although planar components based on diffractive optics (e.g., gratings, Fresnel lenses) have been used for decades, their limited functionality and difficulty of integration have been key incentives to search for better alternatives. Benefiting from the exotic optical properties, metasurfaces are very good candidates to complete these tasks that are very challenging or impossible with conventional methods.

### 6.2.4 Nonlinear metasurface devices for polarization manipulation

The capability of metasurface in the manipulation of light propagation has been extended to the nonlinear optics, providing new opportunities for the realization of nonlinear optical devices[4]. Nonlinear optical processes such as second, third and high harmonic generation have been extensively investigated by using both plasmonic and dielectric metasurfaces. It is reported that the nonlinear optical susceptibility of the meta-atoms strongly depends on the orders of the nonlinear process, the spin states of fundamental wave (FW) and the local symmetry of the meta-atom. Because of the nonlinear P-B phase, the method to continuously and locally tailor the phase of nonlinear optical susceptibility was established recently, facilitating applications such as nonlinear holography and nonlinear image encryption and so on. For example, the arbitrary polarization manipulation can also be realized based on nonlinear metasurface devices. In the future, we are planning to demonstrate a nonlinear optical metasurface to locally manipulate the polarization states of the SHG wave and encode a high-resolution image in the polarization profile accordingly. Such nonlinear image information could be revealed after filtering out the FW and converting the polarization profile into intensity profile according to the Malus's law. The polarization encryption protocol proposed in this work will provide a novel route for optical encryption, security, anti-counterfeiting and background-free image construction.

## 6.3 References


1. Arbabi, E., et al., Full Stokes imaging polarimetry using dielectric metasurfaces. arXiv preprint arXiv:1803.03384, 2018.

2. Markovich, H., Shishkin, I.I., Hendler, N. and Ginzburg, P., 2018. Optical Manipulation along an Optical Axis with a Polarization Sensitive Meta-Lens. *Nano letters*, *18*(8), pp.5024-5029.

3. Stav, T., et al., Quantum entanglement of the spin and orbital angular momentum of photons using metamaterials. Science, 2018. **361**(6407): p. 1101-1104.

4. Li, G., S. Zhang, and T. Zentgraf, Nonlinear photonic metasurfaces. Nature Reviews Materials, 2017. **2**(5): p. 17010.